

**CONTINUOUS CARDIORESPIRATORY MONITORING USING
BALLISTOCARDIOGRAPHY FROM LOAD CELLS EMBEDDED IN A
HOSPITAL BED**

A Dissertation
Presented to
The Academic Faculty

By

Hewon Jung

In Partial Fulfillment
of the Requirements for the Degree
Doctor of Philosophy in the
School of Electrical and Computer Engineering

Georgia Institute of Technology

August 2022

© Hewon Jung 2022

**CONTINUOUS CARDIORESPIRATORY MONITORING USING
BALLISTOCARDIOGRAPHY FROM LOAD CELLS EMBEDDED IN A
HOSPITAL BED**

Thesis committee:

Dr. Omer T. Inan, Advisor
School of Electrical and Computer
Engineering
Georgia Institute of Technology

Dr. Woon-Hong Yeo
The George W. Woodruff School of
Mechanical Engineering
Georgia Institute of Technology

Dr. Ying Zhang
School of Electrical and Computer
Engineering
Georgia Institute of Technology

Dr. Nima Ghalichechian
School of Electrical and Computer
Engineering
Georgia Institute of Technology

Dr. Rishikesan Kamaleswaran
Department of Biomedical Informatics
Emory University

Date approved: July 15, 2022

To my parents, sister, and Junhwan

ACKNOWLEDGMENTS

To get to this moment wrapping up my dissertation and looking back at my Ph.D. journey, there were a lot of ups and downs that could have made me give up this long race. The only reason I am at this moment is because of my family, friends, and mentors and their support.

I would first like to express gratitude to my advisor Professor. Omer Inan. From my first day at Georgia Tech, I wished to have Omer as my advisor; his lab was the first place I wanted to join. Unfortunately, his lab was filled at that moment and I had to spend a semester searching for an advisor. However, I was fortunate to connect with him again and joined the lab later on. And this turned out to be the most fortunate moment that led to the successful completion of this journey. He was a friendly, thoughtful, and creative mentor who has motivated me scientifically and personally. While guiding and supporting my work, he also allowed me to grow as an independent researcher, which I believe would be the basis for all my future steps. All words here are not enough to describe how grateful I am to have him as my advisor and without his guidance and supervision, this work would not have been possible.

I also would like to thank Dr. Ying Zhang, Dr. Woon-Hong Yeo, Dr. Nima Ghalichechia and Dr. Rishikesan Kamaleswaran for taking the time to serve as a member of my committee and provide insightful feedback on this work and future directions. Moreover, I would like to thank our collaborators – Dr. Eric Agdeppa and Timothy Receveur – who supported and worked together on the bed BCG project comprising this dissertation. All the bi-weekly meetings and discussions I had with Eric and Tim were delightful times during

my Ph.D.

I have been privileged to be part of Inan Research Lab and work with brilliant colleagues. Scientific discussions, jokes, and coffee chats I had with my colleagues were full of joy and would be unforgettable. I would like to thank current and former lab members, Sinan Hersek, Nil Gurel, Beren Semiz, Venu Ganti, Mobashir Shandhi, Mohsen Safaei, Nordine Sebki, Samer Mabrouk, Hyeon Ki Jeong, Jacob Kimball, Jon Zia, Andrew Carek, Nick Bolus, Caitlin Teague, Daniel Whittingslow, Dotun Ode, Daniel Hochman, Asim Gazi, Sevda Gharaehbaghi, Kristy Scott, Michael Chan, David Lin, Sungtae An, Goktug Ozmen, Mohammad Nikbakht, Luis Rosa, J Antonio Sánchez-Pérez, John Berkebile, Cem Okan Yaldiz, Afra Nawar, Farhan Rahman, Emily Moise, Tamara Lambert, Christopher Nichols, and Brandi Nevius. Especially, I would like to thank Nil for working together on one of the projects and mentoring me during my early days in Ph.D. I would like to thank Hyeon Ki and Venu for being my coffee mate, friend, colleague, and many more and for spending a lot of time together for data collection. I would like to thank Jacob and David for working together on this dissertation project, reading all my drafts, and giving me insightful feedback and encouraging words.

I would also like to thank my other Georgia Tech friends who have gone through this journey together from my day one in Atlanta and would be my friend beyond our times at Georgia Tech. Each one of them was a warm and inspiring person and becoming their friend was one of the most valuable gifts I got during my time here.

There is one person without whom I cannot explain my last 10 years – my partner, Junhwan. He has been with me for 10 years since my freshman year after we first met when we were high school juniors. Indeed, he is one of the people who inspired me the

most, not only as a peer researcher in the scientific field but also as a human being. Without him tolerating me while I struggled during my Ph.D., this moment would not have come and I would not have grown this much. The years I had with him were always full of love and blessing and I cannot wait to have many more years together.

Last but foremost, I would like to thank my mom, dad, and sister for their unconditional love and support. Regardless of whether I am on the downhill or the uphill of this journey, they have been with me all the time. When I was losing belief in myself, they had belief in me more than I had in myself, reinforcing how valuable I am. Without their sacrifice, I would not have been allowed to be on this journey and without their patience and support, this dissertation would not have existed. Thank you all for always being on my side and I would like to dedicate this dissertation to my family.

TABLE OF CONTENTS

Acknowledgments	iv
List of Tables	x
List of Figures	xi
List of Acronyms	xv
Summary	xvii
Chapter 1: Introduction and Background	1
1.1 Motivation	1
1.2 Non-invasive Cardiac Signals	2
1.2.1 Ballistocardiogram	2
1.2.2 Photoplethmogram	4
1.3 Continuous Vital Monitoring	6
1.3.1 Heart Rate	6
1.3.2 Respiratory Monitoring	8
1.3.3 Blood Pressure	11
1.4 Specific Aims and Contributions	13
1.5 Thesis Organization	15
Chapter 2: Heart Rate Estimation from Ballistocardiogram Signals	16
2.1 Probabilistic Approach for Accurate Heart Rate Estimation using Ballisto- cardiogram from an Array of Load Cells in a Hospital Bed	16
2.1.1 Introduction	16
2.1.2 Methods	19
2.1.2.1 Human Subjects Study and Instrumentation	19
2.1.2.2 Pre-Processing	21
2.1.2.3 Load-Cell Array Processing	25
2.1.2.4 Heartbeat Interval estimation	28
2.1.3 Evaluation	31
2.1.3.1 Window-Based HR Estimation	31
2.1.3.2 Heartbeat Interval Estimation	33
2.1.4 Results	33
2.1.4.1 Window-Based HR Estimation	33

2.1.4.2	Heartbeat Interval Estimation	37
2.1.5	Discussion	38
2.1.6	Conclusion	43
2.2	Estimation of Heart Rate using Ballistocardiogram Measured from Load Cells using a Deep Learning Model	44
2.2.1	Introduction	44
2.2.2	Methods	45
2.2.2.1	Source/Target Signals	45
2.2.2.2	U-Net Architecture	47
2.2.2.3	Model Training and Testing	49
2.2.2.4	Channel Combination	51
2.2.2.5	Evaluation	51
2.2.3	Results and Discussion	52
2.3	Conclusion	53
Chapter 3:	Estimation of Tidal Volume	55
3.1	Introduction	55
3.2	Related Work	59
3.3	Methods	62
3.3.1	Experimental Protocol	62
3.3.2	Measurements	64
3.3.3	Pre-processing	64
3.3.3.1	Ground Truth Processing	66
3.3.3.2	Derivation of the center of mass	66
3.3.4	Respiratory Rate and Low-Frequency Feature Extraction	68
3.3.4.1	Feature computation	68
3.3.4.2	Respiration Quality Index (RQI)	69
3.3.5	ECG-based BCG segmentation	70
3.3.6	ECG-independent BCG segmentation	71
3.3.6.1	Estimation of J-wave location using HR estimation algorithm	71
3.3.6.2	Rejection of false positive beats	72
3.3.6.3	I- and K-wave detection after correction	73
3.3.7	BCG heartbeat features	74
3.3.8	Machine Learning Model Training	74
3.3.8.1	Regression Model	74
3.3.8.2	Evaluation	75
3.3.8.3	Feature combinations	76
3.4	Results and Discussion	76
3.4.1	RR Estimation	76
3.4.2	TV Estimation	79
3.4.3	Evaluation of Features	81
3.4.4	Comparison with State-of-the-art Methods	85
3.4.5	Limitations and Future Work	86

3.5	Appendix	87
3.6	Conclusion	88
Chapter 4:	Estimation of Blood Pressure	90
4.1	Introduction	91
4.2	Methods	93
4.2.1	Experimental Protocol	93
4.2.2	Pre-Processing	97
4.2.3	Signal Processing-based Feature Extraction	99
4.2.3.1	Signal Quality Indexing	99
4.2.3.2	Fiducial Point Detection	100
4.2.4	Neural Network-based Feature Extraction	101
4.2.4.1	Source/Target Signals	101
4.2.4.2	U-Net Architecture	102
4.2.4.3	Model Training and Testing	104
4.2.5	Calibration	105
4.2.5.1	Calibration for PTT	105
4.2.5.2	Re-scaling the generated BP waveforms	107
4.2.6	Evaluation	108
4.3	Results	108
4.3.1	Calibration per day and posture	108
4.3.1.1	PTT-based method	108
4.3.1.2	U-Net-based method	109
4.3.2	Calibration per day	112
4.3.2.1	PTT-based method	112
4.3.2.2	U-Net-based method	112
4.4	Discussion	113
4.4.1	Comparison between finger and toe PPG	113
4.4.2	Source signals in U-Net	114
4.4.3	Comparison between PTT and U-Net	115
4.4.4	Calibration	116
4.4.5	Limitations and Future Work	118
4.5	Conclusion	119
Chapter 5:	Conclusion and Future Work	121
5.1	Conclusion	121
5.2	Future Work	122
5.2.1	Final Remarks	124
References	126

LIST OF TABLES

2.1	Accuracy of Heart Rate Estimation - Mean Absolute Error, MAE (bpm) . . .	35
2.2	Accuracy of heartbeat interval estimation	36
3.1	State-of-the-art Non-invasive Respiratory Sensing Methods	60
3.2	Features extracted from load cell signals	73
3.3	TV Estimation Errors for Different Feature Combinations	77
3.4	Subject-wise TV Estimation Error (ECG-independent Model)	82
4.1	State-of-the-art Studies for Blood Pressure Estimation	94
4.2	Results: PTT vs U-Net	109
4.3	Subject-wise BP Estimation Error (MAE)	110

LIST OF FIGURES

1.1	An example plot of ECG and BCG	3
1.2	An example plot of ballistocardiogram (BCG) and photoplethysmogram (PPG)	5
2.1	Overview of the study and the test setup. Four load cells are located on the four corners of the bed frame (RH - right head channel, LH - left head channel, RF - right foot channel, and LF - left foot channel of load-cell BCG signals, load cell locations are colored as orange in the top left picture). Load-cell outputs are amplified using a custom-designed analog front end (AFE) to obtain BCG signals. BCG signals are used to estimate heart rate (HR) and are validated against ECG.	19
2.2	(a) Top: An example of the recorded BCG and ECG signals. RH - right head channel, LH - left head channel, RF - right foot channel, and LF - left foot channel of load-cell BCG signals. Bottom: The experimental protocol consisting of five different postures, each lasting for a minute. (b) A block diagram of the HR estimation algorithm composed of three parts— pre-processing, computation of PDF, and load-cell channel array processing. . .	21
2.3	An example plot of raw BCG signals measured in each posture.	21
2.4	An example plot of PDFs from each channel.	26
2.5	Bar plots of relative HR estimation error in percent (E_{rel}) for each posture and scenario. Scenario 1 (S1) - Multi-channel fusion; Scenario 2 (S2) - Weighted multi-channel fusion; Scenario 3 (S3) - Weighted multi-channel fusion with array processing	34
2.6	Box plot of relative HR estimation error in percent (E_{rel}) for an additional dataset. Scenario 1 (S1) - Multi-channel fusion; Scenario 2 (S2) - Weighted multi-channel fusion; Scenario 3 (S3) - Weighted multi-channel fusion with array processing; Rest-first 3 minutes of baseline recording, Talking-2 minutes of talking session. The coverage for each case is written above the bar.	36

2.7	Bland-Altman plots for the heartbeat interval estimation shown by postures. Red horizontal lines indicate 5 th (P_5) and 95 th (P_{95}) percentile of error. Different marker colors indicate each subject. MoD = Mean of Differences, LoA = Limit of Agreement given as $P_{95} - P_5$	37
2.8	Coverage, percent error vs q -value threshold plot for each posture. Blue line with the left y-axis indicates the percent error (%). Red line with the right y-axis indicates the coverage(%). For both y-axes, the x-axis was set as the q -value threshold.	40
2.9	An example plot of the 4-channel BCG signals (Top) and the target/generated triangular waveform (Bottom). The ground truth target waveform is represented in blue and the grey lines show generated waveform from each channel. The red represents the average of the generated waveforms.	46
2.10	An example plot of the transformed ECG generated through the distance transform of the ground truth ECG recording. Yellow-Transformed ECG, Blue-Raw ECG, Red- ECG R-peaks	46
2.11	The overview of the U-Net architecture. The architecture has two parts: the contraction and the expansion path. The dimension of the signal is written on the left/right side of the feature map and the number of channels is written on the top of the feature map. CONV-1D convolutional layer, BN-Batch Normalization, leaky ReLU-leaky Rectified Linear Unit. Red: Strided CONV+BN+leaky ReLU, Yellow: tranposed CONV+BN+leaky ReLU, Gray: Skip connections	47
2.12	(Top) An example plot of power spectral density plot computed from the FFT. (Bottom) An example plot of generated waveforms from 4 different BCG channels. Each color indicates different channel. The channel colored in red in this example shows small SNR based on the top plot, therefore showing the low-quality waveform on the bottom plot.	50
2.13	A boxplot showing the HR estimation error per posture and tasks. Each color indicates different respiratory tasks including baseline, shallow regular, shallow fast, deep fast and deep slow.	52
3.1	Overview of the study and the measurements. In the study, four load cell channels in the hospital bed (Centrella® bed) and the spirometer were recorded. Tidal volume (TV) was estimated with the machine learning-based regression algorithm using features extracted from the load cell signals. The model was evaluated against the ground truth TV values from the spirometer.	58

3.2	Left: An example plot of a respiratory volume waveform for each respiratory task. Right: An overview of the set of respiratory tasks performed in this study. The set shown here was repeated for four different postures. . . .	62
3.3	(a) A block diagram of end-to-end signal processing for the estimation of RR and TV. The left side shows the feature extraction from load cell signals, and the right side shows processing steps for ground truth spirometer measurements. (b) An example plot of the airflow (top) and volume (bottom) derived through the integration of airflow. (c) (Top: side view) Visualization of supine, lateral, and seated posture and corresponding body axes in each posture. DV: dorso-ventral, HF: head-to-foot, LA: lateral (Bottom: top view) The locations of the load cells and the datum for the derivation of changes in the center of mass. Red boxes represent the location of load cells. RH = right head, RF = right foot, LH = left head, LF = left foot. Datum is considered as RF.	65
3.4	(a) An example plot of changes in the center of mass along the X , Y , and Z -axes of the bed. From the top, each trace represents CG_x , CG_y , and CG_z , respectively. (b) An example of the power spectral density (PSD) estimated from the CG_y of the low-frequency force signal and the detected breaths. (c) An illustration of ECG-based and ECG-independent BCG segmentation. In the ECG-based approach, the BCG signal was segmented into heartbeats using ECG R-peaks (grey vertical lines). In the ECG-independent approach, the candidate J-wave locations (green markers) were returned by the multi-channel HR estimation algorithm. (d) A plot of extracted heartbeats from one 16-second BCG window. Grey represents all the BCG heartbeats found in the window, and the red represents the averaged beat.	67
3.5	(a)-(d) Correlation between the estimated and actual TV. The results are shown by posture - (a): Supine, (b): Right lateral, (c): Left lateral, (d): Seated. M=Number of datapoints in the plot, N=Number of subjects (e) A Bland-Altman plot for RR estimation error, including all postures, tasks, and subjects. Dotted lines indicate 95% LoA. (f) A correlation plot for the posture-independent model trained on the entire dataset, including all postures. Shape-tasks, Color-subject. (g) A plot for relative feature importance averaged over the four posture-specific models. Same feature types are represented with the same color with different intensity	78
3.6	A plot of Mean absolute error (MAE) over coverage (%) for RR estimation from load cell signals evaluated against ground truth RR from a respiratory chest belt. Each data point indicates a different RQI threshold level. . . .	87

4.1	The overview of the test setup and the protocol for human subjects study engaging tasks to modulate BP. (a) 4-channel BCG, Finger/Toe PPG, BP, and ECG signals were recorded during the protocol. Pulse oximeter sensors were placed on right index toe and finger. Finger BP cuff was placed on the same hand as PPG. (b) Mental arithmetic (MA), Valsalva maneuver (VM), hand grip (HG), and cold pressor (CP) were performed in four different postures including supine, left/right lateral, and the seated posture in this study. (c) An example plot of PPG (Finger/Toe) and BCG were shown for one heartbeat cycle. PAT: Pulse Arrival Time, PTT: Pulse Transit Time, PPG: Photoplethysmogram, BCG: Ballistocardiogram, ADC: Analog to Digital Converter	93
4.2	The histograms show the distribution of systolic (SBP) and diastolic pressure (DBP) measured by the finger BP cuff. The gray and blue represents the distribution of BP values in the training and test set, respectively. The top and bottom rows represent two different train/test splits used for the DL-based model.	95
4.3	The overview of signal processing pipeline. ECG, PPG, and BCG signals were first band-pass filtered and BP signals were low-pass filtered to smooth out. The feature extraction was done in two ways—the signal processing-based extraction of PTT and deep learning (DL) model for data driven feature extraction. For the signal processing approach, the SQI was computed from each signal to remove segments corrupted by the motion artifacts. Fiducial points were detected to compute features including PAT and PTT. For the DL-based approach, the U-Net architecture was used to translate PPG and BCG waveforms into the BP waveform. From the extracted features, the calibration was performed for both methods to estimate systolic (SBP), diastolic (DBP), and the mean arterial pressure (MAP). . . .	98
4.4	The overview of the U-Net architecture. The architecture has three parts: the contraction, and expansion path. The dimension of the signal is written on the left/right side of the feature map and the number of channels is written on the top of the feature map. CONV-1D convolutional layer, BN-Batch Normalization, leaky ReLU-leaky Rectified Linear Unit. Red: Strided CONV+BN+leaky ReLU, Yellow: tranposed CONV+BN+leaky ReLU, Gray: Skip connections	102
4.5	The overview of the BP estimation results for each BP component. The color and shape on the plot represent different subjects and posture, respectively. (Top) The plot shows the correlation between the estimated and the true BP. (Bottom) The plot shows the error distribution for each BP component. The 95 % limit of agreement (LoA) is represented by the horizontal dotted lines.	106

LIST OF ACRONYMS

ABP	Arterial Blood Pressure
BCG	Ballistocardiogram
BP	Blood Pressure
bpm	Beats per minute
brpm	Breaths per minute
DBP	Diastolic Blood Pressure
DL	Deep Learning
ECG	Electrocardiogram
FFT	Fast Fourier Transform
HR	Heart Rate
IBI	Inter Beat Interval
MAE	Mean Absolute Error
MAP	Mean Arterial Pressure
ME	Mean Error
ML	Machine Learning
MSE	Mean Squared Error
PAT	Pulse Arrival Time
PDF	Probability Density Function
PEP	Pre-Ejection Period
PPG	Photoplethmogram
PTT	Pulse Transit Time
RMSE	Root Mean Squared Error

RQI Respiration Quality Index

RR Respiratory Rate

RV Respiratory Volume

SBP Systolic Blood Pressure

SCG Seismocardiogram

SNR Signal-to-Noise Ratio

TV Tidal Volume

SUMMARY

Early recognition of abnormal vital signs is essential for the early detection of patient deterioration in hospitals. The deterioration in the physiologic state is often quantified by an early warning score (EWS) derived from a set of vitals including the heart rate (HR), respiratory rate (RR), body temperature, and blood pressure (BP). Though the EWS has shown promise in alarming the potential need for a higher level of care, it often fails to detect preventable adverse events due to intermittency in vital measurement.

Continuous vitals monitoring at the bedside could address this limitation. The objective of this research is to explore signal processing and machine learning techniques to allow continuous monitoring of cardiorespiratory parameters using the ballistocardiography (BCG) signals recorded with sensors embedded in a hospital bed. First, an array processing technique to optimize the fusion of information from multiple channels was presented and demonstrated the improved HR estimation. Through HR error analysis by posture, postural effects on bed-based BCG signals were investigated for accurate physiological interpretation of the BCG obtained in a variety of postures from a subject in bed. In addition, a data-driven approach for HR estimation using a deep learning (DL) model was also demonstrated. In this approach, the BCG signals were transformed into an interpretable triangular waveform, from which the locations of the heartbeats could be estimated.

Second, RR and respiratory volume (RV) were estimated from the low-frequency components of the load-cell signals recorded with a hospital bed. Incorporating the multi-channel low-frequency waveforms allowed a complete characterization of 3D respiratory movements, leading to improved respiratory parameter estimation.

Lastly, two different models — 1) Conventional pulse transit time (PTT)-based model and 2) DL-based model — were presented for the BP estimation. Multi-channel BCG signals from the load cells and the photoplethysmogram (PPG) signals from a pulse oximeter were used to compute PTT or as an input to the DL models. Both methods demonstrated a robust estimation accuracy with frequent calibration, while the DL-based model has shown advantages against postural variability. While the calibration requirement remains challenging, this work has provided the groundwork for establishing continuous BP monitoring in hospitals using the existing sensors.

Overall, this work established methods that would enable non-invasive and continuous monitoring of standard vital signs in various settings utilizing the sensors already embedded in commonly-deployed commercially available hospital beds without the requirement for auxiliary sensing hardware. Such technologies could potentially improve the continuous assessment of the patients' physiologic state without adding an extra burden on the caregivers.

CHAPTER 1

INTRODUCTION AND BACKGROUND

1.1 Motivation

Continuous vitals monitoring is pivotal for managing and treating cardiovascular diseases, the leading causes of death globally amounting to 17.6 million deaths per year[1]. In hospital settings, continuous monitoring of physiological parameters enables early detection of degeneration in patients. Improving access to continuous cardiac monitoring to all patients on hospital beds could reduce the number of days per hospital stay or deaths related to cardiac arrest and “code blue” events [2, 3].

Continuous physiological measurement involves the measurement of the invasive, non-invasive, or unobtrusive approaches. Invasive approaches require the insertion of sensors into the body, such as catheters or arterial lines, and are the most accurate means of monitoring the overall physiological status of patients. Non-invasive approaches use sensors placed on the skin for detection of biosignals (e.g., electrocardiogram (ECG)), and are frequently used in cardiac patients for continuous monitoring of heart rhythm and rate. Unobtrusive approaches such as non-contact measurements where the sensor is not directly touching the patient are preferred whenever possible, but are not commonly employed in hospital settings since their accuracy is typically limited compared to invasive or non-invasive alternatives. However, even non-invasive solutions can be uncomfortable and impractical in some situations, such as for patients who require multiple medical sensors attached to their

body, infants who have small body surface area, or burn victims [4, 5]. Moreover, the costs of using ECG measurement systems ubiquitously for all patients in hospital settings would be unrealistically high for such a solution to be feasible broadly.

An unobtrusive measurement modality that has been investigated over the past decade for cardiovascular sensing is ballistocardiogram (BCG) signal [6, 7, 8]. This dissertation demonstrates the use of BCG measured from load cells on the hospital bed to continuously monitor cardiorespiratory parameters such as heart rate (HR), respiratory rate (RR) and volume (RV), and the blood pressure (BP).

This chapter provides a brief background on the use of BCG signals for cardiorespiratory monitoring. Section 1.2 introduces cardiac signals utilized in this work—BCG and photoplethmogram (PPG). Section 1.3 reviews current methodologies for continuous monitoring of vitals including HR, RR and RV (i.e. tidal volume (TV)), and BP using BCG measurements and other biosignals. Section 1.4 introduces specific aims and contributions of this work. Finally, the organization of this thesis is outlined in Section 1.5.

1.2 Non-invasive Cardiac Signals

1.2.1 Ballistocardiogram

BCG is a cardiogenic vibration signal that measures the recoil forces of the body in reaction to the movement of blood through the cardiovascular tree [9]. During systole, as the blood is ejected out of the left ventricle into the large vessels, the center of mass of the body moves towards the head. In the other direction, as the blood moves towards the peripheral vessels, the center of mass of the body move towards the feet. Such repeated changes in

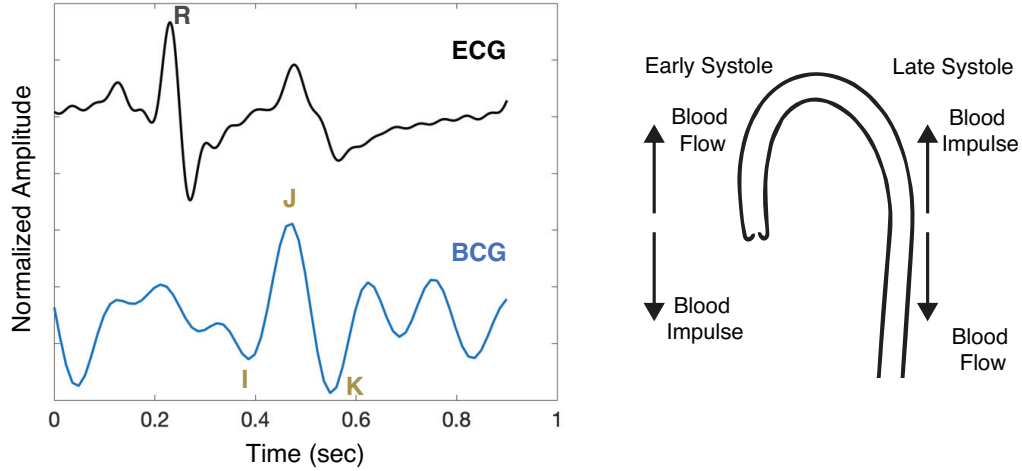


Figure 1.1: An example plot of ECG and BCG

the center of mass generate repetitive BCG waveform occurring at a cardiac frequency [10, 6].

Resulting ballistocardiographic force is three-dimensional [11]. The longitudinal component reflects head-to-foot deflections of the body, while the transverse component measures displacement in dorso–ventral direction. Most of the work including the original bed- and table-based BCG systems focused on the head-to-foot vector, which comprised the largest projection of the 3-D forces resulting from the cardiac ejection. However, the head-to-foot and dorso–ventral forces are often coupled together unavoidably for some sensing systems, adding extra challenge in interpreting results [6].

The traditional head-to-foot BCG could be characterized by three main complexes: the I, J, and K waves as shown in Figure 1.1. Each wave represents the acceleration of blood in various parts of the arterial tree. In particular, the I wave occurs during early systole when the blood moves from the left ventricle. Then the I wave is followed by the J wave, the largest head-ward wave that occurs late in systole. Therefore, previous work has shown a correlation between the timing of the I wave or J wave and some physiological parameters

such as pre-ejection period (PEP) or pulse transit time (PTT).

Though the BCG phenomenon was first discovered more than 100 years ago in 1877 by Gordon, BCG had not gained attention for a while due to insufficient standard measurement methods and a lack of understanding of the physiologic origin of the BCG waveform. However, technological advancements in BCG sensing instruments and signal processing techniques for assessing BCG signals have opened feasibility in its clinical use.

The BCG can be measured unobtrusively without any attachment of sensors or electrodes to the body and thus allowing the data to be recorded continuously throughout normal daily living. Modern BCG measurement systems include various form factors including bathroom scales [12], chairs [13], and beds [14, 15, 16, 7, 8]—all can be instrumented at a relatively low cost. In hospital settings, bed-mounted sensors can be deployed to capture BCG signals throughout the day while the patient is on the bed. Commercially available bed-based BCG sensing systems for both hospital and at-home settings include Emfit (Vaa-jkoski, Finland) [17], EarlySense (Ramat Gan, Israel) [18], and Beddit (Apple, CA, USA) [19] — all of which are systems providing a single channel of BCG output. Furthermore, the ballistocardiographic force has the potential to be measured anywhere on the body as long as the subject remains still. Therefore, BCG can also be captured by wearable devices with accelerometers such as smart wristwatches.

1.2.2 Photoplethmogram

The photoplethysmogram PPG is an optical sensing modality that measures changes in blood volume pulse through differential absorption of light [20]. PPG requires an optical sensing system composed of a light source and a photodiode that measures the intensity

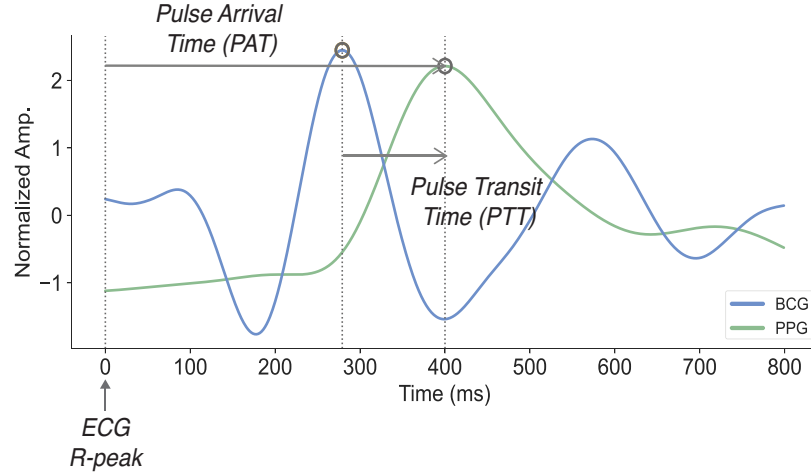


Figure 1.2: An example plot of ballistocardiogram (BCG) and photoplethysmogram (PPG)

of the light. As the blood volume fluctuates according to the cardiac cycle, the amount of light absorbed by the artery varies, resulting in fluctuations in the amount of light reaching the photodiode. The resultant waveform creates the PPG signal, indicating the change in arterial blood volume [20]. The two modes of operation for PPG sensing include the reflectance mode and transmission mode. Reflectance mode PPG measures the intensity of light reflected to a photodiode while transmittance mode PPG measures the intensity transmitted through the capillary bed and surrounding tissues [21]. Therefore, the transmissive mode limits sensing to the extremity locations such as toes, fingers, or earlobe while allowing high signal quality in general. For the reflective mode PPGs, the signal quality varies based on the sensor location as it is more susceptible to motion artifacts. However, reflective mode PPG can be measured from more diverse locations on the body.

The amplitude of the PPG signal decrease with the systolic ejection of blood; therefore, the inflection point on the PPG signal reflects the arrival of the systolic pulse wave at the distal location where the PPG sensor is placed. The timing delay between the ventricular depolarization corresponds to R-peak in ECG and the PPG inflection point is known as

pulse arrival time (PAT) as shown in Figure 1.2. The PPG inflection point is also used as a distal timing reference for the PTT, where PTT is defined as the time it takes for the pressure pulse to travel along the arterial wall [22, 23]. To obtain PTT, the pulse wave needs to be measured at two arterial sites —and one proximal and one distal (far down the arterial tree such as radial artery) to the heart. PPG sensors on locations such as finger [24], wrist [25], and foot [26] are commonly used to acquire distal timing reference. As will be further explored in Chapter 4, PTT has recently gained prevalence for estimating BP non-invasively due to its linear correlation to BP.

1.3 Continuous Vital Monitoring

1.3.1 Heart Rate

As the BCG sensing system can be implemented into everyday objects that are commonly and easily used without interfering with daily activities, the BCG signal has been widely studied for monitoring basic vitals such as heart rate. In [27], beat-to-beat HR was estimated from the BCG signal measure from the film-type transducer material called polyvinylidene fluoride (PVDF), placed on the chair. In the study, beat-to-beat BP was also estimated from BCG along with PPG signals. In [28], HR and RR was measured with BCG signals recorded with the bathroom scale. Among several BCG sensing modalities, one of the most common form-factor is a bed-based system, which can be used in both home and hospital settings for long-term monitoring. In hospital settings, bed-mounted sensors can be deployed to capture BCG signals throughout the day while the patient is on the bed. Commercially available bed-based BCG sensing systems for both hospital and

at-home settings include Emfit (Vaajakoski, Finland) [17], EarlySense (Ramat Gan, Israel) [18], and Beddit (Espoo, Finland) [19] — all of which are systems providing HR and RR while the person is on the bed from a single channel of BCG output.

Though each bed-based BCG system demonstrated promising results for continuous vitals monitoring [17, 18, 19, 29, 30], such systems can be expensive and require auxiliary sensing hardware beyond what is installed in the bed itself. To deploy such systems, the sensor (often piezoelectric film) should be installed on existing hospital beds as an additional accessory. Periodic replacement of the sensor is then required due to the limited lifetime of the piezoelectric material, which can wear out in 1-2 years in some cases [31]. In addition, such single-channel systems can exhibit a substantial drop in coverage depending on the posture of the person on the bed or the location of the body with respect to the sensor [32].

Although BCG has demonstrated robust performance for estimating basic vitals, it still poses some challenges such as motion artifact, distortion in signal morphology caused by postural changes [33], and effective multi-channel fusion. BCG measurement systems are sensitive to the posture of the subject during the recording period, in that the signal shape may be distorted when the subject’s posture changes [33]. For bed-based BCG recordings, commonly used for long-term monitoring such as overnight sleep studies [34], changes in body posture are inevitable — subjects may lay supine for part of the night, then laterally for some time, then prone, for example. Moreover, bed-based BCG is even more susceptible to postural effects than standing BCG as the head-to-foot and dorso-ventral forces are unavoidably coupled together in the measurement [6].

For a multi-channel system, Bruser *et al.* [32] and Rosales *et al.* [35] have presented an

effective approach for optimizing the information from multiple channels, besides simply averaging multiple channels in the time-domain or individually processing each channel as done in previous studies. In those studies, it was demonstrated that multi-channel systems could outperform single-channel systems. Jiao *et al.* [15] proposed a multiple instance dictionary learning approaches to learn morphological characteristics of an individual's personal BCG heartbeats from a multi-channel hydraulic bed sensor system. Hai *et al.* [36] presented Gated Recurrent Unit (GRU) network-based framework for detection of heart-beat in BCG signals. In this work, segments of BCG signals were formulated as images and inputted into the GRU network. This approach achieved an effective fusion of multi-channel information, but subject-specific or globalized pre-training on a large amount of data recorded in a particular posture was required. Few studies have been published on signal processing approaches to utilize multiple-channel knowledge for improved estimations effectively.

1.3.2 Respiratory Monitoring

Respiratory diseases such as asthma and chronic obstructive pulmonary disease (COPD) pose a significant burden on public health [37, 38, 39]. More than 25 million people in the United States have asthma [40], and approximately 14.8 million adults have been diagnosed with COPD [41], the 4th leading cause of death in the United States. Respiratory diseases affect individuals and cause a high cost to the health care system, with annual healthcare expenditures for asthma alone estimated to be around \$20.7 billion [41].

Such respiratory diseases, characterized by various breathing disorder types caused by airway obstruction, could be diagnosed and prevented by continuous monitoring of lung

function [42, 43]. Continuous monitoring is essential for the early detection of respiratory disorders and thus reduces disease exacerbation leading to hospital admission [44, 45]. In clinical practices, spirometry is the most commonly used diagnostic tool for pulmonary function testing (PFT) [46]. Spirometry assesses the function of the patient's lung condition by measuring the velocity and volume of air the patient can breathe in and out. From the flow-volume loop graph of the spirometer, parameters such as peak expiratory flow (PEF) [47], forced expiratory volume in one second (FEV1) [48], and forced vital capacity (FVC) [48, 49] are obtained to evaluate the lung function. However, to obtain these parameters, patients need to perform forced breathing maneuvers multiple times [46]. This is not feasible for patients with severe airway obstruction and continuous long-term monitoring. Another widely used method to measure the volume of air inhaled and exhaled is whole-body plethysmography [50]. Although this does not require forced breathing, it still needs patients' attention to be used.

For long-term continuous monitoring of respiratory rate and volume, several methods have been proposed. Reyes *et al.* [51] proposed the use of a smartphone camera to monitor RR and RV. This study obtained a volumetric surrogate signal through the intensity changes in video channels that reflect the chest wall movement during breathing. Though a high correlation between the peak-to-peak amplitude of the video-based volume estimation and the spirometer volume signal was found, the work requires calibration on each subject. In [52, 53], RR and RV were estimated from a strain or inductance belt around the thorax and abdomen. This method requires tight tension of the belts to capture chest wall motion, thus leading to high error in some cases due to loss of tension caused by the postural changes. Also, this method requires subject-specific or posture-specific calibration. Radio-frequency

(RF) sensor also records surface motion caused by cardiac activity and breathing [54]. However, its signal-to-noise (SNR) is limited [55, 56], and the perfect alignment between the torso and the sensor is mandated [57, 58]. Sharma *et al.* [59] suggested RR and RV measurement by using near-field coherent sensing (NCS). NCS is a non-invasive sensor that transmits a low-power continuous wave (CW) RF signal into the body [60]. Unlike other unobtrusive sensors, the near-field coupling to internal dielectric boundary motion captures direct movements from the heart, lung, and diaphragm, and not just the surface motion. This method achieved a high correlation between estimated and ground-truth RR and RV with the subject- and posture-wise calibration.

The BCG has recently gained attention for its application in continuous non-invasive cardiovascular *and* respiratory monitoring systems. BCG is one of the cardiogenic vibration signals that measure changes in the center of mass of the body in response to the cardiac ejection of the blood [11, 6]. BCG comprises two components—the cardiac rhythm lies in a higher frequency range, and the respiratory component arising from respiratory movements lies in the lower frequency range [61].

Bed-based BCG systems are gaining momentum for use in respiratory monitoring due to their comfortable usage and capability for long-term measurements. Recent studies have indicated that such bed-based BCG sensing systems could robustly track changes in respiratory parameters while addressing the disadvantages of the aforementioned respiratory monitoring approaches in terms of usability [62, 63, 64, 14]. In particular, the RR monitoring with the piezoelectric-based sensor placed under the mattress has been widely validated and deployed in commercialized products for both at-home and hospital settings [19, 65].

Although a bed-based BCG system has been commercially deployed for RR monitor-

ing, estimating TV with BCG signals has not been explored intensively. Additionally, many bed-based BCG systems are single-channel systems with the sensor placed at the center, despite it being known from previous studies that multi-channel systems provide in-depth information and thereby a more robust estimation of physiological parameters [66, 32]. Isono *et al.* [67] demonstrated that with load cell signals, a wide range of RR can be accurately estimated regardless of posture. Though this study [67] did not evaluate load cell signals for the estimation of TV, it suggested a possible correlation to TV.

1.3.3 Blood Pressure

BP is one of the standard vital signs along with temperature, HR, RR, and oxygen saturation (SPO_2) [68]. Frequent measurement of BP, which closely correlates with arterial conditions and cardiac activities, plays an essential role in monitoring cardiovascular risk factors such as hypertension but is infrequently recorded outside of critical care areas in reality. Continuous monitoring of BP on a general medical-surgical unit may decrease the total length of stay in both hospital and intensive care unit days [69], reducing the number of cardiac arrests as well.

The current method of BP measurement relies on oscillometric cuff-based devices. While this method accurately measures the BP, the use of a cumbersome and inconvenient cuff limits the measurement to only a few times per day, therefore making continuous BP monitoring impossible [70]. To address this issue, several cuff-less BP monitoring systems have been developed. The most common approaches in the literature and in commercially available BP estimation systems for this purpose leverages the relationship between *PTT* and BP [22]. *PTT* is the time it takes for the pressure pulse to travel along the arterial wall

[22, 23]. PTT has an inverse correlation to BP that could be expressed with the Moens-Kortweg equation as follows [22]:

$$BP = \frac{K_1}{PTT} + K_2 \quad (1.1)$$

where K_1 and K_2 are subjected-specific parameters. To obtain PTT, the pulse wave needs to be measured at two arterial sites —and one proximal and one distal (far down the arterial tree such as radial artery) to the heart. Both the proximal and distal timing reference could be obtained non-invasively. Current technologies to measure the pulse at distal locations include PPG sensors on locations such as finger [24], wrist [25], and foot [26] due to their high-quality recordings and convenience. For proximal timing reference, measurements such as seismocardiogram (SCG) [71], and BCG [72] serve as a surrogate. SeismoWatch [25], is a watch-based system that obtains distal timing reference from wrist PPG and proximal timing reference from SCG. SCG measures the low-frequency thoracic vibrations due to mechanical movement of the heart induced by cardiac activity, and it requires an accelerometer to be attached to the sternum [6]. With Seismowatch [25], a user needs to press the device manually against the sternum. The scale-based system in [26] measures PTT while the person is standing on the scale, which measures BCG and has an array of PPG sensors on top. PTT is computed by taking proximal timing from BCG signals, and distal timing from the PPG signal sensed from the feet. This does not require certain maneuvers, like pressing the sensors against the chest. Su *et al.* [73] presented a bed-based hydraulic sensor system that captures relative blood pressure using the BCG signals from the bed alone without any extra sensor such as PPG. In [73], a high correlation

between the BCG-based features and ground truth BP was shown. Also, the study presented mean absolute error with the subject-specific calibration.

Besides the PTT or PAT, recent studies leveraged ML or DL models to non-invasively estimate the BP from BCG, ECG, and PPG signals. For traditional ML-based models, timing-related or morphological features derived from cardiac signals were commonly used as an input to the models to obtain BP predictions [73, 74, 75, 76, 77]. With the recent successes of DL models in other domains such as computer vision and speech processing, many attempts have been made for the end-to-end estimation of BP from other cardiac signals. Most studies deploying the DL architectures were done using the PPG signals only by leveraging the morphological similarity between PPG and arterial blood pressure (ABP) waveform [78, 79, 80, 81]. However, this approach may not be valid as the PPG waveform is also affected by the intravascular pressure, the distensibility of the vascular wall, and the oxygen content of hemoglobin besides BP [20].

1.4 Specific Aims and Contributions

While the early warning score system (EWS) has demonstrated its effectiveness in early recognition of patient deterioration and reducing preventable adverse events in hospitals, the intermittency in vital measurement has limited its capability. To address this problem, the BCG has been widely investigated as one of the non-invasive sensing modalities that could provide continuous vital estimations with the existing sensors (i.e., load cells) on the hospital bed. Though many studies have shown robust monitoring of cardiorespiratory parameters using the BCG signal, it poses some limitations as well — (1) susceptibility to motion artifacts and postural variability, (2) frequent calibration requirement due to person-

specificity.

This work explored the use of multi-channel BCG signals from the load cells embedded on the hospital bed to continuously monitor a complete set of vitals including HR, RR and TV, and the BP. Signal processing or ML/deep learning (DL) models were suggested in this work to improve the utilization of multiple channels and mitigate some known limitations of BCG-based cardiac monitoring.

The main contributions of this work are given below:

1. Demonstrated a signal processing-based method for robust estimation of HR from the hospital bed embedded load cells. Implemented a novel array processing algorithm that effectively selects and combines the load cell channels to optimize the fusion of multiple channels and further improve the HR estimation accuracy.
2. Demonstrated HR estimation using a DL model by translating the BCG signal to an interpretable waveform, from which HR can be derived through simple peak detection. Investigated advantages and disadvantages of two different HR estimation algorithms to accommodate various deployment scenarios.
3. Showed robust respiratory monitoring using the low-frequency component of the load cell recordings. Demonstrated improved performance in RR estimation by engaging multiple channels. In addition to RR, this work also showed the feasibility of estimating the respiratory volume (RV) using a tree-based ML model.
4. Demonstrated the estimation of BP using the BCG in combination with PPG from the pulse oximeters. Two different approaches were explored — 1) Conventional

PTT-based model and 2) the DL-based model. In the PTT-based approach, a signal processing pipeline was presented for robust extraction of PTT and BP values were estimated through linear regression. In the DL-based approach, we presented estimating the BP waveform through U-Net architecture and the calibration process to estimate BP values.

5. Validated algorithms on the data collected from human subjects study engaging perturbations that modulate target health parameters and multiple postures to elucidate model performance against diverse settings.

1.5 Thesis Organization

The objective of the proposed research is to establish continuous cardiorespiratory monitoring using the BCG signal recorded from an array of load cells embedded in a hospital bed. The remainder of this thesis is organized as follows: Chapter 2 discusses the estimation of HR using signal processing-based and DL-based model. Chapter 3 discusses respiratory monitoring using the low-frequency components of the load cell recordings, presenting results for RR and TV estimation. Chapter 4 presents the work related to BP monitoring, discussing two different approaches for extracting BP-relevant features from the BCG signals. Lastly, Chapter 5 concludes this work and provides directions for future work.

CHAPTER 2

HEART RATE ESTIMATION FROM BALLISTOCARDIOGRAM SIGNALS

In this chapter, two different algorithms to estimate HR from the multi-channel BCG signals are proposed to enable continuous monitoring of HR, one of the most common and important vitals in health monitoring. The two algorithms include the signal processing-based algorithm and the DL-based algorithm; both methods present a robust HR estimation performance, while each method poses different strengths and limitations. The first section discusses the signal processing-based method, where an algorithm to estimate inter-beat-interval (IBI) based on a probability density function (PDF) is presented. In addition, we proposed a novel array processing technique in this section to improve the existing PDF-based algorithm by optimizing the fusion of information from multiple channels. The second section discusses the DL-based method that estimates the HR through a simple peak detection on the triangular waveform generated by the DL model from the BCG signals.

2.1 Probabilistic Approach for Accurate Heart Rate Estimation using Ballistocardiogram from an Array of Load Cells in a Hospital Bed

2.1.1 Introduction

The BCG can be measured unobtrusively without any attachment of sensors or electrodes to the body. BCG measurement systems can be instrumented into various form factors including bathroom scales [12], chairs [13], and beds [14, 15, 16, 7, 8]. In hospital settings,

bed-mounted sensors can be deployed to capture BCG signals throughout the day while the patient is on the bed. Commercially available bed-based BCG sensing systems for both hospital and at-home settings include Emfit (Vaajakoski, Finland) [17], EarlySense (Ramat Gan, Israel) [18], and Beddit (Apple, CA, USA) [19] — all of which are systems providing a single channel of BCG output.

Though each bed-based BCG system demonstrated promising results for continuous vitals monitoring [17, 18, 19, 29, 30], such systems can be expensive, and require auxiliary sensing hardware beyond what is installed in the bed itself. To deploy such systems, the sensor (often piezoelectric film) should be installed on existing hospital beds as an additional accessory. Periodic replacement of the sensor is then required due to the limited lifetime of the piezoelectric material, which can wear out in 1-2 years in some cases [31]. Most importantly, as mentioned above, such single-channel systems can exhibit a substantial drop in coverage depending on the posture of the person on the bed or the location of the body with respect to the sensor [32].

To this end, the load-cell based BCG system described in this work has benefits over piezoelectric systems in that the BCG sensing hardware matches the lifetime of the bed, and the approach is cost-effective as load-cells are already embedded in many hospital beds to weigh patients or detect falls. These load-cells are often located in each of the four corners of the hospital bed, immediately allowing for multiple channel comparisons. This enables robust estimation of physiological parameters by broadening the spatial coverage of the system to capture the BCG signals and thus achieve high coverage, i.e., rejection of fewer signal segments. Though previous work [32, 35] has shown that multi-channel systems can outperform single-channel systems, many studies tend to focus on simply averaging

multiple channels in the time-domain or individually processing each channel. Also, in some studies [15, 36], subject-specific or globalized pre-training on a large amount of data recorded in particular posture was required. Few studies have been published on signal processing approaches for the effective utilization of multiple-channel knowledge for improved estimations. An approach for the effective fusion of multiple channels can not only be used for the multi load-cell systems but can be used for the multi-channel wearable BCG systems with Magneto-Inertial Measurement Unit (MIMU) sensors [82, 83], an array of fiber optic [84, 85] or optical sensors [86].

In this work, we demonstrate an improvement in HR estimation from bed BCG signals through a novel array processing technique to optimize the fusion of multi-channel information. The multi-channel HR estimation algorithm proposed in this work was based on the existing probabilistic approach-based IBI estimation and the Bayesian fusion algorithm developed with single channel BCG system [8, 32]. We present a selective fusion of channels according to the assessment of the PDF obtained from each channel using the method deployed from [8, 32]. To do so, we deploy a modified q -value to assess each PDF's reliability, in addition to Gaussian weights, to produce a weighted joint PDF. We evaluate the algorithm's performance with the array processing against existing multi-channel and weighted multi-channel fusion methods on the data collected from 25 healthy subjects with the hospital bed. We validate the improvement in HR estimation using our method by analyzing statistical significance and postural effects. We also present analysis on the heartbeat interval estimation results on a beat-to-beat level.

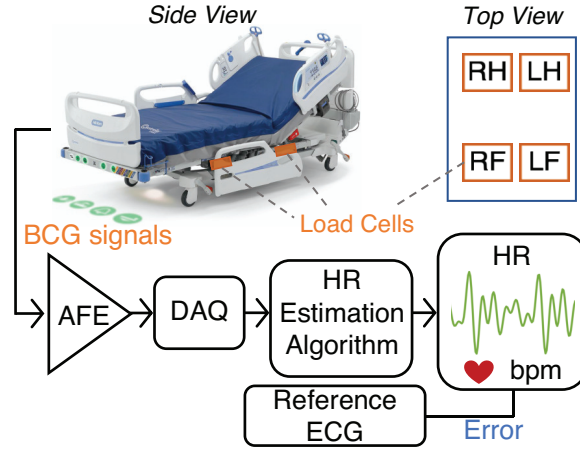


Figure 2.1: Overview of the study and the test setup. Four load cells are located on the four corners of the bed frame (RH - right head channel, LH - left head channel, RF - right foot channel, and LF - left foot channel of load-cell BCG signals, load cell locations are colored as orange in the top left picture). Load-cell outputs are amplified using a custom-designed analog front end (AFE) to obtain BCG signals. BCG signals are used to estimate heart rate (HR) and are validated against ECG.

2.1.2 Methods

2.1.2.1 Human Subjects Study and Instrumentation

Eleven subjects (Male: 6, Female: 5; Age: 27.8 ± 4 ; Weight: 71.54 ± 19.5 kg; Height: 172.27 ± 12.3 cm) without any known history of cardiovascular diseases were recruited for the human subjects study. The study was conducted under the approval of the Georgia Institute of Technology Institutional Review Board (IRB). During the protocol, each subject laid down in a relaxed position on the patient bed (Centrella®, Hill-Rom, IL, USA) shown in Figure 2.1. Subjects were asked to lay in five different postures, including supine, left and right lateral, prone, and seated, for one minute each. The seated posture required the bed to be adjusted to the seated configuration with the head angle of 64° .

To obtain BCG signals, the outputs from the four load cells located on the four corners of the bed frame — left / right of head and foot — under the mattress were fed into

a custom-designed analog front end (AFE). Although the technical specifications of the load beam embedded in the Centrella® bed are not publicly available, it can be referenced by its internal part number 137757. The AFE is consisted of an instrumentation amplifier, a Sallen-Key low-pass filter and a non-inverting gain stage similarly to prior work [87]. Along with the BCG, three electrodes were placed on each subject's chest in Lead II configuration to acquire the ECG signals using a wireless amplifier (BN-EL50, Biopac Systems, CA, USA). The ECG signal was recorded to acquire a *ground truth* HR comparison for the evaluation and was not required for the actual implementation of the BCG-based HR estimation. A 16-bit data acquisition unit (DAQ, MP150, Biopac Systems, USA) was used to simultaneously record the BCG and ECG signals. All signals were originally sampled 2 kHz, but BCG signals were downsampled to 80 Hz to account for the limitation in sampling rate for many embedded systems where the approach in this study would work in the future. However, the downsampled BCG signals were linearly interpolated to 1 kHz for the inter-beat-interval analysis. Interpolation is required for the inter-beat-interval analysis in millisecond resolution and is not required for window-based HR estimation. The reference ECG signals were kept at the original sampling rate of 2 kHz, as they were used for the evaluation purposes only in this work.

For further testing, another set of data was collected from fourteen healthy subjects (Male: 9, Female: 5; Age: 26.21 ± 2.99 ; Weight: 65.29 ± 11.61 kg; Height: 171.43 ± 9.84 cm). During this protocol, the subjects were lying on the Centrella® bed in a supine posture. Subjects remained still and relaxed for the first three minutes and then read a given script out loud for two minutes to introduce artifacts caused by talking. BCG and ECG signals were simultaneously recorded with the same MP150 DAQ at a sampling rate of 1 kHz.

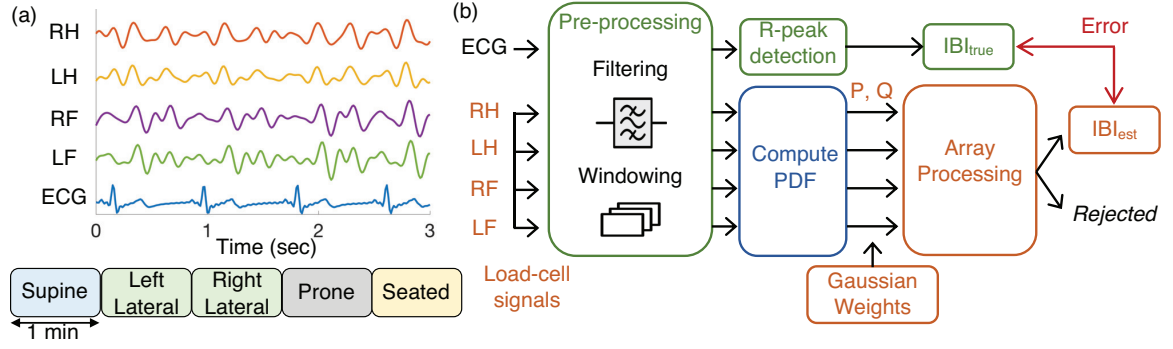


Figure 2.2: (a) Top: An example of the recorded BCG and ECG signals. RH - right head channel, LH - left head channel, RF - right foot channel, and LF - left foot channel of load-cell BCG signals. Bottom: The experimental protocol consisting of five different postures, each lasting for a minute. (b) A block diagram of the HR estimation algorithm composed of three parts—pre-processing, computation of PDF, and load-cell channel array processing.

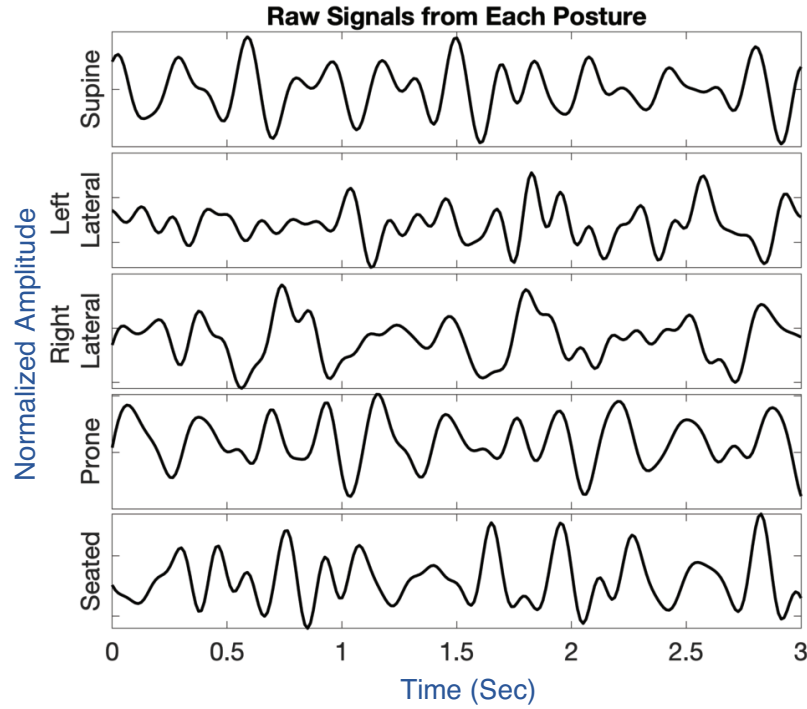


Figure 2.3: An example plot of raw BCG signals measured in each posture.

2.1.2.2 Pre-Processing

All signals were pre-processed, as shown in the block diagram in Figure 2.2(b). BCG and ECG signals were filtered using a finite impulse response (FIR) band-pass filter with

Kaiser window. Cut-off frequencies were 1-40 Hz for ECG, and 0.5-12 Hz for BCG [88, 10]. R-peaks of the ECG were found using a simple threshold peak detection method, and the intervals between those R-peaks were used as a reference for inter-beat intervals.

For both BCG and ECG, one-minute recordings of each posture were segmented into a 3-second long window as shown in Figure 2.2(a). An example plot of raw BCG signals from each posture is also provided in Figure 2.3. The incremental time shift between consecutive windows was 0.1 seconds. A short time shift of 0.1 seconds may not be necessary for the HR estimation but used in this work for the heartbeat interval estimation discussed in Section 2.1.2.4. The window size was chosen as 3 seconds to ensure that each window includes at least two heartbeat cycles assuming 1.5 seconds (40 bpm) as the maximum heartbeat interval. The HR range was assumed as 40 - 150 bpm in this work, considering the setup of bed-based system where subjects were staying relaxed while lying on the bed.

Heart Rate Estimation Algorithm

The HR for each window was estimated by finding the window's averaged IBI. The algorithm in this work was based on previous studies [8, 32, 89, 90] from other research group done with different BCG systems, usually a single channel piezoelectric-based system. The main contribution of this work has been done on the optimization of multi-channel information using a novel array processing algorithm that selectively combines the channels through assessment of probability density functions (PDFs). Details on the definition and derivation of PDF deployed in this work are discussed in the following subsection. The algorithm comprises six steps, as will be explained in the following sections. A brief overview of the procedure is shown in Figure 2.2(b). None of the steps except the beat-

to-beat interval estimation in Section 2.1.2.4 require post processing; the estimations were made based on only the past and current windows, unlike post processing algorithms that assume that the data from the entire recording period is available.

Computation of Probability Density Function (PDF)

For the IBI estimation, the probabilistic approach in [8] was deployed. Given a window with a length longer than two times the maximum possible IBI, this method computes the likelihood for each candidate IBI being the true heartbeat interval of the window. In this work, the range of candidate IBI's was set to $[400 - 1500]$ ms with the resolution of 1 ms. The algorithm computes three time-domain local estimators, namely — adaptive-window autocorrelation (Corr), adaptive-window average magnitude difference function (AMDF), and maximum amplitude pairs (MAP). Three local-estimators are then combined to obtain the joint PDF, and the IBI estimate \hat{T} is given as follows:

$$\begin{aligned} \mathbf{p} &= P(N \mid Corr, AMDF, MAP) \\ &= P(N \mid Corr) \cdot P(N \mid AMDF) \cdot P(N \mid MAP) \end{aligned} \tag{2.1}$$

$$\hat{T} = \underset{T}{\operatorname{argmax}} P(N \mid Corr, AMDF, MAP) \tag{2.2}$$

This algorithm was initially implemented and validated for single-channel BCG signals [8]. However, the later study, [32], demonstrated an improvement in performance with a multi-channel extension which computes and combines $3N$ estimators (three local-

estimators/channel \times N channels) from all N channels through Bayesian fusion.

Gaussian Weight Curve

To make the algorithm more robust to the sudden corruption of BCG signals caused by motion artifacts, the obtained PDFs $P(P \in \mathbb{R}^{N \times 4}, \mathbf{p}_c \in P, c = \text{channels})$ were weighted according to the distance between the reference value (ref_i) and each candidate IBI (IBI_{cand}). Note that the reference value (ref_i) here was computed from the previous estimations made using BCG signals a few seconds before the current window i , and does not require reference ECG signals. A similar approach was taken in other studies [89, 90], but the reference value (i.e., the center of the curve) was computed differently. Additionally, rather than applying the weights during the post-processing as done in [89, 90], the weights were computed and applied *online* in this work. The reference value (ref_i) for window i was determined as the exponential moving average of the most recent 50 estimations before window i . Accordingly, the method described here can be implemented in near-real-time for immediate display of HR for caregivers. The Gaussian weight curve for window i is given as follows.

$$w_i = \frac{1}{2k} - \exp\left(\frac{|ref_i - IBI_{cand}|}{2k'}\right)^2 \quad (2.3)$$

$$ref_i = ema(IBI_{est, (i-50:i)})$$

The parameters k , and k' were heuristically determined so that the curve width at 0.5

becomes approximately 700 ms. Among the recent 50 estimations, only the ones that meet all the criteria in Section 2.1.2.3 were included. The exponential moving average length was set to 10, to place more weight on estimations closer in time to the current window.

Additional possibly incorrect previous estimations were removed if the variability between the minimum and maximum estimations in the previous 50 IBI estimations was greater than 500 ms. In such cases, the points that lay outside the $[5 - 95]$ percentile range were rejected before computing ref_i . The computed Gaussian weight curve was only applied to PDFs when there were more than 50 robust previous IBI estimations. Raw PDFs were used before a sufficient number of solid estimations was obtained.

2.1.2.3 Load-Cell Array Processing

PDF Assessment

The quality of weighted PDFs from each channel was assessed based on the q -values, the ratio between the maximum peak height and the area of the curve, as described in [89]. Ideally, a robust PDF should only have one prominent peak for the most likely candidate IBI. However, as shown in Figure 2.4, a noisy signal can result in multiple peaks at multiple candidate IBIs in the PDF. The most likely candidate IBI chosen from such a PDF may not be reliable, resulting in a significant estimation error. In the example shown in the plot, all channels but the left hand show unreliable IBI estimations, resulting in the most likely IBI substantially differing from the true IBI shown as the red vertical line.

Having multiple peaks in the PDF leads to smaller q -values in general due to increased area under the curves. However, to further penalize the case where the PDF contains mul-

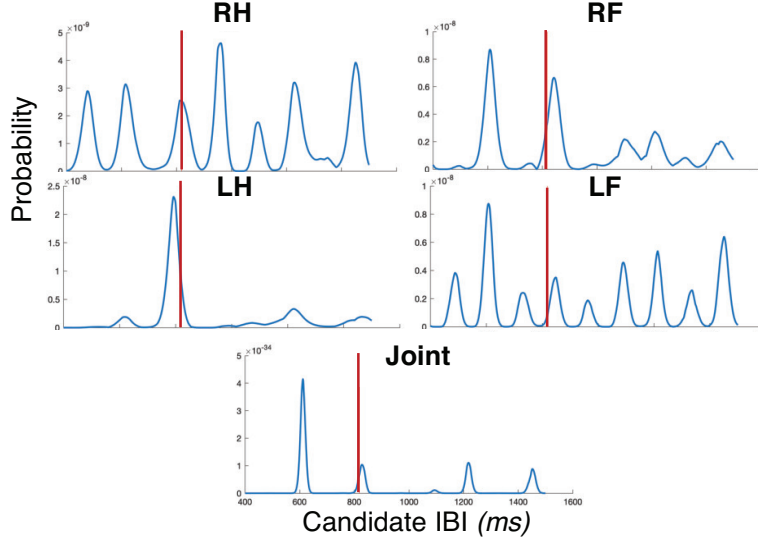


Figure 2.4: An example plot of PDFs from each channel.

multiple peaks, the q -values were adjusted by the number of prominent peaks found. Here, the prominent peaks were defined as peaks with a peak height of over 70% of the maximum peak in the PDF. Note that only the candidate IBI with the maximum peak was used as the final IBI estimation, and the other peaks detected were used to count the number of peaks in the PDF and adjust q -values. The following expresses the computation of the q -value for channel c (q_c), given M_c as the number of prominent peaks and $\mathbf{p}_c \in \mathbb{R}^N$ as the PDF.

$$q_c = \frac{1}{M_c} \cdot \frac{\max(\mathbf{p}_c)}{\sum_{j=0}^N \mathbf{p}_c(j)} \quad (2.4)$$

Channel selection and combination

After the q -values from all four channels $Q = [q_1, q_2, q_3, q_4]$ were calculated for a window, the window and channels were selected according to the following criteria:

Criteria 1 (window selection): At least one q -value from the four channels must be larger than the threshold. The threshold was determined heuristically such that a reasonable amount of coverage was maintained through the trade-off analysis between q -value threshold and the coverage and the error as shown in Figure 2.8.

$$\max(Q) > Q_{threshold} \quad (2.5)$$

Criteria 2 (channel selection): Channels must have a q -value over 70 % of the maximum q -value among the four channels for the window

$$\{c \mid q_c > \max(Q) \times 0.7\} \quad (2.6)$$

First, a window i that does not meet criteria 1 was considered to have unreliable PDFs for all channels and rejected. If the window met the first criteria, the channels with relatively large q -values were selected based on criteria 2 and combined via a Bayesian approach.

The IBI estimation was obtained as the candidate IBI at which the combined probability is the greatest. The remaining channels that were not selected were also combined to obtain a secondary IBI estimation in case the first IBI estimation deviated significantly from the reference value (ref_i). The primary and secondary IBI estimations are denoted as IBI_{est1} and IBI_{est2} respectively.

Determine the Final IBI Estimation

As the last step to prevent large estimation error, the absolute differences between the ref_i , the center of the Gaussian weights computed as the exponential moving average of previous estimations from BCG signals, and the primary and secondary IBI estimations were checked. By default, the algorithm chooses the primary IBI estimation as the IBI estimation. However, if the secondary IBI estimation shows an absolute difference much smaller than that of the primary IBI estimation — by 250 ms — then the secondary IBI estimation is selected as the final IBI estimation. This is to prevent the case where a highly selective PDF with high q -value prefers a prominent peak with candidate IBI seriously differing from the true IBI.

The array processing procedure in Section 2.1.2.3 is summarized in Algorithm Algorithm 1.

2.1.2.4 Heartbeat Interval estimation

Based on IBI estimations from the algorithm above, possible heartbeat locations were found as done in [8]. For each window i , given the center of the window as W_{mid} , the maximum peak within the range of $[W_{mid}, W_{mid} + IBI_{est,i}]$ was found and denoted as the anchor point J_i . Detected anchor points can be considered as possible locations for the BCG J-peak, the maximum peak in BCG heartbeat following the ECG R-peak.

As the PDF estimation algorithm was built on the assumption that each window includes at least two heartbeat cycles — one on each side of the window center — the esti-

Algorithm 1 Load-cell Array Processing

Input: P, ref_i , Gaussian curve w_i **Output:** $IBI_{est,i}$

```
1: for each window  $i$  do
2:    $Q = assessPDF(P)$  ▷ Get  $q$ -values
3:
4:   if  $\max(Q) < Q_{threshold}$  then ▷ Criteria 1
5:     Reject window  $i$ 
6:   else
7:      $selected = \{c \mid q_c \geq \max(Q) * 0.7\}$  ▷ Criteria 2
8:      $remaining = \{c \mid c \notin selected\}$ 
9:
10:    for each channel  $c$  do ▷ Channel combination
11:      if  $c \in selected$  then
12:         $joint1 \leftarrow joint1 \cdot P(c)$ 
13:      else
14:         $joint2 \leftarrow joint2 \cdot P(c)$ 
15:      end if
16:    end for
17:    ▷ Get estimations from joint probabilities
18:     $joint1 \cdot w_i \rightarrow IBI_{est1}, d_1 = |IBI_{est1} - ref_i|$ 
19:     $joint2 \cdot w_i \rightarrow IBI_{est2}, d_2 = |IBI_{est2} - ref_i|$ 
20:     $IBI_{est,i} = IBI_{est1}$  ▷  $IBI_{est1}$  as default
21:
22:    if  $d_2 < d_1 - 250\ ms$  then ▷ Final IBI estimation
23:       $IBI_{est,i} = IBI_{est2}$ 
24:    end if
25:  end if
26: end for
```

mated IBI reflects the interval between the heartbeat pair around the window center. As a result, it can be assumed that the second J-peak of the heartbeat pair would exist no further than $IBI_{est,i}$ from the window center.

Due to the short time shift of 0.1 seconds between windows, the same anchor point would appear multiple times across a few consecutive windows. Given the minimum interval between heartbeats set as 400 ms, 0.1 seconds would be short enough to have the same anchor point appearing multiple times while allowing enough time to process each window for the real-time processing that could be implemented in the future. The anchor points detected in three or more windows were considered as the final J-peak candidates. The estimated IBIs of each J-peak candidate were then averaged together for heartbeat interval analysis. Let the averaged IBI's and the anchor point be denoted as $[T_k, J_k]$, ($T_k = \overline{IBI_{est,k}}$, $k \in \text{J-peak candidates}$). For the anchor point detection procedure, a “virtual” single channel was created by subtracting the foot channels from the head channels — $(RH + LH) - (RF + LF)$ — as done in [67]. The anchor points above were detected in the “virtual” channel using the IBI estimated from the multi-channel algorithm. The anchor point detection method is described in more detail in [8].

To remove possible false-positive J-peak candidates, points that have a significant difference between the averaged IBI (T_k), and the actual J-J distance ($J_k - J_{k-1}$) were removed. For the evaluation, pairs of $[T_k, J_k]$ were mapped to corresponding ECG R-peaks and R-R intervals. Note that for heartbeat interval estimation, a few seconds of short look-ahead is required.

2.1.3 Evaluation

2.1.3.1 Window-Based HR Estimation

Evaluation Scenarios

The performance of window-based HR estimation was evaluated for three different scenarios to investigate the effects of array processing. The three scenarios include — 1) multi-channel fusion [32], 2) weighted multi-channel fusion, and 3) our algorithm, weighted multi-channel fusion with the array processing. For all scenarios, the signal segments with motion artifacts were removed with the same criteria. Each scenario was performed as follows:

- **Scenario 1:** Multi-channel fusion

The IBI was estimated from the joint PDF computed through the Bayesian fusion of all four channels.

- **Scenario 2:** Weighted multi-channel fusion

The joint PDF was computed through the Bayesian fusion of all four channels. The joint PDF was then weighted by the Gaussian curve described in Section 2.1.2.3

- **Scenario 3:** Weighted multi-channel fusion with array processing

PDFs from the four channels were processed via array processing as described in Section 2.1.2.3. The array processing includes the application of Gaussian weight curves, assessment of PDFs via q -values, and some rejection criteria for quality assurance.

For the analysis of the postural effects on HR estimation, the errors were evaluated by

postures for all cases.

Error Metrics

The reference ECG was used to validate the HR estimated with the load-cell BCG signals. The ECG R-R intervals in the window were averaged together and served as the ground truth averaged IBI interval ($IBI_{ECG,i}$). Note that there is always a delay between ECG and BCG, and there could be multiple heartbeat pairs in the window. Therefore, sometimes it could be unclear which heartbeat pair was reflected in the IBI estimated from BCG. The average of R-R intervals in the window was used as the ground truth rather than a single R-R interval in the window to address this problem. Ground truth HR of the window i was then computed as:

$$HR_{ECG,i} = \frac{60}{IBI_{ECG,i}} \quad (2.7)$$

The HR estimation ($HR_{BCG,i}$) was computed in the same way with estimated IBIs from BCG. The error between the ground truth and estimation was reported in mean absolute error (MAE, Unit: beats per minute (bpm)), and percent error (%), along with the coverage (%). The coverage here measures the ratio of the number of windows processed after rejection to the total number of windows, indicating how much time the system has covered over the total recording period.

2.1.3.2 Heartbeat Interval Estimation

For the validation of the heartbeat interval estimation, each J-peak candidate (P_k) was mapped to the closest ECG R-peak and the corresponding R-R interval. The averaged estimated IBIs (T_k) paired with each J-peak candidate were compared against the mapped ECG R-R intervals. The MAE in ms along with the width of the limits of agreement ($[5 - 95]$ percentile range) are reported here.

Note that the detected J-peak candidates were not used to compute the heartbeat intervals but were used to map estimated IBIs to the corresponding ECG R-R intervals. For heartbeat interval estimation, the three local estimators and the PDFs estimate the interval of the heartbeat pair at the center of the window. Therefore, the R-peak pair around the center of the window of chosen as the ground truth heartbeat interval.

2.1.4 Results

2.1.4.1 Window-Based HR Estimation

Figure 2.5 shows the bar plots of percent error for each scenario and posture. Across all postures, estimation errors were lower in scenario 3 compared to the other two scenarios, at the average mean absolute (MAE) and percent errors of — 1.76 bpm (2.74%) for supine, 2.89 bpm (4.59%) and 3.03 bpm (4.63%) for lateral postures, 2.42 bpm (3.62%) for prone, and 2.98 bpm (4.56%) for the seated posture. Following scenario 3, scenario 2 achieved an average lowest MAE of 1.96 bpm for supine and highest of 4.33 bpm for the right lateral posture. The errors computed for scenario 1 were higher than those in scenarios 2 and 3 in all postures. For posture-wise analysis, the lowest errors were achieved in the supine

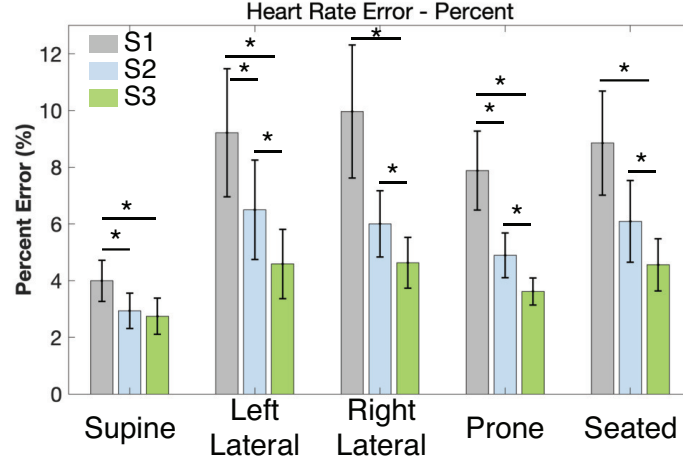


Figure 2.5: Bar plots of relative HR estimation error in percent (E_{rel}) for each posture and scenario. Scenario 1 (S1) - Multi-channel fusion; Scenario 2 (S2) - Weighted multi-channel fusion; Scenario 3 (S3) - Weighted multi-channel fusion with array processing

posture and the highest in lateral postures across all scenarios. Table 2.1 shows the detailed MAE values for each patient, scenario, and posture.

Statistical significance of the relative error (E_{rel}) and MAE was tested using a paired t-test with a 95% significance level to evaluate the differences in the error between each scenario. Comparing scenario 2 to scenario 1, the relative error and MAE were significantly decreased in scenario 2 for supine, left lateral, and prone postures, but not for right lateral and seated postures.

The relative error was significantly decreased in scenario 3 compared to scenarios 2 and 1 for all postures except one case — the difference between scenario 2 and 3 for the supine posture. Similar results were observed for the MAE, but the difference between scenario 3 and 1 in right lateral and seated postures was not significant, but close to significance with p -values of 0.07 and 0.05 respectively. Here, the mean coverage across all patients for each posture decreased in scenario 3 compared to the other two scenarios, but the coverage was still over 93% for all postures, which falls into a reasonable range of coverage in terms of

Table 2.1: Accuracy of Heart Rate Estimation - Mean Absolute Error, MAE (bpm)

Subjects	Supine			Left			Right			Prone			Seated		
	S1	S2	S3	S1	S2	S3	S1	S2	S3	S1	S2	S3	S1	S2	S3
1	2.53	1.66	1.55	4.55	3.55	2.97	12.37	10.58	8.16	7.60	5.29	3.58	9.01	7.62	6.02
2	3.65	2.05	1.98	7.83	3.62	2.25	7.78	2.86	2.68	5.57	3.86	2.84	5.26	3.96	3.21
3	3.65	2.35	1.52	1.22	1.08	1.04	0.80	0.74	0.73	1.33	1.17	0.94	13.43	11.73	6.64
4	5.19	1.74	1.46	17.68	13.46	4.38	27.14	6.81	3.50	15.84	2.08	1.50	18.87	1.69	0.91
5	1.21	1.02	1.02	2.09	1.71	1.61	3.84	2.57	1.86	2.74	1.95	1.68	1.17	1.17	0.95
6	2.52	2.30	2.24	5.24	3.43	2.79	2.95	2.94	3.04	4.22	3.42	3.07	2.14	2.14	1.59
7	1.02	0.69	0.64	5.69	2.16	1.12	5.07	3.68	2.15	1.41	1.20	0.94	3.22	1.90	1.28
8	1.71	1.71	1.72	5.56	4.07	3.60	3.48	2.89	2.01	1.95	1.88	1.75	4.70	5.00	3.54
9	5.37	4.94	4.92	13.83	11.49	8.98	8.52	6.33	4.96	4.99	3.90	3.32	4.93	3.75	3.73
10	1.67	1.51	1.36	1.21	1.21	1.22	2.05	1.56	1.63	7.84	6.24	3.07	6.24	4.15	3.80
11	0.98	0.98	0.99	1.86	1.85	1.80	4.05	3.33	2.64	9.26	5.05	3.96	1.22	1.05	1.06
Mean MAE (bpm)	2.68	1.91	1.76	6.07	4.33	2.89	7.09	4.03	3.03	5.70	3.28	2.42	6.38	4.02	2.98
SE (bpm)	0.48	0.34	0.34	1.60	1.26	0.69	2.24	0.85	0.61	1.30	0.53	0.33	1.65	0.97	0.61
Mean E_{rel} (%)	3.99	2.94	2.74	9.22	6.50	4.59	9.97	6.01	4.63	7.88	4.89	3.62	8.85	6.09	4.56
Mean Coverage (%)	99.81	99.85	98.69	97.16	97.51	94.48	98.38	98.96	95.50	99.50	99.69	97.86	97.57	97.92	93.86

The mean absolute error (MAE) of heart rate estimation is presented for each subject, posture, and scenario. The average of relative error (E_{rel} , %), and the coverage (%) is also given in the last rows. SE = standard error. MAE and SE were measured in beats per minute (bpm).

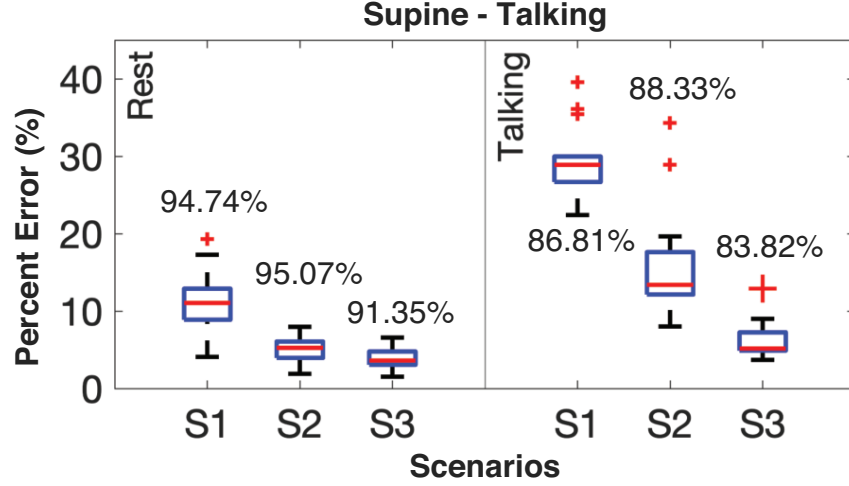


Figure 2.6: Box plot of relative HR estimation error in percent (E_{rel}) for an additional dataset. Scenario 1 (S1) - Multi-channel fusion; Scenario 2 (S2) - Weighted multi-channel fusion; Scenario 3 (S3) - Weighted multi-channel fusion with array processing; Rest-first 3 minutes of baseline recording, Talking-2 minutes of talking session. The coverage for each case is written above the bar.

Table 2.2: Accuracy of heartbeat interval estimation

Posture	$E_{abs}(ms)$			$P_5(ms)$			$P_{95}(ms)$			$(LoA, P_{95} - P_5)$		
	S_1	S_2	S_3	S_1	S_2	S_3	S_1	S_2	S_3	S_1	S_2	S_3
Supine	13.77	9.18	8.72	-12.50	-12.02	-12.00	14.60	13.03	13.70	27.10	25.05	25.70
Left	51.72	35.13	20.77	-149.90	-37.20	-26.00	152.80	26.40	20.32	302.70	63.60	46.32
Right	55.05	30.57	22.37	-37.70	-52.10	-28.15	351.70	23.00	20.00	389.40	75.10	48.15
Prone	39.96	20.11	15.37	-27.85	-25.57	-19.00	40.77	24.00	25.05	68.62	49.58	44.05
Seated	50.15	28.23	17.36	-81.75	-44.80	-27.57	309.45	33.00	19.02	391.20	77.80	46.60

The accuracy of heartbeat interval estimation is given in mean absolute error (E_{abs}), 5th percentile (P_5) of error, 95th percentile (P_{95}) of error, and the width of agreement ($P_{95} - P_5$). Errors are shown by posture and scenario.

usability.

The HR estimation performance was also tested on the additional dataset. As done in the first dataset, the performance was evaluated in three different scenarios as shown in Figure 2.6. For the rest period, the MAE was 2.47 bpm, with the percent error of 3.88% in scenario 3. The error was increased for the talking session compared to the rest period, MAE of 4.02 bpm and percent error of 6.33%, but the error was lowest in scenario 3.

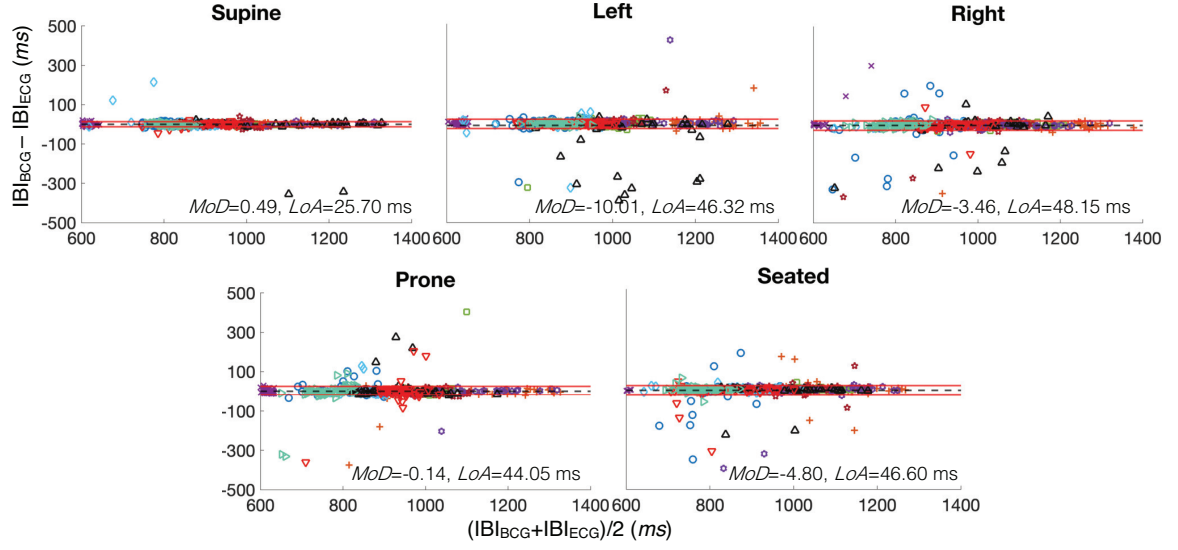


Figure 2.7: Bland-Altman plots for the heartbeat interval estimation shown by postures. Red horizontal lines indicate 5th (P_5) and 95th (P_{95}) percentile of error. Different marker colors indicate each subject. MoD = Mean of Differences, LoA = Limit of Agreement given as $P_{95} - P_5$

2.1.4.2 Heartbeat Interval Estimation

For further assessment of IBI estimations given by the algorithm, the estimated IBIs were evaluated for heartbeat interval estimation, as described in Section 2.1.3.2. Figure 2.7 shows the Bland-Altman plot for each posture in scenario 3. For each posture, around 526 heartbeat intervals were presented in the Bland-Altman plot. Statistics of the error distribution presented in Figure 2.7 such as the MAE (E_{abs}) and the width of limits of agreement given by the 5th and 95th percentiles of the error are shown in Table 2.2. Although not shown in Figure 2.7, the statistics of heartbeat interval error distributions are also given for the other two scenarios in Table 2.2. Similar to the HR estimation, a lower MAE and narrower width of agreement were achieved in scenario 3 in general. By posture, the lowest errors were achieved in the supine position with a MAE of 8.72 ms and width of agreement of 25.70 ms. Wider spread in errors was observed for other postures, as shown in

the Bland-Altman plots. With heartbeats from all postures together, MAE and the width of agreement were 16.66 ms and 38.98 ms, respectively. Although the direct comparison in performance would be challenging as it was evaluated on the different dataset, this is comparable to the state-of-art single-channel approaches from the literature. In the recent study [91], the MAE of 13.23 ms with coverage of 73.42 % in the healthy group and the MAE of 18.95 ms with coverage of 39.65 % in the patient group were achieved.

2.1.5 Discussion

The results for HR and heartbeat interval estimation demonstrate improvements in performance with weighted probabilities and selective channel combinations. The statistical significance in the difference between scenarios 2 and 1 for HR estimation shows that the weighted joint PDF reduces the error compared to using an unweighted joint PDF in general, except for the challenging postures — lateral and seated postures. The motivation behind weighted PDF is to reduce large deviations in IBI estimations among consecutive windows that could be caused by sudden motion artifacts and not by physiological changes. In subjects with normal cardiac rhythm, physiological parameters such as HR or heart rate variability do not change dramatically within 50 windows, which corresponds to 7.9 seconds [92, 93]. Thus, 8-second window lengths are commonly used in many HR estimation studies [3, 94]. Also, the challenging postures in scenario 2 implies a need for selective channel combinations for challenging postures to achieve a further reduction in the HR estimation error.

Although the 8-second window is common for HR estimation, a 3-second window was

used in this work for the following advantages. Using short windows could reduce errors and improve the coverage when few estimations from the neighboring windows are aggregated. For example, with the 3-second windows with the 1-second shift, eight windows correspond to 10 seconds. Taking the average (or median) of the “valid” ones among eight estimations could provide a more robust estimation while reducing the chance that the 10-second segment gets rejected compared to obtaining a single estimation from a 10-second window. Another motivation for using a 3-second window in this work was for the heartbeat interval estimation, which focuses on estimating the interval between a single heartbeat pair around the center of the window. The more beat pairs the window has, the more likely the estimation error would increase in the case of heartbeat interval estimation.

The statistical significance in HR estimation between scenario 3 and the other two scenarios, along with the heartbeat interval estimation error, demonstrates that the performance improvement resulted from the array processing combined with the weighted PDFs. Notably, the differences between scenarios 3 and 2 for postures except supine validates the further improvement achieved by adding an array processing procedure in the algorithm. For the supine posture, the error is already minimal in all scenarios, 2.68 bpm, 1.91 bpm, and 1.76 bpm, respectively. Therefore it is considered to be at the lower limit of the probabilistic approach. For the right lateral and the seated postures — seemingly challenging postures from the results in this work — scenario 2 could not achieve a significant reduction in error while the significance was observed with scenario 3. This result demonstrates that array processing further decreased the error in addition to Gaussian weights, either by rejecting the corrupted channels or windows in challenging postures that could result in distorted joint PDFs and thus high estimation error.

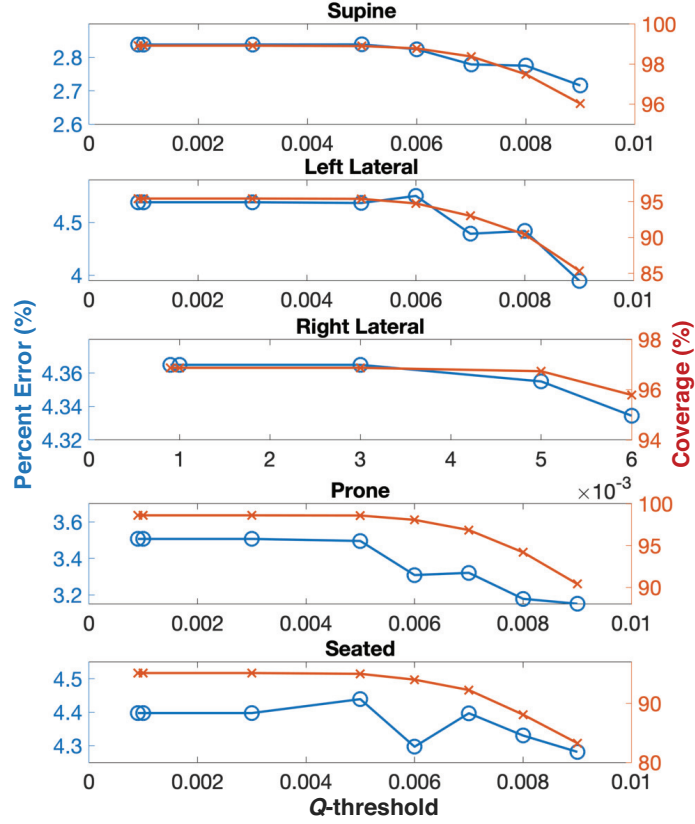


Figure 2.8: Coverage, percent error vs q -value threshold plot for each posture. Blue line with the left y-axis indicates the percent error (%). Red line with the right y-axis indicates the coverage(%). For both y-axes, the x-axis was set as the q -value threshold.

The coverage is also an important metric for the evaluation of HR and heartbeat interval estimation. Decreasing the error by excluding a large portion of the data is undesirable in terms of usability. However, having the capability to automatically detect and reject segments that contain heavily corrupted heartbeats from which any methods cannot make robust estimations is important. A small decrease in coverage for the array processing could have resulted from the rejection of such windows while maintaining the coverage at over 93% for all postures. The decrease in coverage was relatively large in the lateral and seated postures. However, the trade-off analysis between q -value threshold, coverage, and the error shown in Figure 2.8 indicates that the coverage could be improved (up to around

2% decrease in coverage compared to scenario 1 and 2) with performance comparable to reported values through threshold tuning.

Overall, the lowest errors were achieved in the supine posture and the highest in lateral postures across all scenarios for both HR and heartbeat interval estimation. This variability in HR estimation error across postures is expected, as the bed-based BCG is known to be susceptible to postural effects [6]. These are due to coupling of the head-to-foot and dorso-ventral forces in the BCG measurement depending on the person's posture on the bed. Moreover, the substantial decrease in signal quality in the seated posture in [33] provides a basis for the high estimation errors in the seated posture. Relatively high errors in the lateral and seated postures are shown across all scenarios in this work. Among the three scenarios, however, the lowest variability between each posture was observed in scenario 3, showing it is more robust to postural changes than the other methods analyzed.

Systems with multiple, spatially distributed sensors better capture the cardiac vibration signal and outperform the single-channel system in HR estimation, as demonstrated in [32]. The existing Bayesian fusion approach, which obtains the joint PDF by combining the PDF of each channel through element-wise multiplication, is shown to provide improved performance over simple time-domain averaging. The robustness of this existing method results from requiring all the channels, through multiplication in probability, to have high probability value in PDF around the candidate IBI chosen as the final estimation. However, this also suggests that having even one noisy channel with the PDF value of almost zero at the true IBI can zero-out the joint probability at that true IBI when combined with all other channels via the Bayesian approach. Depending on the posture or the location of the patient's body on the bed, it is likely that some portion of the channels are corrupted while

the others are not. Figure 2.4 shows an example of such cases. In this case, the left head channel alone has the most likely IBI at the true IBI, expressed as a red vertical line in the plots. However, the joint PDF computed by the Bayesian fusion of all channels, including the unreliable ones, resulted in the most likely IBI substantially differing from the true IBI, as can be seen in the plot. The assessment of PDFs using q -values in array processing could handle such cases and thus reduce the overall error.

The proposed algorithm in this work has shown significantly improved performance compared to the state-of-art methodology previously reported by Bruser *et al.* [8, 32]. We consider the algorithm from Bruser *et al.* the key work to compare against due to the fact that this work demonstrated robust performance in myriad settings, including with single-channel [8] and multi-channel systems [32], different sensor types (hydraulic [32] and electromechanical-film (EMFi) [90]) and diverse subject populations (including healthy and hospitalized subjects [90]). Additionally, an important advantage of the method is that it does not require training on massive datasets or any feature engineering based on a priori morphological knowledge of BCG signals which might not generalize in different postures, positions, and across subjects [8]. The improvement in performance upon the prior work from Bruser *et al.* thus demonstrates an important advancement of the state of the art in HR estimation from bed-based BCG recordings. Nevertheless, it should be noted that the performance of our algorithm in terms of mean absolute error ($\text{MAE} \leq 4 \text{ bpm}$) across posture and artifact-laden periods with short windows, is comparable or better than the results from many other recent studies [15, 36, 95, 62].

2.1.6 Conclusion

This study demonstrates robust estimation of HR and heartbeat intervals using BCG signals obtained from the four load-cell sensors embedded in a hospital bed. The array processing technique in this work significantly improves performance of the existing probabilistic approach-based IBI estimation by selective channel fusion/rejection via quality assessment and a Gaussian weight curve. The results suggest this technique further optimizes the benefits of a multi-channel system, which is already known to outperform a single channel system. In addition, postural error analysis validates the improved robustness of the method to postural changes.

The evaluation of this work was done with a data set collected in a lab setting over a short period of time, which limits the generalization of these results to actual use in hospital settings for a more extended recording period. Future work should be done with data collected from hospital settings through overnight study to validate the algorithm against real-world challenges. Additionally, the current study was tested on young and healthy subjects in stable condition. Future work should explore the broader population under various physiological conditions (i.e., higher HR), and include older subjects and patient groups with cardiovascular diseases to optimize the accuracy of the algorithm. The ability to continuously monitor HR and heartbeat intervals from patients in hospital beds with the methods described in this paper could ultimately provide breakthrough advances in early detection of patient deterioration, and reduce the need for more systems to be worn on the body. The robustness of the array processing approach to postural differences greatly enhances the translational potential of the work, since patients are not always in a supine

posture in hospital settings. Finally, leveraging load-cell sensors already embedded in commonly-deployed commercially available hospital beds (Centrella®, Hill-Rom) would allow for broad utilization of these methods in many settings, without the requirement for auxiliary sensing hardware to be purchased and maintained.

2.2 Estimation of Heart Rate using Ballistocardiogram Measured from Load Cells using a Deep Learning Model

2.2.1 Introduction

In this study, the probabilistic approach for estimating HR was explored in the previous section. The PDF-based model demonstrated a robust performance without requiring model training on a large amount of data or prior knowledge about the data. The pipeline can also be executed with low-complexity computations allowing the pipeline to be deployed on the devices with a limited computational capacity. However, there were heuristically determined parameters in the PDF-based approach such as the q-value threshold for rejecting noisy BCG channels, the width of the Gaussian curve, and the number of previous windows to generate a reference for the Gaussian curve. Such parameters would require further experiments on the data obtained from the real-world settings for the optimization.

To reduce error-prone hand engineering steps in the PDF-based HR estimation algorithm, in this section, the HR estimation using a DL model was also explored utilizing the three different datasets. The three datasets were collected across sub-aims including the respiratory dataset in Chapter 3, the BP dataset in Chapter 4, and the public BCG dataset in [96]. Similar to the in-house dataset collected in this study, the public BCG dataset also

includes 4-channel load cell BCG and the ground truth ECG measurements. The three datasets together resulted in a large amount of data, allowing a DL model to be trained, validated, and tested.

In this study, the U-Net architecture [97] was used to estimate the HR from 4-channel load cell BCG signals. To estimate HR, the BCG signals were translated to “transformed” ECG by the U-Net model, and from the generated waveform, the HR was estimated by detecting the peaks. The following section describes the method in detail.

2.2.2 Methods

2.2.2.1 Source/Target Signals

For the DL model, the 4-channel BCG signals were used as inputs (i.e. source signals) and the triangular waveform from the raw ECG signal (i.e. “transformed” ECG) was used as the output. Figure 2.9 shows an example of the source and target signals.

For each subject and posture, the time-series BCG, and the ECG recordings were first filtered according to Section 2.1.2.2 and then downsampled to 125 Hz. Here the downsampled signals were used instead of the original signals sampled at 1 kHz to reduce the dimension of the signal and accelerate the model training. Both the source and target signals were then segmented into 512-samples long (4.096 seconds) windows with 125 samples (1 second) overlap between the windows and each window served as a single training/testing instance for the model.

To generate the ground truth target signal, the raw ECG signal was transformed using the distance transform method[98, 99] as shown in Figure 2.10. The distance transform

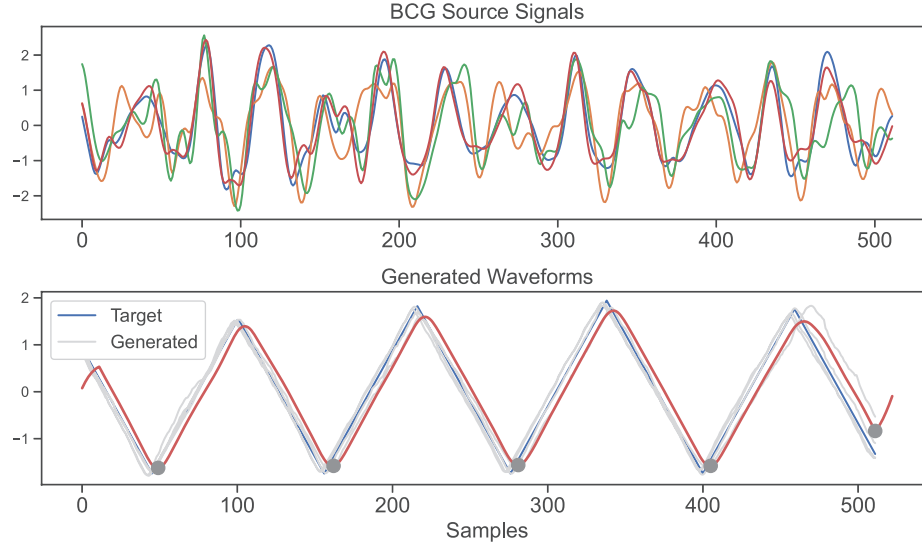


Figure 2.9: An example plot of the 4-channel BCG signals (Top) and the target/generated triangular waveform (Bottom). The ground truth target waveform is represented in blue and the grey lines show generated waveform from each channel. The red represents the average of the generated waveforms.

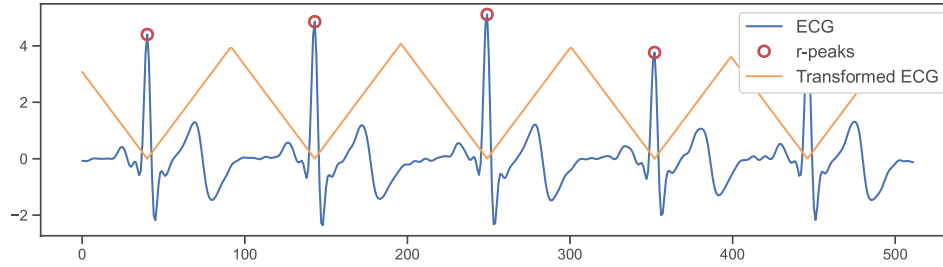


Figure 2.10: An example plot of the transformed ECG generated through the distance transform of the ground truth ECG recording. Yellow-Transformed ECG, Blue-Raw ECG, Red- ECG R-peaks

used here is commonly deployed for the computer vision tasks to compute the distance of each pixel to the closest boundary pixels. In this study, we computed the distance between each data point in the ECG signal to the nearest R-peak. The resulted signal forms a triangular shape where the valleys align with the true R-peak location. The “transformed” ECG signal was chosen as a target over the raw ECG signal itself or the binary labels (i.e. ‘1’ for the heartbeat regions and ‘0’ for non-heartbeat regions in the time-series recordings).

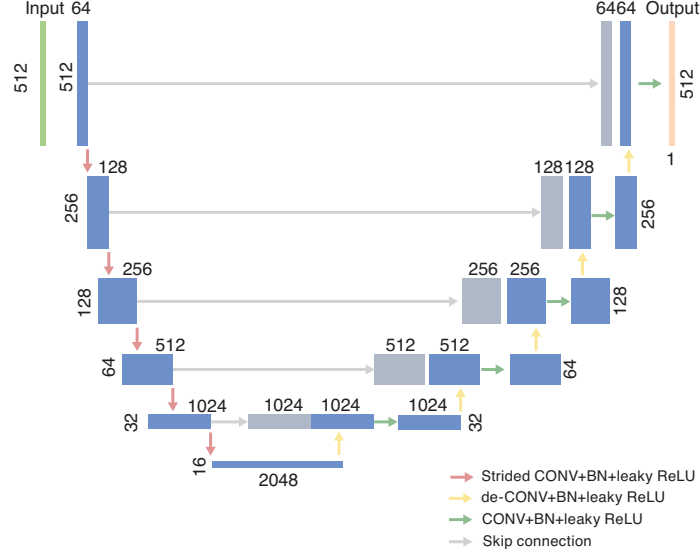


Figure 2.11: The overview of the U-Net architecture. The architecture has two parts: the contraction and the expansion path. The dimension of the signal is written on the left/right side of the feature map and the number of channels is written on the top of the feature map. CONV-1D convolutional layer, BN-Batch Normalization, leaky ReLU-leaky Rectified Linear Unit. Red: Strided CONV+BN+leaky ReLU, Yellow: tranposed CONV+BN+leaky ReLU, Gray: Skip connections

This was because a triangular waveform intuitively provides the locations of the heartbeats while not requiring the full ECG waveform and it can be easily generated from the raw reference ECG signals.

2.2.2.2 U-Net Architecture

The DL model used in this work was designed based on the U-Net architecture [97]. The overall architecture is composed of two parts—the contractive and expansive path—as shown in Figure 2.11. The contractive path implementation is similar to the original U-Net model in [97] which consists of cascaded blocks composed of convolution, batch normalization and non-linear activation. Instead of taking the stacked 4-channel BCG signals (i.e. $N_{mini-batch} \times 4 \times 512$) as an input, each BCG channel was used as an input to the model

(i.e. $N_{mini-batch} \times 1 \times 512$). Using each channel separately as an instance resulted in 4 times more data than using a stacked 4-channel BCG. Here, a single-channel model was chosen over a multi-channel model to handle the cases where some of the channels were heavily corrupted by the motion or completely lost due to connectivity issues when recording the signals. Also, though the multi-channel BCG monitoring system was used in this work, a single-channel BCG system is more common for at-home monitoring; a piezoelectric film sensor, for example. Therefore a single-channel DL model would allow the model to be deployed for the single-channel BCG measurement system as well.

The contractive path takes the 1-channel BCG signal as an input; thus the input has a dimension of $N_{mini-batch} \times 1 \times 512$, where 512 represents the signal length from the aforementioned windowing scheme. $N_{mini-batch}$ size was set as 40 in this study.

The contractive path reduces the dimension of the input by half while doubling the number of channels for each layer. Instead of using the max-pooling layer in the original U-Net, to reduce the dimension of the signal, a strided convolution (strided CONV) with stride of 2 and the kernel size of 11 were used in this work.

This was followed by a batch normalization (BN) to accelerate the model training and leaky ReLU (Rectified Linear Unit) as a non-linear activation. These alterations were chosen based on the previous signal-to-signal translation problems using U-Net-inspired DL architectures [100, 78, 81, 79]. The contractive path allows the model to learn a compact representation of the input data by recursively reducing the dimension while increasing the number of channels.

The expansive path mirrors the structure in the contractive path to restore the original signal dimension through transposed convolutions. Each layer first performs transposed

convolution on the output from the previous layer. It also takes the feature map from the corresponding layer in the contractive path through the skip connections and concatenates it with the output from the transposed convolution along the channel dimension. Then, convolution is performed on the concatenated feature map to halve the number of channels. Concatenating high-resolution features from the contracting path allows the model to better construct target signals during the expansive path.

For the final layers, instead of halving the number of channels, the channel dimension was reduced to 1 to output the final single-channel BP waveform. As done in the contractive path, the transposed convolution was followed by the BN and the leaky ReLU. In both the contractive and expansive path, the input to each layer was padded such that the dimension could be exactly doubled/halved from the previous input dimension. For the transposed CONV (yellow in Figure 2.11), the kernel size of 4 was used, and for the CONV (green), the kernel size of 11 was used. For both the contractive and expansive path, the slope of 0.2 was used for the leaky ReLU. In this work, 6-layer model was chosen based on the experiments and used for the following analysis.

2.2.2.3 Model Training and Testing

For the model training, the BP dataset in Chapter 4 and a publicly available BCG dataset in [96] (referred to as “public BCG dataset” in this work) were used. In both datasets, the ECG and 4-channel load cell BCG signals were recorded at a sampling rate of 1 kHz. All signals were then downsampled to 125 Hz before feeding into the model. For training, 35 subjects from the public dataset and 16 subjects from the BP dataset were used (i.e. 361560x4 instances). For the validation, 5 subjects and 3 subjects were included from the public BCG

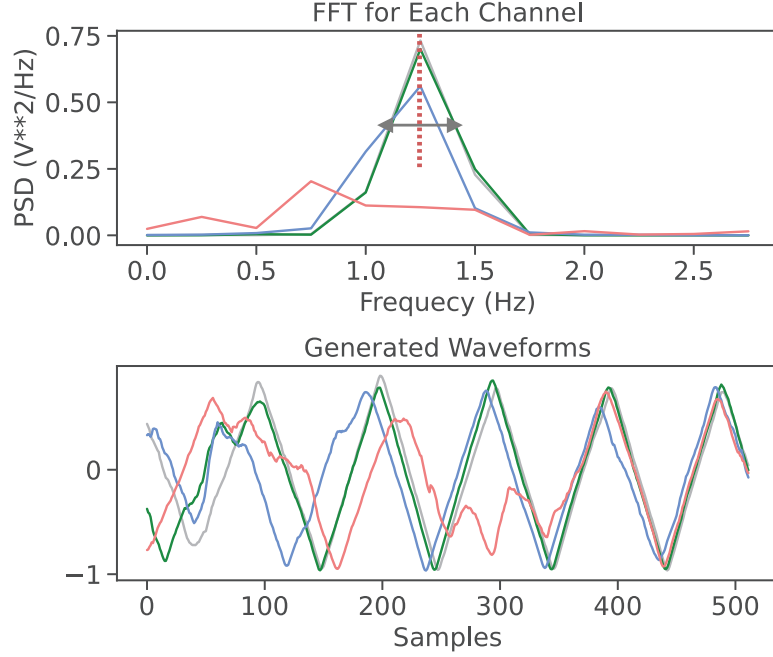


Figure 2.12: (Top) An example plot of power spectral density plot computed from the FFT. (Bottom) An example plot of generated waveforms from 4 different BCG channels. Each color indicates different channel. The channel colored in red in this example shows small SNR based on the top plot, therefore showing the low-quality waveform on the bottom plot.

and BP dataset (i.e. 74912 instances), respectively. For the testing, the respiratory dataset (15 subjects, 31200 instances) in Chapter 3 was used. In the respiratory dataset, subjects were performing some tasks to modulate the respiratory parameters; therefore relatively more motion artifacts were observed in the respiratory dataset compared to other datasets used in this work.

For training, a batch size of 40, an initial learning rate 0.001, and the Adam optimizer were used. The model was trained against the MAE between the generated and the target waveform. Before training, the source and target signals were normalized to zero mean and unit variance within the instance.

2.2.2.4 Channel Combination

To assess the quality of the generated waveforms, the Fast Fourier Transform (FFT) was computed on each waveform. The signal-to-noise ratio (SNR) was estimated by the power density centered around the dominant frequency divided by the total power in the cardiac frequency range (below 3 Hz). Figure 2.12 shows an example plot of the power spectral density computed from the FFT along with the corresponding generated waveforms where each channel is represented with a different color.

The SNR here quantifies the periodicity of the given signal segment—the higher the SNR, the stronger periodicity and the better signal quality. In the example in Figure 2.12, the channel colored in red shows a small SNR based on the top plot, therefore showing the low-quality waveform on the bottom plot. The SNR computation was done based on [101]. The channels with the SNR below the threshold were rejected and only the waveforms from the remaining channels were averaged together. When none of the channels met the SNR criteria, the window was rejected. These processes of assessing signal quality and selecting and combining the channels were done for each 512-sample long window.

2.2.2.5 Evaluation

For the evaluation, as done in the previous sections, the MAE between the estimated and true HR was computed. The results were analyzed by posture and task to assess the performance against the postural variability and the motion artifact which is particularly strong in certain tasks such as the deep breathing. In addition to MAE, the coverage was also computed to track the number of rejected windows.

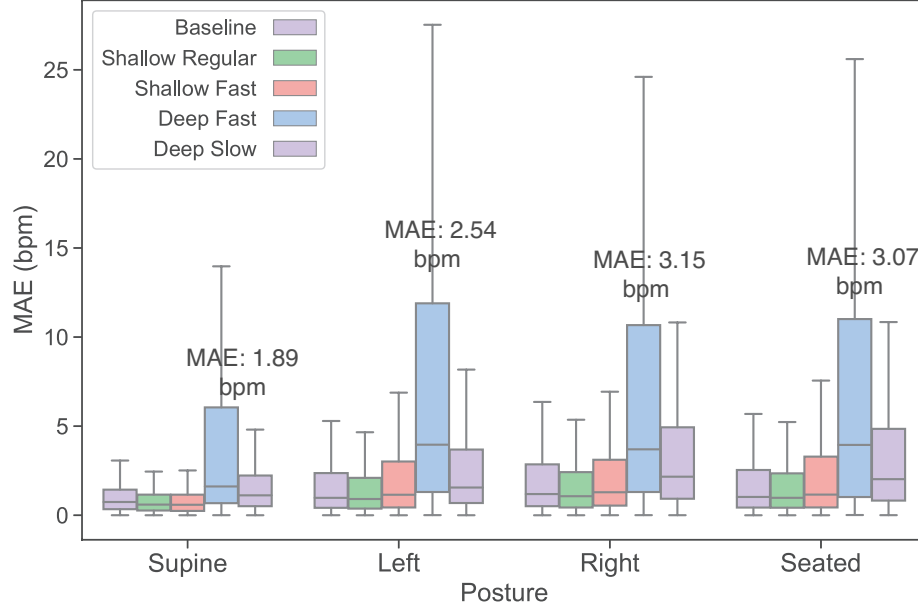


Figure 2.13: A boxplot showing the HR estimation error per posture and tasks. Each color indicates different respiratory tasks including baseline, shallow regular, shallow fast, deep fast and deep slow.

2.2.3 Results and Discussion

Figure 2.13 shows HR estimation accuracy by postures and tasks. In the SP dataset, more signal segments were affected by the motion artifacts compared to other datasets with the stationary tasks, particularly during the deep fast breathing sessions shown in blue on the plot. Overall, the error was lowest in supine with MAE below 2 bpm. Task-wise, overall, the MAE was below 3 bpm except the deep breathing. The error was larger in lateral posture as observed from the PDF-based algorithm as well. Across all postures and tasks, the coverage was around 91.36 %, indicating that 2696 instances out of 31200 testing instances were rejected through SNR thresholding. The single-channel model with the FFT-based thresholding resulted in improved accuracy and coverage than the multi-channel model.

In this section, we demonstrated the estimation of HR using the DL model by translating BCG signals to a more interpretable waveform. The DL model-based method has advantages in that it does not require complicated pre-processing steps or optimization of parameters such as the width of the Gaussian curve and the frequency of reference generation in the PDF-based method while demonstrating a robust HR estimation accuracy. When a large amount of data is available to train the model and the computational resource is not limited, the DL approach could provide a robust HR estimation model that generalizes well on real-world data with more motion artifacts.

2.3 Conclusion

In this chapter, algorithms for estimating HR from the BCG signals are proposed. The PDF-based algorithm in the first section demonstrated robust performance with the array processing steps to selectively combine the channels. The DL-based algorithm also showed a high HR estimation accuracy in a more end-to-end approach. Both methods demonstrated a strength against the postural variability by showing stable performance in some challenging postures. Two different methods presented in this section offer a variety of solutions that could be deployed based on the settings these technologies are deployed. The PDF-based method could be advantageous when the computational resource is limited. At the same time, the DL-model could outperform in a more realistic scenario with variability but has more computational capacity.

Relevant Publication

H. Jung *et al.*, “Accurate Ballistocardiogram Based Heart Rate Estimation Using an Array of Load Cells in a Hospital Bed,” *IEEE Journal of Biomedical and Health Informatics*, 2021, ISSN: 2168-2194. DOI: 10.1109/jbhi.2021.3066885

H. Jung *et al.*, “Quantification of Posture-Induced Changes in Bed-Based Ballistocardiogram,” in *Computing in Cardiology*, vol. 2020-September, 2020. DOI: 10.22489/CinC.2020.060

CHAPTER 3

ESTIMATION OF TIDAL VOLUME

The previous chapter investigated the algorithms for HR estimation using the BCG signals acquired from the load cells on the hospital bed. Force measurements from the load cells contain the cardiac and respiratory components after filtering out the high-frequency noise. The cardiac component, which lies in the frequency range of around 0.5 - 10 Hz corresponds to the BCG signal and the low-frequency component reflects the respiratory movement.

This chapter focuses on the low-frequency component of the load cell recordings for continuous monitoring of the respiratory parameters. We propose a globalized ML-based algorithm for estimating TV without the requirement of subject-specific calibration or training. A signal processing pipeline was implemented to extract features that capture respiratory movement and the respiratory effects on the cardiac signals. Through validation of TV and RR estimation accuracy on the respiratory dataset collected from the human subjects study, this study suggests that load cell sensors existing on the hospital beds can be used for convenient and continuous respiratory monitoring in general care settings.

3.1 Introduction

Respiratory failure is one of the leading causes of admission to the intensive care unit (ICU) from general hospital wards [103, 104, 105]. Especially with the emergence of the novel

coronavirus disease (COVID-19), early detection of respiratory failure has become more critical. To prevent adverse events and manage acute respiratory diseases, early detection of patient deterioration and applying the appropriate treatment on time is essential [106]. However, early prediction of respiratory failure could be challenging. In some instances, changes in the indicators of respiratory failure such as RR and TV could appear gradually; in other instances, these very same parameters could change dramatically and reach a life-threatening state in just a few minutes [107]. This mandates the continuous monitoring of such indicators.

Despite their importance, respiratory parameters are commonly overlooked by clinicians [108]. In general hospital wards, respiratory monitoring often relies on intermittent manual observation by healthcare providers [107, 109]. Clinical assessment based on such manual observations may lack precision compared to quantified assessments based on continuously measured physiological parameters. Additionally, the patient to caregiver ratio is much higher in general hospital wards, making it more likely that changes in critical indicators are not noticed by clinicians [110]. This has highlighted the need for alternative convenient and ubiquitous respiratory monitoring systems that do not add a burden on healthcare professionals.

The key parameters that characterize respiratory mechanics are RR and TV [111]. RR refers to the rate of breathing, commonly expressed as the number of breaths per minute (brpm). TV quantifies the depth of breathing and measures the volume of air inspired and expired in each breathing cycle. The normal range of RR and TV for healthy adults is 12 brpm and 0.5 L/0.4 L (male/female adult), respectively [112, 111]. The product of RR and TV derives minute ventilation (ME), a volume of air inspired or expired from a person's

lungs per minute. RR, TV, and ME play an essential role in determining a patient's pulmonary function and are used as criterion for diagnosis or prognosis of respiratory diseases, triage decisions, and early interventions.

Current clinical non-invasive respiratory monitoring includes spirometry [46] and body plethysmography [50]. Spirometry is considered the gold standard for pulmonary function tests, but it requires patients to perform certain maneuvers such as forced breathing under the guidance of clinicians. Body plethysmography is also commonly used in clinical settings; however, it requires bulky and costly sensing systems and for the patient to be attentive during the measurement. Both methods above are highly accurate but not suitable for continuous measurement.

The BCG has recently gained attention for its application in continuous non-invasive cardiovascular *and* respiratory monitoring systems. BCG is one of the cardiogenic vibration signals that measure changes in the center of mass of the body in response to the cardiac ejection of the blood [11, 6]. BCG comprises two components—the cardiac rhythm lies in a higher frequency range, and the respiratory component arising from respiratory movements lies in the lower frequency range [61]. Bed-based BCG systems are gaining momentum for use in respiratory monitoring due to their comfortable usage and capability for long-term measurements. Recent studies have indicated that such bed-based BCG sensing systems could robustly track changes in respiratory parameters while addressing the disadvantages of the aforementioned respiratory monitoring approaches in terms of usability [62, 63, 64, 14]. In particular, the RR monitoring with the piezoelectric-based sensor placed under the mattress has been widely validated and deployed in commercialized products for both at-home and hospital settings [19, 65].

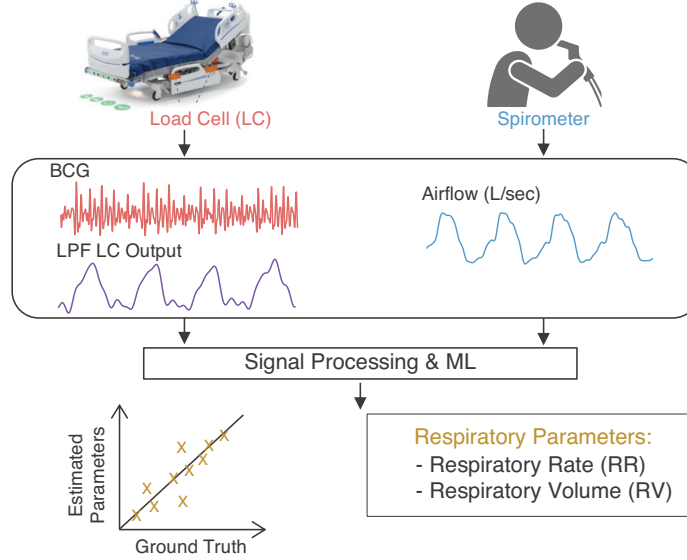


Figure 3.1: Overview of the study and the measurements. In the study, four load cell channels in the hospital bed (Centrella® bed) and the spirometer were recorded. Tidal volume (TV) was estimated with the machine learning-based regression algorithm using features extracted from the load cell signals. The model was evaluated against the ground truth TV values from the spirometer.

Although a bed-based BCG system has been commercially deployed for RR monitoring, estimating TV with BCG signals has not been explored intensively. In this work, we investigated the estimation of RR and the feasibility of monitoring TV using multi-channel load cell signals recorded with sensors embedded on a hospital bed. Figure 3.1 provides an overview of the study. We present a RR estimation algorithm that improves the performance by utilizing multi-channel information and a respiration quality index (RQI). To estimate TV, we present an end-to-end signal processing and machine learning-based prediction algorithm using features extracted from both the cardiac and respiratory components of load cell signals. For the computation of cardiac features, we deployed the multi-channel HR estimation algorithm from a previous study [66] for the segmentation of BCG signals into heartbeats, allowing for feature extraction without using reference ECG signals. For robust capture of 3D respiratory motion in any posture, we derived low-frequency force sig-

nals reflecting changes in the center of mass along the 3D axis of the bed. The performance of the algorithm was tested on data from 15 healthy subjects collected while performing a set of respiratory tasks in multiple postures, and feature importance was reported for interpretation of the results.

3.2 Related Work

As an alternative to traditional respiratory measurements, non-invasive sensing technologies have been studied for continuous respiratory monitoring as summarized in Table 3.1. Brüllmann *et al.* [52] investigated the use of a body garment embedded with a respiratory inductive plethysmography (RIP) sensing system for monitoring TV. The study evaluated the system in various postures and achieved a width of 95% limits of agreement (LoA) of 0.08 L with subject- and posture-specific calibration. Similar to RIP, Chu *et al.* [113] proposed a piezoresistive thin film that could be applied on the ribcage and abdomen to measures expansion and contraction of the chest. After subject-specific calibration, the system showed a width of LoA of 0.594 L for TV estimation, evaluated on a reclined position.

Impedance pneumography (IP), a recording of the variation in lung and thoracic bioimpedance measured from electrodes over the chest, is also well known to be correlated to airflow. Seppä *et al.* [114] demonstrated TV estimation error less than 3% across all postures and TV ranges (low/mid/high); and similarly, the correlation between the estimated and actual TV was $r = 0.95$ in [115]. Both studies utilized subject- and posture-specific approaches for calibration.

Fekr *et al.* [116] proposed an accelerometry system that could be placed on the ster-

Table 3.1: State-of-the-art Non-invasive Respiratory Sensing Methods

Paper	Sensing modality	Performance		Placement	TV Calibration
		RR (brpm / %)	TV (L / %)		
[52]	RIP belt	–	$m = 0, \sigma = 0.04$	Belt around the chest	Subject-specific
[113]	Strain sensor	–	$m = -0.077, \sigma = 0.15$	Sensor placed on the chest and abdomen	Subject-specific
[114, 115]	IP	–	$< 3\%$	Electrodes on the chest	Subject/Posture-specific
		–	$r = 0.95$		Subject/Posture-specific
[116]	Accelerometer	$0.05\% \pm 0.01\%$	$r = 0.87$	Accelerometer on the sternum	Subject-specific
[59]	RF	$r = 0.94$	$r = 0.84$	Belt around the chest and abdomen	Subject/Posture-specific
		$m = 0.047, \sigma = 2.93$	$m = 0, \sigma = 0.11$		
[117]	Doppler radar	–	$MAE = 0.07-0.19$	Antenna placed near subjects	Subject-specific
[51]	Camera	$m = -0.024, \sigma = 0.42$	$m = 0.014, \sigma = 0.18$	Camera placed near subjects	Subject-specific
		$RMSE = 0.41 \pm 0.18$	$RMSE = 0.18 \pm 0.11$		

The table summarizes the state-of-the-art sensing methods for non-invasive respiratory monitoring and their performance, placement, and calibration approach. For the performance, the values are reported in several different metrics including correlation (r), root mean squared error/mean squared error (RMSE/MSE) (brpm for RR, L for TV), percent error (%), and limits of agreement specified by mean difference m and standard deviation (σ) between the predicted and actual values. RIP: respiratory inductive plethysmography, IP: impedance pneumography, RF: radio frequency

num for monitoring RR and TV variability. The study particularly investigated its use for patients with pathological breathing such as tachypnea, bradypnea, Kussmaul, Cheyne-Stokes, and Biot’s. Overall, the system obtained an RR estimation error of $0.05\% \pm 0.01$ and Pearson correlation $r = 0.87$ for TV variability with subject-specific calibration. The wearable radio-frequency system in [59] is another example of a belt-type system that proposes RR and TV monitoring. In [59], the RF recordings were calibrated per subject and posture against the chest respiratory belt, and the correlation between the predicted and actual values was $r = 0.94$ for RR and $r = 0.84$ for TV.

Other state-of-the-art methods include non-contact systems that require sensors such as Doppler radar antennas [117] and cameras [51, 118] to be placed near the subject, rather than directly onto the body. Lee *et al.* [117] reported mean squared error (MSE) from 0.07 to 0.19 ml for TV across various breathing patterns and the camera-based systems [51] reported a width of LoA of 0.024 brpm for RR and 0.72 L for TV. The accuracy was evaluated with subject-specific calibration in all of the non-contact systems above.

While these respiratory sensing systems have shown feasibility as a surrogate for conventional clinical measurements, each method poses a challenge—in many cases, frequent calibration per subject or posture is required [52, 59, 51, 114, 117]. Additionally, sensors need to be attached to the patient’s body—tight skin contact is required to capture chest wall motion [52, 113, 59], or multiple electrodes need to be placed on the body [114, 115]. Therefore, in this work, we focus on the improvement of usability of the state-of-the-art methods—requirement of sensor placement and calibration per subject/posture for absolute TV estimation—while maintaining the performance comparable to the existing methods.

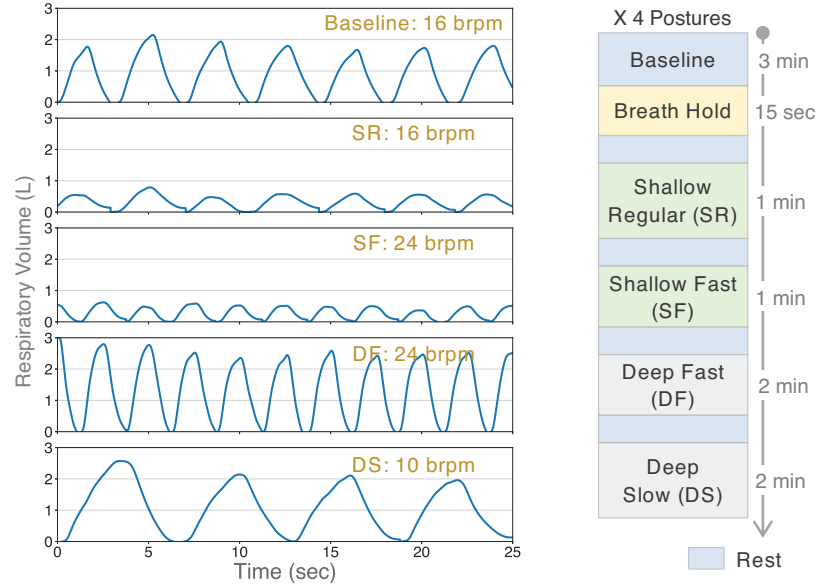


Figure 3.2: Left: An example plot of a respiratory volume waveform for each respiratory task. Right: An overview of the set of respiratory tasks performed in this study. The set shown here was repeated for four different postures.

3.3 Methods

3.3.1 Experimental Protocol

The human subjects study (H18452) was conducted under the approval of the Georgia Institute of Technology Institutional Review Board. A total of fifteen subjects (Male: 9, Female: 6; Age: 25.80 ± 3.30 ; Weight: 66.67 ± 12.40 kg; Height: 170.87 ± 12.4 cm) without known history of cardiorespiratory diseases were recruited for the study. Figure 3.2 shows the overview of the protocol. During the protocol, subjects performed a set of respiratory tasks to modulate respiratory rate and depth while lying on the hospital bed (Centrella®, Hill-Rom, IL, USA) shown in Figure 3.1. Additionally, the respiratory tasks were repeatedly performed in multiple postures, including supine, left lateral, right lateral, and seated. For the seated posture, the bed was adjusted to the seated mode, where the head-of-bed angle

was set to 45° with a slight foot drop.

The set of respiratory tasks included: 1) Baseline (BL, 3 min), 2) Shallow Regular (SR, 2 min), 3) Shallow Fast (SF, 1 min), 4) Deep Fast (DF, 1 min), and 5) Deep Slow (DS, 1 min). There was a short rest period (30-60 sec) between tasks to allow subjects to return to their baseline state. To effectively modulate the respiratory rate, subjects were instructed to synchronize their breath cycles to metronome beats played at a target respiration frequency. The metronome was set at 16 brpm for the baseline and regular breathing, 24 brpm for the fast breathing, and 10 brpm for the slow breathing.

Each respiratory task was aimed to simulate common normal/abnormal breathing patterns. Eupnea, referring to normal breathing patterns with an average rate of 20 brpm for adults, corresponds to the BL period in this work [112, 119]. SR and SF period simulates hypopnea (abnormally shallow breathing with or without an increase in rate) and tachypnea (rapid and shallow breathing) [112], respectively. Typically a breathing rate over the normal range is considered as rapid breathing, especially a rate greater than 30 brpm is defined as severe tachypnea [120]. Lastly, deep breathing tasks – DF and DS – were intended to simulate hyperventilation (rapid and deep breathing with an increase in both the rate and depth, resulting in an increase in minute ventilation) [121], and bradypnea (abnormally slow breathing with/without an increase in depth) [112].

Unlike respiratory rate, it is not straightforward to regulate TV in a quantifiable manner as the spirometer—the pneumotach sensor—records the airflow rate (L/sec), not the TV (L). Instead, subjects were trained before the actual recording to breathe at their comfortable depth during the baseline period and breathe intentionally shallower/deeper for the shallow/deep breathing tasks. In general, a decrease/increase in TV was observed for the

shallow/deep breathing, as shown in Figure 3.2.

3.3.2 Measurements

ECG, BCG, and the ground truth spirometer output were recorded during the protocol. For the ECG signal, adhesive Ag/AgCl electrodes were placed in lead II configuration. The ECG signals were amplified and acquired through a wireless module (BN-EL50, Biopac Systems, CA, USA).

BCG signals were acquired from the four load cells embedded on the Centrella® bed. The outputs from the load cells were amplified through a custom-designed analog front end (AFE) to obtain BCG signals as done in previous studies [66, 87]. To obtain the ground truth RR and TV values, the airflow from the spirometer (Pneumotach transducer TSD117A, Biopac Systems, CA, USA) was recorded for all respiratory tasks during the protocol. For accurate measurement, subjects wore a nose clip and breathed through a disposable mouthpiece attached to the spirometer.

All signals were recorded through an MP160 data acquisition system (DAQ, Biopac Systems, CA, USA) at the sampling rate of 1 kHz.

3.3.3 Pre-processing

Figure 3.3(a) shows an overview of the signal processing pipeline. All signals were filtered using a finite impulse response (FIR) filter with Kaiser window. The reference ECG signals were band-pass filtered with cut-offs of 0.5–22 Hz [88]. The load cell outputs were band-pass filtered with cut-offs of 0.5–9 Hz to obtain BCG signals [10]. The R-peaks in ECG signals were detected through simple thresholding and used as a reference to segment

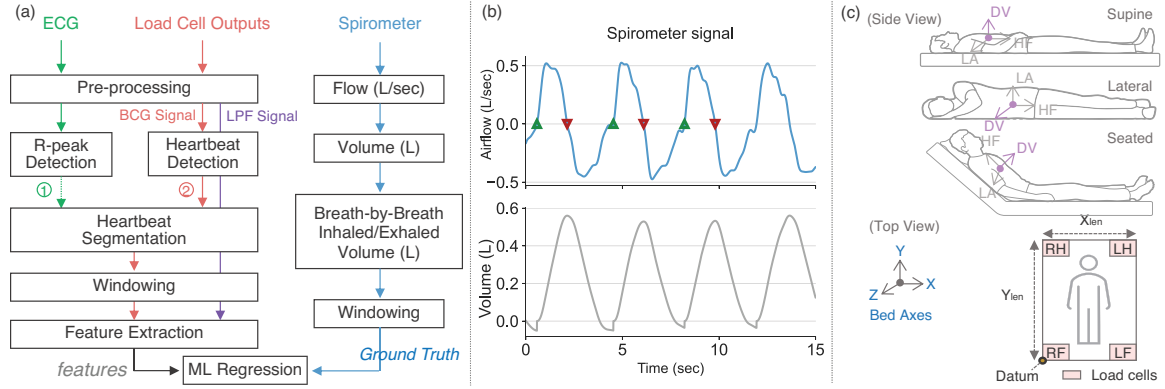


Figure 3.3: (a) A block diagram of end-to-end signal processing for the estimation of RR and TV. The left side shows the feature extraction from load cell signals, and the right side shows processing steps for ground truth spirometer measurements. (b) An example plot of the airflow (top) and volume (bottom) derived through the integration of airflow. (c) (Top: side view) Visualization of supine, lateral, and seated posture and corresponding body axes in each posture. DV: dorso-ventral, HF: head-to-foot, LA: lateral (Bottom: top view) The locations of the load cells and the datum for the derivation of changes in the center of mass. Red boxes represent the location of load cells. RH = right head, RF = right foot, LH = left head, LF = left foot. Datum is considered as RF.

the BCG signals into heartbeats. The quality of ECG signals in this study was very high as the signals were recorded from healthy subjects during activities with mild motion artifacts. Therefore, more sophisticated processing other than simple peak thresholding was not required for ECG signals. Also, note that the ECG signals were used only for the BCG segmentation in the ECG-based model, where BCG features were extracted using ECG as a reference.

To extract low-frequency features, the load cell outputs were low-pass filtered with the cut-off at 2Hz to extract respiratory components of the signal while filtering out the cardiac components and motion artifacts [10]. Raw spirometer recordings were low-pass filtered in the same way to process the airflow signals and obtain ground truth respiratory volume signals.

Subsequent to filtering, all signals were segmented into 16-second windows with a

time increment of 2 seconds. Ground truth values and features were computed from each window and fed into a machine learning regression model for training and testing. The window length was chosen based on the previous study [122] where RQI computed from a 16-second window achieved the optimal trade-off between the robustness of RQI and data coverage.

3.3.3.1 Ground Truth Processing

A pneumotachometer measures airflow, from which respiratory volume can be derived by integration in time. From the airflow measurement shown in Figure 3.3(b), the onsets of inspiration and expiration (represented with red and green markers in the plot) were detected by a simple zero-crossing detection. The positive interval under the signal between consecutive zero-crossing points indicates the inspiration cycle, whereas the negative interval under the signal indicates the expiration cycle. Integration over each inspiration and expiration cycle without cumulating bias over time results in the respiratory volume signals shown in Figure 3.3(b). In each window, the TV and RR values were calculated from all breaths within the window. The average of those values was used as the corresponding ground truth.

3.3.3.2 Derivation of the center of mass

To capture respiratory movements, the changes in the center of mass on a 2D plane formed by four load cells at each corner of the bed frame were derived. Figure 3.3(c) illustrates the location of the four load cells and the resulting 2D plane. Changes in the center of mass along X - and Y -axis of the bed were computed using four low-pass filtered load cell

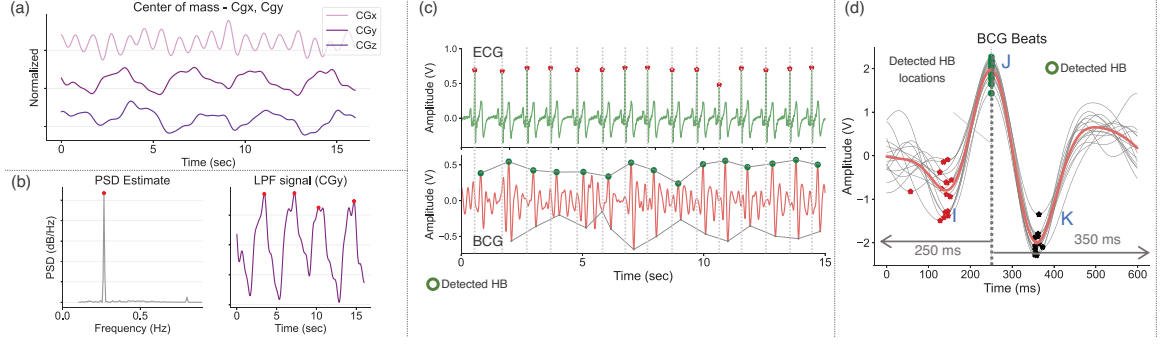


Figure 3.4: (a) An example plot of changes in the center of mass along the X , Y , and Z -axes of the bed. From the top, each trace represents CG_x , CG_y , and CG_z , respectively. (b) An example of the power spectral density (PSD) estimated from the CG_y of the low-frequency force signal and the detected breaths. (c) An illustration of ECG-based and ECG-independent BCG segmentation. In the ECG-based approach, the BCG signal was segmented into heartbeats using ECG R-peaks (grey vertical lines). In the ECG-independent approach, the candidate J-wave locations (green markers) were returned by the multi-channel HR estimation algorithm. (d) A plot of extracted heartbeats from one 16-second BCG window. Grey represents all the BCG heartbeats found in the window, and the red represents the averaged beat.

signals and denoted as CG_x and CG_y , respectively. The following equations express the derivation of CG_x and CG_y . In Equation 3.1-Equation 3.2, the datum was considered as the right foot (RF) load cell location and X_{len} and Y_{len} indicate the width and height of the 2D plane.

$$CG_x = \frac{X_{len} \times (LH + LF)}{W} \quad (3.1)$$

$$CG_y = \frac{Y_{len} \times (RH + LH)}{W} \quad (3.2)$$

$$CG_z = \int (W - LC_{sum}) dt \quad (3.3)$$

$$W = DC_{RH} + DC_{LH} + DC_{RF} + DC_{LF} \quad (3.4)$$

An example of the derived CG_x and CG_y is shown in Figure 3.4(a). Dynamics in CG_x

and CG_y reflect the forces resulting from respirations along the X - and Y -axis of the bed's 2D plane.

To quantify respiratory movements along the Z -axis of the bed, orthogonal to the 2D plane, the difference between the sum of low-pass filtered load cell signals (LC_{sum}) and its DC component (W) was derived. The measured difference, which quantifies the signal dynamics with respect to its DC component, was then integrated without aggregating bias over time, resulting in CG_z as expressed in Equation 3.3. Three low-frequency force signals — CG_x , CG_y , and CG_z — derived from the aforementioned processes capture the respiratory movement in all three dimensions, allowing for robust characterization of the 3D nature of respiratory motions in any posture.

3.3.4 Respiratory Rate and Low-Frequency Feature Extraction

3.3.4.1 Feature computation

Figure 3.4(b) illustrated the feature extraction steps for the low-frequency force signals. First, the power spectral density (PSD) of the 30-second segment was computed through Welch's method [123]. For Welch's method, Hamming window was used to obtain 8 segments with 50% overlap. From the computed PSD, the frequency with the largest PSD was output as the estimate of the respiration frequency. The locations of breaths in each window were then found through the amplitude thresholding using the estimated respiration frequency as a reference for minimum inter-peak distance. The beat-to-beat intervals and the beat amplitude values were then averaged together for each window.

The average beat-to-beat intervals were used as RR estimates in brpm and compared

against the ground truth RR from the spirometer. The RR estimates were also included in a feature set for the TV estimation algorithm. Each low-frequency force signal was processed with the aforementioned breath detection algorithm.

In addition to breath interval and amplitude features, a set of statistics including mean, std, min, max, 1st quartile, and 3rd quartile were computed to capture the dynamics in the low-frequency force signals.

3.3.4.2 Respiration Quality Index (RQI)

For the rejection of noisy windows with respiration waveforms corrupted by motion artifacts, the respiration quality index (RQI) introduced in the previous studies [124, 125, 122] was used. Each window from the low-frequency force signal was assessed by RQIs computed using the fast Fourier transform (FFT) and autocorrelation. FFT-based RQI (RQI_1) evaluates how much power is centered in the respiration frequency range in a given signal window. Autocorrelation-based RQI (RQI_2) evaluates the periodicity of the window in the respiration frequency range. The final RQI (RQI_3) was computed as the average of the two RQIs. Only the window with RQIs over a certain threshold ($RQI_1 > 0.55$ and $RQI_3 > 0.3$) was used for RR estimation and features for TV estimation. Note that among three low-frequency signals— CG_x , CG_y , and CG_z —the RQI of CG_y was used for rejection based on the analysis discussed in Section 3.4.1. The same threshold values were used across all subjects.

The threshold was determined heuristically and set at the level where increasing the threshold no longer significantly improves the overall accuracy of the algorithm but rejects more segments. Specifically, to determine the RQI threshold that achieves optimal trade-

off between the RR estimation accuracy and the coverage (i.e., the ratio of the number of windows remaining after rejection and the total number of windows), additional analysis was performed on a dataset outside the training and testing sets in this work. The additional dataset includes 4-channel load cell signals, an RR estimator, and the chest respiratory belt signal as the source of ground truth RR. From the additional analysis, the RQI threshold values used in this work achieved mean absolute error (MAE) of around 2.7 brpm at the worst case with the coverage over 70% on the external dataset, and therefore, were chosen for this work. More details about the external dataset and the RQI threshold analysis are presented in the Appendix section.

3.3.5 ECG-based BCG segmentation

To obtain BCG heartbeat features, BCG signals first need to be segmented into heartbeats. In this work, two different approaches were taken for the BCG signal segmentation. The first is the ECG-based approach, where BCG signals were segmented into heartbeats by extracting 600 ms-long segments from ECG R-peaks as shown in Figure 3.4(c). BCG heartbeat length was chosen as 600 ms based on the previous study [87]. In the ECG-based approach, BCG J-waves were identified as the maximum peak within the $[200 - 400ms]$ range from ECG R-peaks. The closest minimum valleys before/after the J-waves were chosen as the I-wave and J-wave in each heartbeat. To reject noisy beats in which I-, J-, and K-waves are not identifiable, the detected I-, J-, and K-wave locations within the beat were compared to I-, J-, and K-wave locations in BCG templates. Here, BCG templates were generated from the first 30 seconds of recording during the baseline period when subjects were staying still and not performing any respiratory tasks. Therefore, the highest

signal quality was observed during this period in general and chosen for generating the templates. The detected I-, J-, and K-wave locations that deviate significantly from those in BCG templates were rejected.

3.3.6 ECG-independent BCG segmentation

Although ECG signals were recorded in this study for validation purposes, the ECG may not be available in real-world applications. For ECG measurement, an auxiliary sensing system is required. However, in the general wards where patients are less intensively monitored, such systems may not be deployed. To validate the estimation of TV using the sensors embedded on a hospital alone (i.e., four load cells), the BCG J-wave locations were estimated without ECG. In the ECG-independent approach, BCG heartbeat-based features were extracted as follows:

3.3.6.1 Estimation of J-wave location using HR estimation algorithm

To estimate the J-wave locations, the multi-channel HR estimation algorithm described in the previous studies [66, 8] was deployed. The multi-channel HR estimation algorithm estimates the inter-beat-interval (IBI) based on the estimation of the probability density function (PDF). Here, the PDF outputs the probability of each candidate IBI in the predefined range being the actual IBI of the given signal segment. The algorithm in [66] also demonstrated based on [8] that by using a short signal segment with a short time shift between consecutive windows, the algorithm can also provide the estimates for J-wave locations.

The J-wave location estimation in [8] was based on the assumption that the PDF estimates the interval between the heartbeat pair around the window center. Therefore, the

J-peak of the second beat in the pair (called the anchor point) would exist no further than the estimated IBI from the window center. Also, with the short time shift between windows, the same heartbeat pair and the anchor point would appear multiple times across a few consecutive windows. The anchor points that appeared in three or more windows were considered as the J-peak candidates. The detailed procedure for anchor point detection is presented in [8, 66]. Using the candidate J-wave locations from the multi-channel HR estimation algorithm, the BCG signal was segmented into heartbeats, as shown in Figure 3.4(c). In Figure 3.4(c) bottom, the green marker indicates an example of the candidate J-wave locations found by the algorithm, and Figure 3.4(d) shows the BCG heartbeats segmented accordingly. The segment 250 ms before and 350 ms after the detected J-wave locations were extracted as the heartbeats.

3.3.6.2 Rejection of false positive beats

The candidate heartbeats extracted from the previous subsection were downsampled to 100Hz, resulting in 60 samples for each heartbeat. The downsampled candidate beats were then labeled as true ('1') or false positive ('0') according to ECG R-peak. If the estimated J-wave location matches the J-wave location estimated by the ECG, then the beat was labeled as '1' and '0' otherwise. Using the downsampled candidate heartbeats themselves as features and their labels as the target, the support vector machine (SVM) classifier was trained for binary classification of true versus false-positive heartbeats. The 'rbf' kernel with $C=10$ and $gamma=10$ were used for the SVM model.

Table 3.2: Features extracted from load cell signals

Feature Type	Feature Name	Description
BCG beat	IJint	IJ time interval
	IKint	IK time interval
	JKint	JK time interval
	IJamp	IJ amplitude
	IJK _{RMS}	RMS value of IJK complex
	JampHR	J-wave amplitude X HR
	IJKrms/IBI	RMS of IJK complex /IBI
	IJ/IBI	IJ time interval/IBI
	IK/IBI	IK time interval/IBI
	JK/IBI	JK time interval/IBI
	IBI	inter-beat-interval (IBI)
	Band power	Band power computed in [0-9Hz] range with the bin size of 3Hz
	PSD features	Maximum PSD and corresponding frequency
LF	CG _{xRR} , CG _{yRR} , CG _{zRR}	RR estimate from CGx, CGy, CGz
	CG _{xAmp} , CG _{yAmp} , CG _{zAmp}	Average breath beat amplitude from CGx, CGy, CGz
	CG Stats	Statistics of CGx, CGy, CGz
Demographic	Weight	

Type, name, and description of features extracted from the load cell signals in this work.

3.3.6.3 I- and K-wave detection after correction

After rejecting some false positive heartbeats, the I- and K-wave locations were found within 60 ms before/after the estimated J-wave location in each heartbeat. The heartbeats were rejected when I- or K-wave did not exist in that range.

3.3.7 BCG heartbeat features

After segmenting the BCG signals into heartbeats using either the ECG-based or ECG-independent approach and finding the I-, J-, and K-waves within BCG heartbeats, BCG heartbeat features were computed. The BCG heartbeat features include both time and frequency domain features. For each window, those features were computed from the averaged beat — the beat averaged across all beats detected in the window.

Amplitude and timing parameters were derived from the amplitude/timings of I-, J-, and K-waves of BCG heartbeats resulting in 11 features. Other time domain features include the area under the IJK complex. Frequency domain features include band power computed in the [0 - 9Hz] range with a bin size of 3Hz. In total, 16 features were extracted from the BCG signals. Note that four BCG channels were averaged for the extraction of BCG heartbeat features. Also, all IBI-related features were computed using the IBI estimated from the multi-channel HR estimation algorithm, not from the ECG in the ECG-independent approach. All extracted features are listed in Table 3.2.

3.3.8 Machine Learning Model Training

3.3.8.1 Regression Model

For the estimation of TV from the features extracted in the previous steps, an Extreme Gradient Boosting (XGBoost)[126] model was used. The XGBoost regression model was chosen based on the preliminary analysis that the XGBoost model outperformed other regression models. XGboost is a tree-based ensemble method with gradient boosting, where trees are sequentially trained and added such that the loss made by existing models could be

minimized. The final predictions are made by adding all trees in the “ensemble” together.

XGboost has been widely deployed in recent studies due to its performance and robustness against over-fitting. Also, interpretability is another advantage of XGboost and other tree-based models. XGBoost quantifies the importance of each feature by measuring reduction in loss within each tree at the node associated with the corresponding feature and averaged over all trees in the “ensemble”. For healthcare applications in particular, the feature importance returned by the model allows for physiological interpretation of the results.

In this work, the XGBoost model was trained on the features extracted for all windows to estimate the corresponding target TV values. Hyperparameters of XGBoost such as maximum depth, number of estimators, and gamma were determined through hyperparameter tuning done in an inner LOSO cross-validation (CV) nested inside outer LOSO CV loop for the train-test split. The following model training schemes were evaluated to analyze the postural effects on the TV estimation accuracy:

- 1) Posture-specific model training- a separate model trained per posture
- 2) Posture-independent model training- one globalized model trained on data from all four postures.

Note that subject-specific training was not performed in either case.

3.3.8.2 Evaluation

For evaluation, the LOSO CV framework was deployed. In each LOSO CV loop, the model is trained on N-1 subjects (N = total number of subjects) and tested on one held-out

subject. This framework generates a globalized model without any subject-specific training and tests how well the model generalizes to the unseen data from a new subject. For the assessment, the root mean squared error (RMSE) was computed for each fold (i.e., each held-out subject in LOSO CV), along with the overall correlation (r) between the estimated and actual TV values across all folds.

3.3.8.3 Feature combinations

Multiple models were trained with different combinations of features to assess the contribution of each feature type on TV estimation performance. For each model, the training and validation procedure presented above were repeated. Resulting correlation and RMSE values were compared across all feature combinations listed in Table 3.3.

3.4 Results and Discussion

3.4.1 RR Estimation

The Bland-Altman plot in Figure 3.5(e) show the agreement between the RR estimated from CG_y of the low-frequency force signals and the actual RR. Among the total of 13172 windows across all subjects, tasks, and postures, 8.48% of windows were rejected through RQI thresholding, resulted in 12055 windows. In Figure 3.5 (e), different colors and shapes represent each subject and posture. The estimated RR was highly correlated to the true RR ($r = 0.99$), and 95% of the differences between the two were observed in the range of $[-1.3, 1.26]$ brpm (width of 95% LoA: 2.56 brpm).

The average subject-wise RMSE across all postures and respiratory tasks was 0.60 brpm

Table 3.3: TV Estimation Errors for Different Feature Combinations

Feature Combination	Supine			Left			Right			Seated			All		
	r	RMSE (L)	r	RMSE (L)	r	RMSE (L)	r	RMSE (L)	r	RMSE (L)	r	RMSE (L)	r	RMSE (L)	r
LF (CGx)	0.74	0.32	0.82	0.24	0.71	0.29	0.79	0.25	0.71	0.25	0.79	0.25	0.71	0.32	0.71
LF (CGy)	0.65	0.34	0.74	0.27	0.79	0.25	0.87	0.19	0.78	0.19	0.87	0.19	0.78	0.27	0.78
LF (CGz)	0.87	0.21	0.76	0.28	0.79	0.25	0.74	0.27	0.79	0.27	0.74	0.27	0.79	0.27	0.79
LF (CGx, CGy)	0.77	0.29	0.85	0.22	0.78	0.25	0.87	0.19	0.80	0.19	0.87	0.19	0.80	0.26	0.80
LF (CGy, CGz)	0.87	0.22	0.79	0.24	0.82	0.23	0.88	0.19	0.83	0.19	0.88	0.19	0.83	0.24	0.83
LF (CGx, CGz)	0.88	0.21	0.80	0.25	0.80	0.24	0.84	0.22	0.82	0.22	0.84	0.22	0.82	0.25	0.82
LF (CGx, CGy, CGz)	0.87	0.21	0.84	0.22	0.83	0.22	0.89	0.18	0.83	0.18	0.89	0.18	0.83	0.24	0.83
BCG beat (ECG-independent)	0.35	0.49	0.09	0.47	0.23	0.48	0.26	0.41							
BCG beat (ECG-based)	0.36	0.50	0.02	0.54	0.20	0.48	0.23	0.46	0.27	0.46	0.23	0.46	0.27	0.46	0.27
BCG beat + LF (CGx, CGy, CGz) + Weight (ECG-independent)	0.88	0.21	0.82	0.23	0.85	0.21	0.89	0.19	0.85	0.19	0.89	0.19	0.85	0.23	0.85
BCG beat + LF (CGx, CGy, CGz) + Weight (ECG-based)	0.87	0.22	0.83	0.23	0.84	0.22	0.87	0.20	0.84	0.20	0.87	0.20	0.84	0.24	0.84
Respiratory Tasks															
Baseline			SF			SR			DF			DS			
MAE	$E_{rel}(\%)$	MAE	$E_{rel}(\%)$	MAE	$E_{rel}(\%)$	MAE	$E_{rel}(\%)$	MAE	$E_{rel}(\%)$	MAE	$E_{rel}(\%)$	MAE	$E_{rel}(\%)$	MAE	$E_{rel}(\%)$
0.13	20.29	0.09	20.54	0.10	28.30	0.26	21.59	0.30	21.15						

(Top) TV estimation errors for multiple models trained on different combinations of features. The reported values are the correlation (r) and RMSE (L) between the predicted and actual TV. RMSE values were averaged over subjects. (Bottom) TV estimation error by postures, averaged across subjects and postures. MAE: mean absolute error (L), E_{rel} : relative (percent) error.

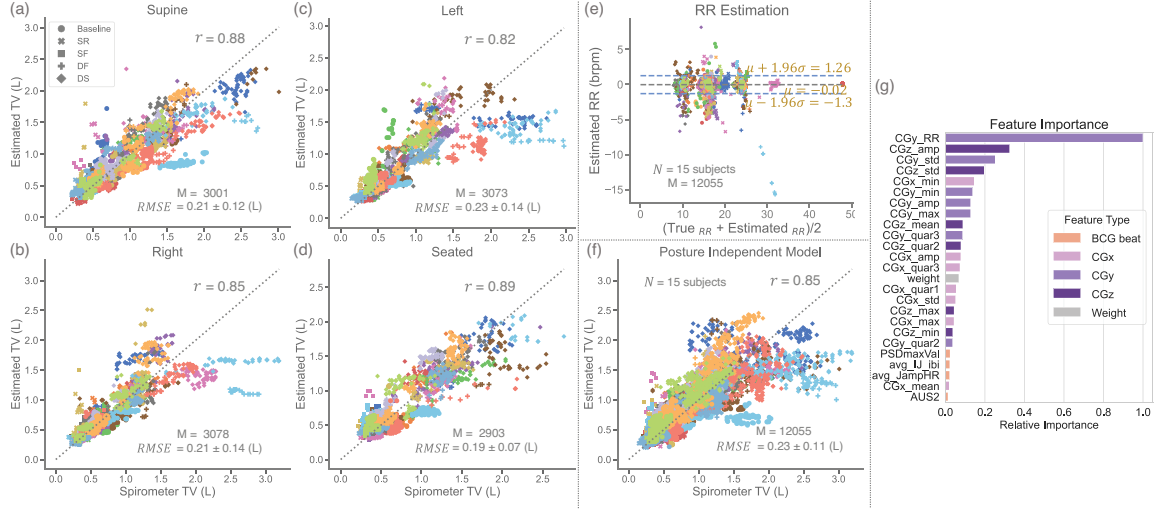


Figure 3.5: (a)-(d) Correlation between the estimated and actual TV. The results are shown by posture - (a): Supine, (b): Right lateral, (c): Left lateral, (d): Seated. M =Number of datapoints in the plot, N =Number of subjects (e) A Bland-Altman plot for RR estimation error, including all postures, tasks, and subjects. Dotted lines indicate 95% LoA. (f) A correlation plot for the posture-independent model trained on the entire dataset, including all postures. Shape-tasks, Color-subject. (g) A plot for relative feature importance averaged over the four posture-specific models. Same feature types are represented with the same color with different intensity

(± 0.27 brpm). By respiratory task, the average RMSE values in brpm were 0.54 (baseline), 0.60 (shallow regular), 0.40 (shallow fast), 1.24 (deep fast), and 0.61 (deep slow). The RR estimation accuracy was similar across all postures — the average RMSE values were 0.89, 0.50, 0.54, 0.61 brpm for supine, left/right lateral, and seated posture, respectively.

In this work, RR was predicted using CG_y of the low-frequency force signals rather than using CG_x or CG_z or selecting the one with the highest signal quality among the three for each window. CG_y was chosen based on the assessment of each component of low-frequency force signals using mean RQI, the average of FFT-based and autocorrelation-based scores. The RQI score averaged over four postures was 0.53, 0.68, and 0.56 for CG_x , CG_y , and CG_z , respectively, indicating CG_y had the highest RQI overall. Also, the respiration waveform was apparent in CG_y regardless of the posture, resulted in consis-

tently high RQI across postures — 0.68, 0.69, 0.68, and 0.66, respectively. For CG_x , the RQI was relatively high in lateral postures (0.61 and 0.58) but low in supine and seated posture (0.47 in both postures). On the other hand, the opposite was observed with CG_z — the RQI was high in supine and seated posture (0.58 and 0.57) and low in lateral postures (0.52 and 0.54). Based on the RQI assessment, CG_y , which had good and consistent signal quality in any posture compared to the other two low-frequency force signals, was selected for the RR estimation and resulted in robust estimations.

In the previous studies [124, 122], the RQI was used to assess the quality of ECG or photoplethysmography (PPG)-derived respiration waveforms. It has shown that the RQI could quantify the quality of respiration waveforms, thus resulting in improved RR estimation when fusing multiple respiration waveforms derived from different sources by selecting the one with the highest RQI. Similarly, the RR estimation accuracy was improved in this work by rejecting noisy respiration waveforms with the RQI. Width of 95% LoA was decreased from 3.22 to 2.56 brpm in the Bland-Altman analysis with the removal of some segments with RQI under the threshold. This suggests the robustness of RQI in improving RR estimation by detecting and rejecting unreliable signal segments corrupted by the artifacts. Rejecting such windows is also important for TV estimation because the low-frequency force signals are the top contributing features in the model, as will be presented in the following section.

3.4.2 TV Estimation

Table 3.3 (top) shows the Pearson correlation (r) and RMSE between the predicted and actual TV for the posture-specific models trained on different combinations of features ex-

tracted from the load cell signals. These results were obtained from the ECG-independent model unless specified as ECG-based, and the reported RMSE values are the LOSO cross-validation accuracies averaged over subjects.

For the ECG-independent model, the model trained with the combination of all features—BCG heartbeat, three axes of low-frequency force, and the body weight features—resulted in the best performance, with a correlation of $r = 0.89$ and RMSE of 0.19 (L) in the best case (from seated posture). The lowest correlation ($r = 0.82$) was achieved in lateral postures, leading to a correlation over 0.82 in all cases with no significant difference in estimation accuracy between postures. The corresponding ECG-based model, where the low-frequency features are extracted in the same way, but the BCG heartbeat features were extracted using ECG R-peaks as a reference to identify heartbeats, demonstrated performance similar to the ECG-independent model. The best and worst case for the ECG-based model were supine ($r = 0.87$) and left lateral ($r = 0.83$). The results in Figure 3.5 and Table 3.4 were all reported with the ECG-independent model trained on all features including the BCG heartbeat, low-frequency, body weight features as listed in Table 3.2.

Figure 3.5(a)-(d) visualizes the results with different marker colors and shapes indicating subjects and tasks, respectively. The plots show the windows remaining after RQI rejection performed in the RR estimation stage, providing 12055 windows among a total of 13172 windows. By posture, 7.94%, 7.10%, 7.09%, and 11.79% of windows were rejected for supine, left lateral, right lateral, and seated postures, respectively.

For evaluating inter-subject variability, the subject-wise RMSE values were presented for each posture in Table 3.4. Overall, the relative error was around 20% across postures, but there are some subjects with high errors — for example, subject 10, colored as light

blue in Figure 3.5. Subject 10 had relatively larger ground truth TV values compared to other subjects as shown in Table 3.4, possibly due to unnatural breathing through a spirometer. During the protocol, subjects were instructed to intentionally make their respiration shallower or deeper than their normal resting breathing but only to the extent that would not hinder their natural breathing behavior. However, some subjects put excessive effort into making deeper breaths, resulted in unnatural breathing behavior that likely becomes a source of the noise. Table 3.3 (bottom) also presents the error (MAE, E_{rel} : relative percent error) by respiratory tasks averaged over all subjects. Although the MAE was generally higher for the deep breathing tasks (i.e., higher TV) and similar trend was observed from Figure 3.5(a)-(d), E_{rel} was consistent across respiratory tasks, except SR. The high relative error in shallow breathing could be attributable to more chaotic waveform in both the load cells and the reference spirometer when simulating shallow breathing.

Figure 3.5(f) provides the TV estimation results from the posture independent models (without ECG signals) trained on the entire data set, including all postures, tasks, and subjects. The posture independent model resulted in the correlation $r = 0.84$, similar to lateral postures in posture-wise models.

3.4.3 Evaluation of Features

Figure 3.5(g) shows the relative feature importance returned by the ECG-independent XGBoost regression model. The most important feature was scaled to 1 and each feature type was represented with different colors for visualization, with similar feature types (e.g., low-frequency features) colored the same with different intensity. The relative importance values for the top twenty-five features shown in Figure 3.5(g) were averaged across four

Table 3.4: Subject-wise TV Estimation Error (ECG-independent Model)

Subject	Supine			Left			Right			Seated			Posture independent		
	RMSE	$E_{rel}(\%)$	True TV	RMSE	$E_{rel}(\%)$	True TV	RMSE	$E_{rel}(\%)$	True TV	RMSE	$E_{rel}(\%)$	True TV	RMSE	$E_{rel}(\%)$	True TV
1	0.33	33.01	1.15	0.44	28.08	0.99	0.29	32.76	0.59	0.15	15.37	0.84	0.34	24.88	0.89
2	0.09	8.13	0.82	0.19	21.89	0.66	0.13	14.32	0.68	0.15	16.73	0.71	0.15	15.78	0.72
3	0.10	10.92	0.68	0.26	24.03	0.69	0.12	12.12	0.67	0.19	15.06	0.82	0.15	13.99	0.72
4	0.16	23.38	0.60	0.08	14.21	0.52	0.09	13.62	0.57	0.15	20.36	0.53	0.14	17.43	0.55
5	0.15	15.42	0.87	0.07	7.97	0.80	0.20	17.63	0.80	0.12	11.73	0.81	0.13	13.40	0.82
6	0.20	13.49	1.06	0.24	25.26	0.88	0.20	26.87	0.69	0.32	22.21	0.88	0.31	22.98	0.87
7	0.25	23.90	0.80	0.22	16.37	0.79	0.34	16.67	0.91	0.15	17.29	0.73	0.24	21.35	0.81
8	0.19	16.16	0.82	0.15	15.42	0.64	0.15	15.04	0.70	0.12	13.73	0.70	0.17	17.36	0.72
9	0.22	25.51	0.91	0.15	25.11	0.65	0.30	41.71	0.72	0.13	21.03	0.75	0.16	24.88	0.75
10	0.55	26.92	1.30	0.61	35.66	1.12	0.66	29.45	1.25	0.34	47.20	0.90	0.59	34.60	1.16
11	0.14	13.81	0.86	0.17	18.76	0.67	0.10	12.94	0.61	0.25	32.44	0.66	0.21	23.66	0.69
12	0.34	22.07	1.18	0.39	22.55	0.97	0.20	14.86	0.91	0.29	30.19	0.75	0.27	18.80	0.97
13	0.15	27.99	0.64	0.09	16.00	0.60	0.10	11.66	0.63	0.10	15.56	0.72	0.14	18.58	0.65
14	0.20	18.56	1.02	0.18	13.28	0.83	0.22	14.30	0.82	0.13	11.22	0.80	0.28	22.57	0.87
15	0.11	15.29	0.73	0.23	34.02	0.62	0.12	17.90	0.59	0.22	36.74	0.52	0.19	25.10	0.62
Mean	0.21	19.64	0.90	0.23	21.24	0.76	0.21	19.46	0.74	0.19	21.79	0.74	0.23	21.02	0.79
STD	0.12	6.85	0.20	0.14	7.48	0.16	0.14	8.66	0.17	0.07	10.02	0.11	0.11	5.27	0.15

Subject-wise error for TV estimation. The reported values are RMSE (L) and percent error (%) between the predicted and actual TV for each subject and posture. True TV values were also reported in L.

posture-specific models. Among the top twenty-five important features, the most important features were low-frequency features, including all three axes of the low-frequency force signals.

As shown in the feature importance plot, low-frequency features are the main contributing features in TV estimation models. According to the comparison of models trained on different feature combinations in Table 3.3, having a combination of multiple axes of the low-frequency force signals outperformed the single-axis models. This could be because of the kinematics of the chest wall movement caused by the respirations.

The chest wall is comprised of two compartments, the rib cage and abdomen [127]. The displacements of the rib cage occur in three-dimensions (3D), including the dorso-ventral (DV), lateral (LA), and head-to-foot (HF) directions of the human body. On the other hand, the movement of the abdomen is confined to the dorsoventral direction [127]. In the previous studies [127, 128], an increase in abdomen displacement in the DV direction was observed in supine posture compared to seated posture. Therefore, it could be assumed that in this study, where subjects were lying on the bed, the respiratory force would be largest in the DV direction with smaller movement in HF and LA directions caused by the displacement of rib cage. This suggests that the respiration waveform would be prominent along the bed's axis, aligning with the DV direction.

The axes of the human body align differently to the bed's 3D axes depending on the posture. With the configuration in Figure 3.3(c), DV, HF, and LA directions are mapped to the Z, Y, and X-axes of the bed in supine. In the lateral postures, the DV direction aligns better with the bed's X axis, the HF with the Y and the LA with the Z axis. However, in the seated posture, alignment to the bed axes changes depending on the head angle. Because

the respiratory forces are most aligned with the DV body axis, it could be hypothesized that the respiratory forces would be most prominent in the bed's Z-axis in supine, X-axis in lateral postures, and Y-axis in the seated posture.

The results in Table 3.3 support this hypothesis. In the supine posture, among single-axis models engaging either CGx , CGy , or CGz , the CGz model outperformed the other two. In the left lateral posture, the CGx model—DV direction in this posture—had a higher correlation than the other two axes. However, unlike the left lateral posture, the correlation was higher in CGy and CGz models than in CGx . This could be due to how the CGx was derived in this work. In Equation 3.1, we assumed the datum as RF load cell and used LH and LF load cells for the center of mass computation. Therefore, CGx is less sensitive to the X-axis force pointing towards the right side of the bed. In the seated posture, the CGy model resulted in the highest correlation among the three axes.

Engaging features from all three axes could allow complete characterization of the 3D nature of the respiratory movement. Therefore, it is notable that the models with all three axes lead to the best performance in most cases in Table 3.3. Also, having all axes is essential to capturing the DV movement in any posture, particularly for the posture-independent model.

In this work, the importance of BCG heartbeat-based features was low compared to low-frequency features. Therefore no significant difference between the ECG-based and ECG-independent model was observed, and the feature computation error that could be caused by the BCG heartbeat identification seemed to have minimal effects. Still, adding the BCG heartbeat features improved the performance in supine, right lateral, and posture-independent models for ECG-independent cases. This could be because including BCG

heartbeat features allows the model to capture respiratory effects reflected in the cardiac signals. It is known from the literature [125, 124, 129] that cardiac signals such as ECG, PPG, and BCG are modulated by respiration. BCG beat-based features could add such respiratory information with acceptable quality signals, allowing for improved TV estimation.

3.4.4 Comparison with State-of-the-art Methods

The proposed RR and TV estimation algorithm were validated against the data recorded in multiple postures with large RR and TV variations in this study. Our RR estimation algorithm achieved high accuracy (RMSE=0.6 brpm, width of 95% LoA=2.56 brpm) comparable or even better than state-of-the-art studies for non-invasive continuous RR monitoring summarized in Table 3.1 and Section 3.2.

For TV estimation, the RMSE was around 0.2 L (with $r > 0.82$) across all scenarios for our model. These error values might be higher than the tolerance for medical-grade devices requiring $\pm 3\%$ errors [46]. However, this accuracy is acceptable considering that the approach requires neither obtrusive sensors nor tight skin contact with sensors that would interfere with daily activities. Although each study was tested on different dataset and the evaluation metrics were different, the performance in this study is still comparable to many other studies in Table 3.1 — with IP [114, 130, 131], typically higher correlation ($r > 0.9$) is observed, but it requires the attachment of multiple electrodes. The correlation coefficients (r) of other state-of-the-art technologies [132, 51, 113, 59, 52, 133] range from 0.77 to 0.98, but none of these technologies investigated globalized approaches that do not require subject-specific calibration.

Calibration is the main challenge in many of these technologies. Frequent calibration

could achieve higher accuracy in general but is not desirable in terms of translation to real-world settings, especially in hospitals where clinicians are already overloaded. To this end, this work has demonstrated improved usability by proposing a globalized model without any training specific to the subject or a particular posture, promoting the application of the approach in actual hospital setups with limited resources. With the usability and reasonably high model performance, the proposed approach in this work could provide a quantitative assessment for respiratory health at a low cost by deploying existing sensors already embedded in a hospital bed.

3.4.5 Limitations and Future Work

A relatively small and homogeneous population for testing is one limitation of this study. In the current setup, although the protocol was designed to simulate abnormal respiratory conditions commonly seen from patients with respiratory conditions, we could only validate our model with healthy and young subjects. Based on the validation in this work, future studies should include a diverse population, including patients with respiratory diseases such as COPD and asthma suffering from obstructive breathing to evaluate/improve the performance of the model and determine a realistic accuracy threshold for alarming patient deterioration. Also, the approach needs to be validated for the longer term in actual hospital settings. For the actual application, further studies should be conducted under uncontrolled settings to engage natural breathing behaviors and take into account the increased noise caused by motion artifacts arising from daily activities.

Another limitation is the validation of the effects of specific features. Although the results in this work suggest improved model accuracy by including BCG heartbeat-based

features, the improvement was minimal. This could be due to feature extraction errors from the processing pipeline for both the ECG-based and ECG-independent cases or a decrease in signal quality caused by the respiratory motions. Future work should further investigate the role of BCG features in improving the performance and robustness of the signal processing pipeline in this work.

3.5 Appendix

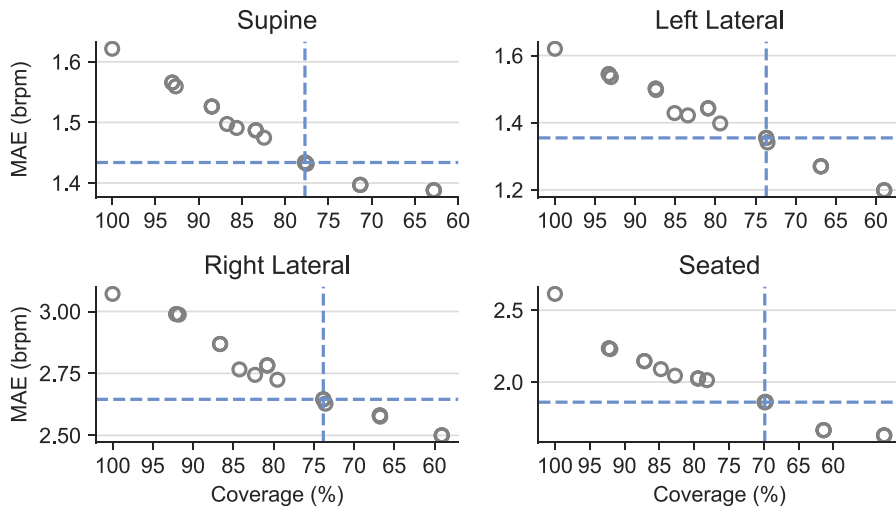


Figure 3.6: A plot of Mean absolute error (MAE) over coverage (%) for RR estimation from load cell signals evaluated against ground truth RR from a respiratory chest belt. Each data point indicates a different RQI threshold level.

An additional analysis was performed on a dataset outside this work collected from 20 healthy subjects (IRB protocol: H18452, Male:9, Female:11; Age: 24.30 ± 3.33 ; Weight: 67.29 ± 14.35 kg; Height: 171.20 ± 10.34 cm), which resulted in 9836 data points. The setup was the same as described in Section 3.3.1 with subjects staying on the bed in four different postures but without respiratory tasks. Using the 4-channel load cell signals as an RR estimator, and the chest respiratory belt signal as the source of ground truth RR,

the RQI, RR estimation error, and the coverage were computed. The plot in Figure 3.6 presents MAE for RR estimation over the coverage. Each data point indicates a different RQI threshold level, and the blue dotted line is the RQI threshold chosen in this work.

3.6 Conclusion

This study demonstrates the feasibility of using load cell sensors embedded in a hospital bed for continuous and unobtrusive monitoring of respiratory parameters such as RR and TV. The proposed method could be widely deployed in general hospital wards without adding a cost for purchasing auxiliary sensing systems and burdening healthcare providers with applying additional hardware to the patients. Additionally, it provides benefits from the patients' perspective in that the technology does not require attention to perform forced breathing for calibration, which is necessary for many other non-invasive respiratory monitoring systems. Therefore, the proposed method is feasible for long-term measurements allowing for longitudinal tracking of disease progression or recovery from respiratory infections. It could also be applied to assessing pulmonary function in patients who are unconscious or experiencing cognitive failure, which is not possible with conventional approaches. In conclusion, the multi-channel load cell system on a hospital bed with a machine learning algorithm could provide a robust long-term continuous respiratory monitoring method. The ease of application without calibration and the high accuracy demonstrated in this work suggest the potential of monitoring RR and TV using the load cells alone in general care facilities.

Relevant Publication

H. Jung *et al.*, “Estimation of Tidal Volume Using Load Cells on a Hospital Bed,” *IEEE Journal of Biomedical and Health Informatics*, 2022, ISSN: 21682208. DOI: 10.1109/JBHI.2022.3141209

H. Jung *et al.*, “Impedance Pneumography: Assessment of Dual-Frequency Calibration Approaches,” in *2021 IEEE 17th International Conference on Wearable and Implantable Body Sensor Networks, BSN 2021*, 2021. DOI: 10.1109/BSN51625.2021.9507042

CHAPTER 4

ESTIMATION OF BLOOD PRESSURE

The previous two chapters discussed the estimation of some basic vitals such as HR and RR and explored the feasibility of monitoring TV, a relatively new parameter. In addition to those parameters, BP is one of the important vitals to assess the physiologic state; however, its measurement often relies on bulky and uncomfortable devices such as an oscillometric cuff. Therefore, frequent and convenient measurement of BP using non-invasive biosignals has been studied for a long time, but continuous cuff-less BP measurement remains challenging.

This chapter explores the estimation of BP from the BCG signal to enable a complete hospital bed monitoring system that provides a full set of vitals. This study presents algorithms for continuous BP monitoring using the load cell BCG and the finger/toe PPG signals. In this work, we propose two different approaches – (1) a conventional PTT-based model and (2) a U-Net-based model to predict BP from BCG and PPG signals. In PTT-based models, the PTT was acquired through signal processing and linear regression was performed on its inverse to estimate BP. In the U-Net-based model, the source signals (BCG and PPG) were translated to BP waveforms from which the BP values were estimated after calibration. In sum, this study demonstrates the feasibility of continuous BP monitoring using sensors in a hospital bed and elucidates the effects of different sensing modalities and postural variability.

4.1 Introduction

One conventional approach to non-invasive continuous BP monitoring is through PTT or PAT. The PTT is defined as the time elapsed for the pulse wave to propagate along the length of the arterial tree [135] and is known to be inversely correlated to the BP. To acquire non-invasive PTT, two timing references, one proximal and the other distal to the heart are required. In practice, a combination of signals such as the ECG, PPG measured from an extremity location such as a fingertip or toe, and cardiogenic vibration signals such as the BCG or SCG could be used as the timing references. In particular, the PTT is often acquired as the timing delay between the fiducial points in BCG or SCG and the PPG. In previous studies, the PTT was found to be highly correlated to the BP in both the controlled lab environment and at-home settings [136, 137]. Similarly, the PAT is defined as the timing delay between the ECG R-peak and the foot of the PPG. Along with PTT, the PAT has been widely used to monitor BP due to its convenience in measurement. However, the PAT has been demonstrated to be less correlated to BP compared to PTT as it includes the PEP which is determined by ventricular properties and autonomic state rather than just BP [135, 20].

Besides using PTT or PAT to estimate BP, some studies estimated BP using multiple timing-related or morphological features from the BCG and PPG signals as inputs to the machine learning (ML) model. In [74, 75, 76, 77], PTT or PAT features extracted from various locations, the PPG morphological features and some physiological features including HR were used to estimate BP through ML models such as multiple linear regression (MLR), support vector regression (SVR) and tree-based models. Some studies also demon-

strated BP estimation using BCG signals alone. In [73], features from multi-channel BCG recordings were used to relatively track BP values and the study in [138] a bidirectional long short-term memory network (bi-LSTM) to estimate SBP and DBP from a two-channel BCG system. Also, some studies used convolutional neural network (CNN), LSTM, or a combination of two to predict SBP and DBP from the ECG and PPG [74, 139].

Recently, end-to-end approaches for estimating the BP through translation of PPG signals to BP waveforms have been widely studied. For example, in [78, 79, 80, 81], variants of the original U-Net model in [97] were proposed. With the recent success of generative adversarial network (GAN) models in generating realistic images or speech signals [140, 141, 142], GAN models have also been applied to 1D biosignals as well. For example, the studies in [143, 144] demonstrated the use of cycle GAN models to generate model realistic BP waveforms from the PPG signals alone. Table 4.1 summarizes the aforementioned state-of-the-art studies for non-invasive continuous blood pressure estimation, presenting the method, sensing modalities, the dataset used, and their performance.

In this work, we demonstrate BP estimation using the PPG and the load-cell BCG signals in two different approaches: the conventional PTT-based and the DL-based models. The proposed algorithms were evaluated on a dataset collected from 20 healthy subjects with recordings consisting of the ECG, finger PPG, toe PPG, 4-channel load cell BCG and the continuous BP from the finger BP cuff measured in four different postures on the hospital bed. The performance of the model was evaluated from several angles. First, we demonstrated the effects of different source signals—finger PPG and toe PPG in the PTT analysis, and comparison between multi-modal and single-modal models in DL methods. Also, we evaluated performance under different calibration schemes to understand the ef-

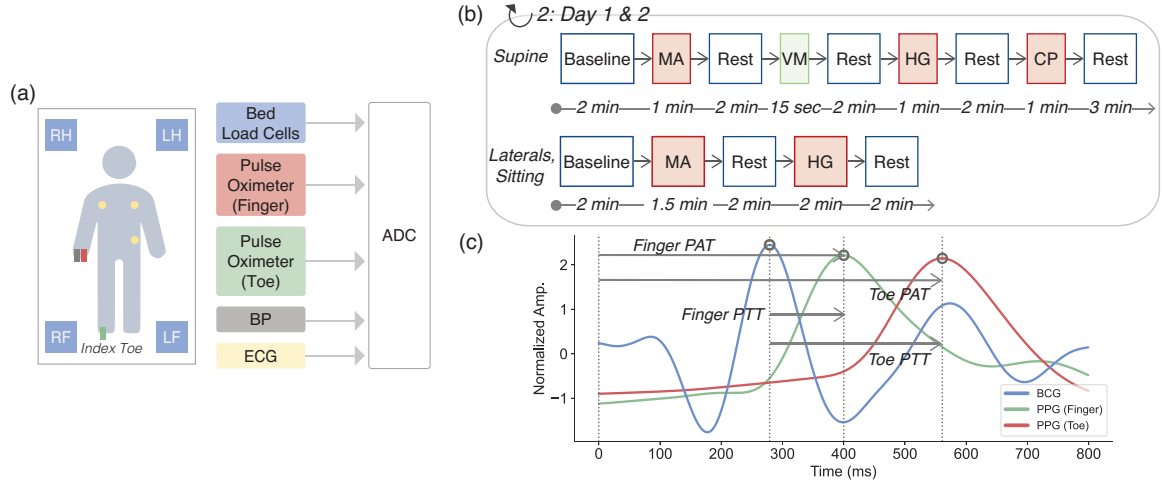


Figure 4.1: The overview of the test setup and the protocol for human subjects study engaging tasks to modulate BP. (a) 4-channel BCG, Finger/Toe PPG, BP, and ECG signals were recorded during the protocol. Pulse oximeter sensors were placed on right index toe and finger. Finger BP cuff was placed on the same hand as PPG. (b) Mental arithmetic (MA), Valsalva maneuver (VM), hand grip (HG), and cold pressor (CP) were performed in four different postures including supine, left/right lateral, and the seated posture in this study. (c) An example plot of PPG (Finger/Toe) and BCG were shown for one heartbeat cycle. PAT: Pulse Arrival Time, PTT: Pulse Transit Time, PPG: Photoplethysmogram, BCG: Ballistocardiogram, ADC: Analog to Digital Converter

fects of postural variability. Finally, the performances between the two different approaches were compared to explore the advantages and limitations of each method.

4.2 Methods

4.2.1 Experimental Protocol

In this study, twenty healthy subjects (Male: 11, Female: 9, Age: 24.3 ± 3.3 ; Weight: 67.29 ± 14.4 kg; Height: 171.2 ± 10.3 cm) who have not been diagnosed with cardiovascular or respiratory diseases were recruited for the human subjects study. The protocol (H18452) was approved by Georgia Institute of Technology Institutional Review Board (IRB).

Figure 4.1 describes the test setup and protocol used for this study. Each subject laid down on the patient bed (Centrella®, Hill-Rom) in four different postures with the ECG,

Table 4.1: State-of-the-art Studies for Blood Pressure Estimation

Paper	Dataset (Number of Subjects)	Methods (Sensing Modality)	Calibration	SBP (mmHg)		DBP (mmHg)		MAP (mmHg)	
				MAE	RMSE	r	MAE	RMSE	r
[145]	In-house (13 subjects)	PTT (SCG, PPG)	Subject-specific	-	2.9	0.84	-	4.8	-
[136]	In-house (44 subjects)	PTT (SCG, PPG)	Subject-specific	2.90	3.41	0.67	5.36	6.28	0.50
[76]	MIMIC I (28 records)	ML (PPG) ML (ECG, 2 Pulse pres- sure wave sensors)	Globalized model	4.65	-	0.85	6.10	-	0.9
[77]	In-house (85 subjects)		Subject-specific	1.49*	-	0.84	1.62*	-	0.90
[138]	In-house (18 subjects)	DL (ECG, PPG)	Subject-specific	2.03	2.57	0.76	2.62	3.36	0.77
[73]	In-house (48 subjects)	Correlation Analysis (BCG)	Subject-specific	-	-	-	-	-	0.9
[78]	MIMIC II (942 subjects)	DL (PPG)	Globalized model	1.75	2.82	-	3.40	5.49	-
[79]	MIMIC II (942 subjects)	DL (ECG, PPG)	Globalized model	0.71	-	-	2.33	-	-
[81]	MIMIC II (942 subjects)	DL (PPG)	Globalized model	2.89	-	-	5.16	-	-
[143]	UCI ML dataset	DL (ECG, PPG)	Globalized	-	-	-	-	2.95*	-

The table summarizes the state-of-the-art studies for non-invasive blood pressure estimation and their measurements, calibration approach, and performance. For the performance, the values are reported in several different metrics including correlation (r), root mean squared error/mean error (RMSE/MSE/ME) (in mmHg), between the predicted and actual values. * Indicates mean difference error (ME) instead of MAE.

PPG, and continuous finger cuff BP sensor attached to his/her body.

In each posture, a series of perturbations followed by rest periods were performed to modulate BP. First, a mental arithmetic exercise was conducted in which subjects were given a three-digit integer and were told to add the sum of the digits to the number repeatedly for 1 minute. Then, a Valsalva maneuver was performed to induce a transient decrease in BP, in which subjects held their breath for 15 seconds and attempted to forcefully breathe out as if blowing up a balloon while closing their mouth and pinching their nose. For hand-grip exercise, subjects were squeezing an adjustable resistance hand gripper for up to 2 minutes. Finally, during the cold pressor, subjects immersed their left hand without sensors in a bucket of ice water for 1 minute to increase BP.

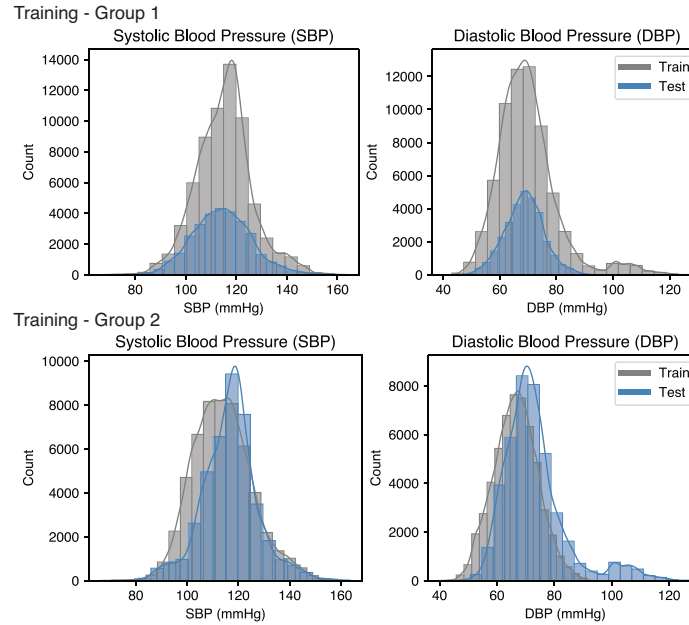


Figure 4.2: The histograms show the distribution of systolic (SBP) and diastolic pressure (DBP) measured by the finger BP cuff. The gray and blue represents the distribution of BP values in the training and test set, respectively. The top and bottom rows represent two different train/test splits used for the DL-based model.

Perturbations used in this work were chosen based on the literature [135]. These per-

turbations were introduced to induce large variability in BP such that the model or the calibration curve could be trained and tested on the wide range of BP values. In addition, these perturbations were easily done in static positions to reduce the effect of motion artifacts on the recorded signals. Figure 4.2 illustrates the histogram for the SBP and DBP measured in this study, showing the large variability. The grey and blue on the plot shows the distribution of BP for the train and test sets, respectively and the top and bottom plot represent two different train/test split which will be discussed in Section 4.2.4.3, for the DL-based models.

During the protocol, the perturbations were repeated for four different postures—supine, left/right lateral, and sitting—to investigate the effects of postural variability. Note that the Valsalva maneuver and cold pressor were conducted only for the supine posture to reduce the overall protocol length per visit. For the sitting posture, the bed was articulated such that the head-of-bed angle becomes 45° . Among 20 subjects recruited, 17 subjects visited the lab again within a month for the follow-up measurements to investigate the day-to-day variability. The protocol for the follow-up visit was the same as the first visit. For the evaluation, only the subjects who completed the full protocol were included and one subject was excluded due to noisy reference BP recording.

In this study, ECG, BCG, and the ground truth continuous BP were recorded. The placement of all the sensors and an example plot for a typical PPG and BCG signal is shown in Figure 4.1 for one heartbeat cycle. For the ECG signal, adhesive Ag/AgCl electrodes were placed in lead II configuration. The ECG signals were amplified and acquired through a wireless module (BN-EL50, Biopac Systems). BCG signals were acquired from the four load cells embedded on the Centrella® bed. The outputs from the load cells were

amplified through a custom-designed analog front end (AFE) to obtain BCG signals as done in previous studies [66]. Also, PPG signals were measured from the right index finger and toe using the pulse oximeter (OXY100E, Biopac Systems) sensor.

To obtain the ground truth BP values, a finger-cuff BP sensor based on the volume-clamp methodology (ccNexfin, Edwards Lifesciences) was placed on the same hand (right) as the finger pulse oximeter, acquiring a reference measurement of continuous beat-by-beat BP. From each BP beat, SBP, DBP, and mean arterial pressure (MAP) were derived as maximum, minimum, and addition of two-thirds of SBP and one-third of DBP. To ensure the calibration of the finger-cuff BP sensor was done properly, at the beginning of each posture, the BP measurements were also taken from an oscillometric BP cuff (Omron, Kyoto, Japan). Recordings for each posture only started when the BP values from the oscillometric cuff and the finger cuff closely agreed with each other. All signals were recorded through an MP160 data acquisition system (DAQ, Biopac Systems) at a sampling rate of 1 kHz.

4.2.2 Pre-Processing

Figure 4.3 depicts the overall signal processing pipeline. All signal processing and statistical analyses were performed in Python 3.7. Before extracting features, ECG, BCG, and PPG signals were first band-pass filtered using Butterworth infinite impulse response (IIR) filters. The cut-off frequencies were 1-8 Hz for PPG, 0.5-15 Hz for BCG, and 1-30 Hz for ECG to remove high-frequency noise out of cardiac frequency range and baseline wander caused by respiration. In addition, the continuous BP waveform was low-pass filtered with an IIR filter at the cut-off of 3.5 Hz to smooth out the waveform while maintaining the DC

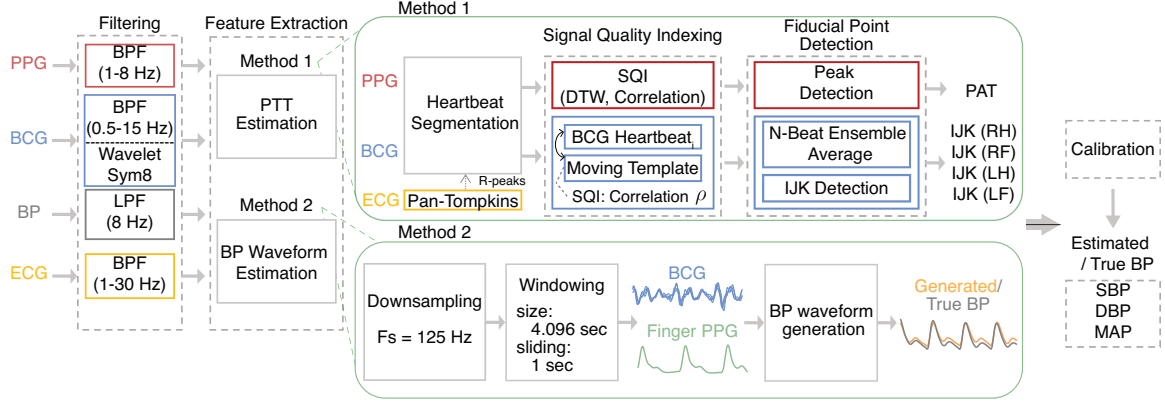


Figure 4.3: The overview of signal processing pipeline. ECG, PPG, and BCG signals were first band-pass filtered and BP signals were low-pass filtered to smooth out. The feature extraction was done in two ways—the signal processing-based extraction of PTT and deep learning (DL) model for data driven feature extraction. For the signal processing approach, the SQI was computed from each signal to remove segments corrupted by the motion artifacts. Fiducial points were detected to compute features including PAT and PTT. For the DL-based approach, the U-Net architecture was used to translate PPG and BCG waveforms into the BP waveform. From the extracted features, the calibration was performed for both methods to estimate systolic (SBP), diastolic (DBP), and the mean arterial pressure (MAP).

values. To offset the non-linear phase response of the IIR filter, filtering was done in both the forward and reverse directions.

After filtering, two different approaches were explored for the extraction of features relevant to BP from BCG and PPG signals. First is the signal processing-based extraction of PTT to investigate the estimation of BP by leveraging the physiologically known relationship (i.e. the inverse linear correlation) between PTT and the BP as done in the previous studies [136, 137, 26, 146, 147]. The second approach uses the U-Net [97], a DL architecture that was originally proposed for the segmentation of medical images and has shown a promise in many applications including signal to signal translation for cardiac waveforms [148, 100, 81, 149] and denoising of time-series signals [140, 141, 150]. In this study, the BP waveform was generated with the U-Net architecture from the 4-channel

BCG and finger PPG signals to estimate the BP. The following sections describe the details for each method.

4.2.3 Signal Processing-based Feature Extraction

4.2.3.1 Signal Quality Indexing

Before extracting features, the R-peaks of ECG were first detected using the Pan-Tompkins algorithm [151]. Detected R-peaks were then used to segment PPG, BCG, and BP waveforms into cardiac cycles. Then, the signal quality of these heartbeat-indexed signals was assessed for each subject using the signal quality assessment in [152] to remove the segments corrupted by the motion artifacts.

For PPG signals, the signal quality index (SQI) was computed for each heartbeat as described in the previous work [152]. The method quantifies the similarity between each heartbeat and the template by four different methods including the direct correlation, dynamic time warping (DTW), linear resampling, and clipping detection. Heartbeats that were possibly corrupted were removed using the threshold suggested in [152]. A similar approach was taken for BCG signals in which the correlation between each heartbeat and the template was computed. Instead of thresholding on the computed SQIs, heartbeats with SQI that belong to the bottom 20 percent were removed. For both PPG and BCG, the template was generated for each heartbeat cycle from the moving average of the last 30 beats. All channels—finger and toe for PPG and four load cell channels for BCG—were processed in the same way.

Because the finger BP cuff sensor intermittently performs an automatic pressure recal-

ibration step, BP heartbeats during this period are generally characterized by a small physiological implausible variability within one cardiac cycle. Affected beats were removed using the correlation SQI and thresholding on the standard deviation.

After removing low-fidelity heartbeats through the aforementioned signal quality assessment process, each heartbeat-indexed signal was ensemble-averaged using 8-beat sliding windows to acquire more robust heartbeats for the fiducial point detection.

4.2.3.2 Fiducial Point Detection

The detection of timing references for PTT computation—the foot/peak of the PPG and the IJK complex of BCG described in Figure 4.1 was done similarly to the previous studies [145, 26, 153]. In particular, the foot of the PPG was determined by the intersecting tangent method described in [145]. Along with the foot, the locations for the maximum 1st order derivative and peak following the foot were also detected.

For the robust detection of I, J, and K-waves in BCG heartbeats, a sliding template matching algorithm was used, in which extrema were found in each heartbeat using fiducial points in the template as references. For the initial few beats in the recordings, a physiologically realistic constraint for possible J-wave location (i.e. within 120-350 ms from ECG R- peak) was imposed based on [87] to ensure robust I, J, and K detection on initial templates. Subsequent templates for each heart beat were formed using the previous 30 beats.

Finally, the PTT was calculated as the difference of the proximal timing reference, the J-wave of the corresponding BCG heartbeat, and distal timing reference, location of the maximum 1st order derivative on the finger or toe PPG. Unlike the previous studies [153,

146] where the PTT was commonly computed as the timing delay between the I-wave of BCG and foot of the PPG, J-wave of BCG and maximum 1st order derivative of the PPG were used in this work to ensure that the same morphological peak was consistently chosen across subjects and postures. Occasionally, the I-wave in BCG is challenging to detect, especially when the subjects are in lateral postures. To avoid inconsistency in computed PTT arising from I-wave detection error, the J-wave, which is relatively less challenging to find was utilized. As the J-wave comes after the I-wave, to ensure that the J-wave occurs before the distal timing point in PPG, the maximum 1st order derivative was used instead of the foot. These steps were repeated for each BCG channel.

4.2.4 Neural Network-based Feature Extraction

For a more end-to-end approach that replaces the signal processing steps, including segmentation into cardiac cycles and detection of fiducial points, with the neural networks, in the second approach for the feature extraction, a DL architecture called U-Net was used.

4.2.4.1 Source/Target Signals

In this approach, the finger PPG and 4-channel BCG signals were used as inputs (i.e. source signals) and the BP waveforms measured by the finger BP cuff were used as the outputs (i.e. target signal). Finger PPG was used instead of using toe PPG or both PPG sources to match the signals in external dataset used for the model training as described in the later section.

For each subject and posture, the time-series PPG, BCG, and the BP recordings were first filtered according to Section 4.2.2 and then downsampled to 125 Hz. Note that the

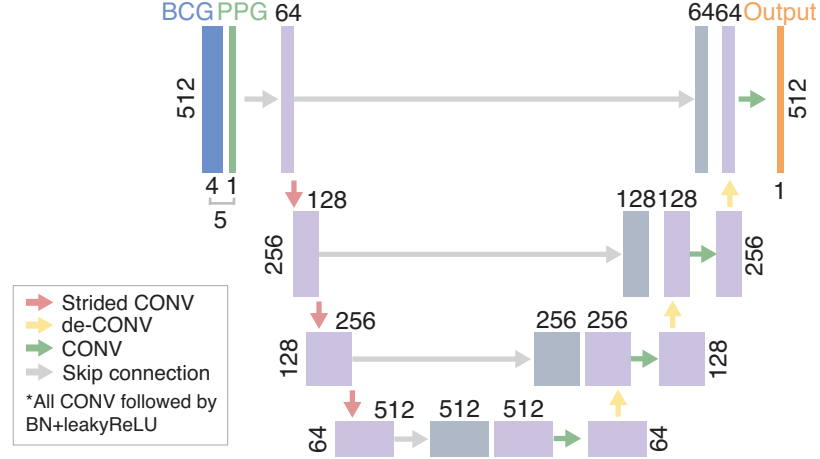


Figure 4.4: The overview of the U-Net architecture. The architecture has three parts: the contraction, and expansion path. The dimension of the signal is written on the left/right side of the feature map and the number of channels is written on the top of the feature map. CONV-1D convolutional layer, BN-Batch Normalization, leaky ReLU-leaky Rectified Linear Unit. Red: Strided CONV+BN+leaky ReLU, Yellow: tranposed CONV+BN+leaky ReLu, Gray: Skip connections

downsampled signals were used instead of the original signals sampled at 1 kHz to reduce the dimension of the signal to make the model training and testing faster and 125 Hz was chosen based on previous studies [78, 79, 154, 81, 75, 80, 144]. Both the source and target signals were then segmented into 512-samples long (4.096 seconds) windows with 125 samples (1 second) overlap between the windows and each window served as a single training/testing instance for the model.

To remove the windows with the invalid BP waveforms (i.e. the BP signals recorded while the finger BP sensor was calibrating), the windows containing the invalid BP beats identified in the process described in Section II-C-(1) were rejected.

4.2.4.2 U-Net Architecture

To generate BP waveforms from PPG and BCG signals, the U-Net architecture [97] was used in this work. The overall architecture is composed of two parts—the contractive and

expansive path—as shown in Figure 4.4.

The contractive path implementation is similar to the original U-Net model in [97] which consists of cascaded layers of convolution, batch normalization and non-linear activation. The contractive path takes the 4-channel BCG signals and a single channel PPG signal stacked along the channel dimension as an input. The input has a dimension of $N_{mini-batch} \times 5 \times 512$, where 512 represents the signal length from aforementioned windowing scheme. $N_{mini-batch}$ size was set as 40 in this study.

The contractive path reduces the dimension of the input by half while doubling the number of channels for each layer. Instead of using the max-pooling layer in the original U-Net, to reduce the dimension of the signal, a strided convolution (strided CONV) with stride of 2 and the kernel size of 11 were used in this work. This was followed by a batch normalization (BN) to accelerate the model training and leaky ReLU (Rectified Linear Unit) as a non-linear activation. These alterations were chosen based on the previous signal to signal translation problems using U-Net inspired DL architectures [100, 78, 81, 79]. The contractive path allows the model to learn a compact representation of the input data by recursively reducing the dimension while increasing the number of channels.

The expansive path mirrors the structure in the contractive path to restore the original signal dimension through de-convolutions (i.e. transposed convolution). Each layer first performs transposed convolution on the output from the previous layer. It also takes the feature map from the corresponding layer in the contractive path through the skip connections and concatenates with the output from the transposed convolution along the channel dimension. Then, convolution is performed on the concatenated feature map to halve the number of channels. Concatenating high resolution features from the contracting path al-

allows the model to better construct target signals during the expansive path. For the final layers, instead of halving the number of channels, the channel dimension was reduced to 1 to output the final single-channel BP waveform. As done in the contractive path, the transposed convolution was followed by the BN and the leaky ReLU. In both the contractive and expansive path, the input to each layer was padded such that the dimension could be exactly doubled/halved from the previous input dimension. For the transposed CONV (yellow in Figure 4.4), the kernel size of 4 was used, and for the CONV (green), the kernel size of 11 was used. For both the contractive and expansive path, the slope of 0.2 was used for the leaky ReLU.

4.2.4.3 Model Training and Testing

For the model training, in addition to the dataset collected from the protocol in Section 4.2.1, a publicly available dataset [96] (referred to as “public BCG dataset” in this work) was also used to increase the number of training instances. In the public BCG dataset, the ECG, PPG, 4-channel load cell BCG, and continuous BP waveform from the finger BP cuff were recorded at a sampling rate of 1 kHz. The signals were downsampled to 125 Hz before feeding into the model. In total, the data were collected from 40 subjects (17 males, 23 females) while staying motionless on the bed. Unlike the in-house dataset collected in this study, subjects were not performing any tasks to modulate the BP nor were they asked to vary postures.

For the training, 30 subjects from the public BCG dataset were included along with 10 subjects from the in-house dataset. The remaining 10 subjects in the public BCG dataset were included in the validation set. Of the remaining subjects in the in-house dataset, 3

were used for validation and 5 were used for testing. The model training was performed twice with the same model architecture and hyperparameters but with different training, validation, and test split. A different set of training/validation/test subjects were chosen from the in-house dataset to evaluate the performance on a sufficient number of subjects from the in-house dataset. The two different splits have led to 65547/13933/20770 and 54935/17253/28062 instances for training, validation, and testing respectively. The distribution for each scheme is shown in Figure 4.2, where grey represents training subjects and blue represents validation/testing subjects.

For training, a batch size of 40, an initial learning rate 0.001, and the Adam optimizer were used. The model was trained against the mean absolute error (MAE) between the generated and the target waveform.

Before training, each source signal was normalized to zero mean and unit variance and the target signals were globally normalized across all instances such that all target BP waveforms lie in the range between -1 and +1. The statistics from training set used for normalization were later applied to the generated waveforms during the testing.

4.2.5 Calibration

4.2.5.1 Calibration for PTT

The relationship between the BP and the PTT is commonly modeled by the Moens–Korteweg equation [135] shown in (Equation 4.1) below. The slope K_1 and the y-intercept K_2 in (Equation 4.1) are known to be subject-specific, thus requiring subject-specific calibration for the absolute estimation of BP from PTT. In addition, the BCG heartbeat morphology

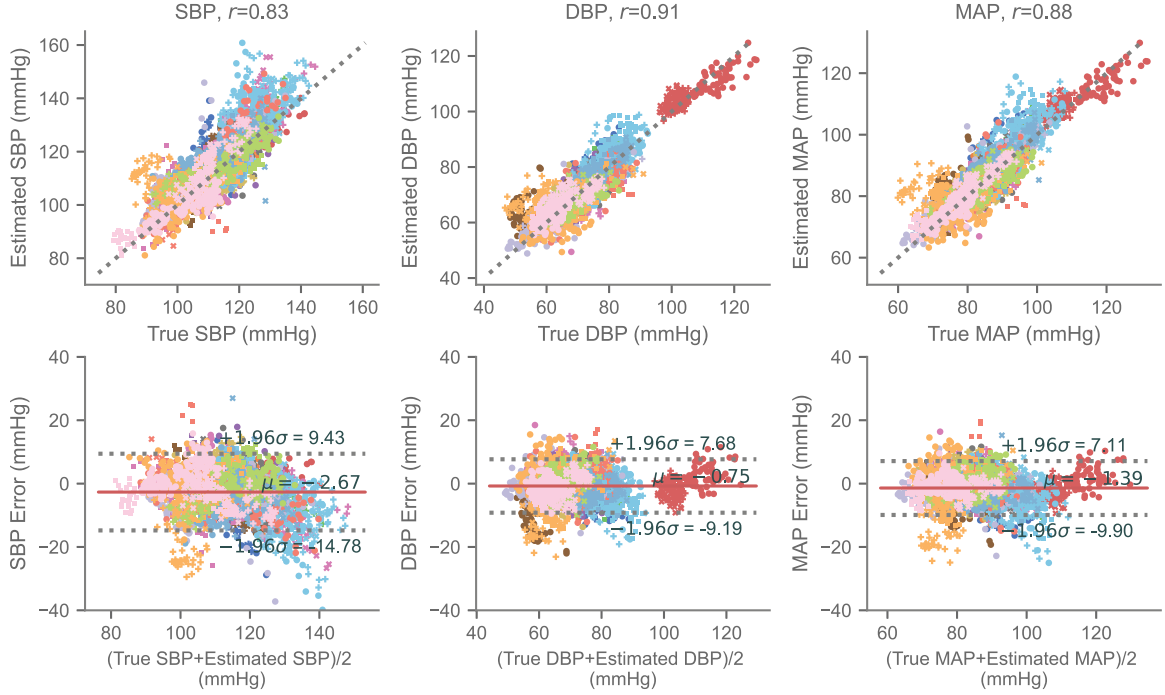


Figure 4.5: The overview of the BP estimation results for each BP component. The color and shape on the plot represent different subjects and posture, respectively. (Top) The plot shows the correlation between the estimated and the true BP. (Bottom) The plot shows the error distribution for each BP component. The 95 % limit of agreement (LoA) is represented by the horizontal dotted lines.

is known to be affected by the postural changes; requiring posture-specific calibration as well.

To explore the effects of such variability, multiple linear regression was performed independently on subject-specific SBP, DBP, SBP, and inverse PTT pairs to determine a pair of K_1 and K_2 coefficients for each of the three BP components per subject. The calibration coefficients were determined by finding the slope and y-intercept that best fit the calibration data.

$$BP = \frac{K_1}{PTT} + K_2 \quad (4.1)$$

For calibration, the first two minutes of recording during the baseline period were used. For testing, the obtained calibration curve was applied to the remaining data points for each subject. To perform linear regression robust to outliers, 5-fold cross-validation was used and the slope and intercept of the model that achieved the highest cross-validation score were determined as K_1 and K_2 . For the evaluation, the 10-point moving average was done without overlap to aggregate 10 predictions together. Here each prediction was from one ensemble-averaged heartbeat. For the channel selection, the channel with the best quality was chosen during the calibration and the same channel was used for the testing as well.

4.2.5.2 Re-scaling the generated BP waveforms

For the U-Net models, the peaks and valleys were detected from the generated BP waveform in each window and served as relative SBP and DBP estimates. These relative SBP and DBP estimates correlated in trend with the true SBP and DBP values, however, the absolute values were often offset by a certain bias and thus required subject-specific re-scaling.

$$bias = \frac{1}{M} \sum_{n=1}^M BP_{true}(n) - BP_{est,relative}(n) \quad (4.2)$$

To re-scale relative SBP and DBP estimates back to the actual BP range specific to each subject, the bias was measured from the average offset of the first 13 instances—corresponds to 15 seconds—of both the true and relative estimations of SBP and DBP as shown in Equation 2. Here, although the offsets were measured from the average of continuous BP over

a few seconds, in practice, this could be measured from multiple (e.g. two to three) single-timepoint BP measurements from a conventional oscillometric cuff without having continuous BP waveform measurements. The relative SBP and DBP estimates were offset by this baseline bias to be re-scaled to the subject-specific BP range.

4.2.6 Evaluation

For the evaluation, the mean absolute error (MAE) between the estimated and the reference BP values and the overall Pearson’s correlation r were reported. Also, the Bland-Altman plots were presented for the final model to understand the error distribution.

To assess effects of different sensing modalities (toe/finger PPG, and BCG), two PTT-based models—the toe PTT (tPTT) and finger PTT (fPTT)—and the two U-Net models—a single-modal model using PPG alone and the multi-modal model using both BCG and PPG—were evaluated. For the evaluation of the calibration or re-scaling frequency pertinent to postural variability, the calibration or re-scaling was performed in two ways—per day and posture and per day only (i.e. calibration once per day only in supine posture) for each subject.

4.3 Results

4.3.1 Calibration per day and posture

4.3.1.1 PTT-based method

Table 4.2 presents the overall BP estimation error after calibrating the inverse of PTT to the SBP and DBP separately. The finger PTT (fPTT) here indicates the time delay between the

Table 4.2: Results: PTT vs U-Net

		fPTT		tPTT		U-Net (PPG)		U-Net (BCG, PPG)	
		MAE	r	MAE	r	MAE	r	MAE	r
Per Day & Posture	SBP	6.36	0.78	5.88	0.81	5.52	0.80	5.05	0.83
	DBP	3.72	0.82	3.42	0.85	3.44	0.81	3.22	0.83
	MAP	4.38	0.78	4.01	0.82	3.68	0.82	3.35	0.84
Per Day	SBP	15.74	0.17	13.98	0.35	8.19	0.54	6.72	0.65
	DBP	10.48	0.20	8.12	0.37	5.20	0.61	4.22	0.72
	MAP	11.58	0.16	9.55	0.34	5.58	0.59	4.50	0.71

The table summarizes the BP estimation error from 14 subjects for the two PTT-based (finger and toe) and U-Net-based (single-modal and multi-modal) models. The first three rows show the results after performing calibration per day and posture for each subject. The last three rows show the results for calibrating per day only. The errors are shown in mean absolute error (MAE) in mmHg, and the Pearson's correlation r between the true and estimated BP values. fPTT: finger PTT, tPPT: toe PTT

J-wave of BCG and the maximum derivative of finger PPG and toe PTT (tPTT) indicates the the same calculation, but using toe PPG instead. When calibration was performed per day and posture for each subject the overall correlation between the true and the estimated BP was 0.78 and 0.82 for fPTT and 0.81 and 0.85 for tPTT respectively for SBP and DBP. For the MAP, the correlation was similar—0.78 and 0.82 for fPTT and tPTT, respectively. The mean absolute error (MAE) was lower in tPTT as well as shown in Table 4.3, where the average MAE across subjects were 6.33 mmHg and 3.74 mmHg in fPTT and 5.83 mmHg and 3.43 mmHg in tPTT for SBP and DBP.

4.3.1.2 U-Net-based method

The overall BP estimation errors for the U-Net-based methods are shown on the last two columns in Table 4.2. Like the PTT-based methods, two different U-Net modality configurations were evaluated—the single-modality U-Net (i.e. PPG signals only) and the multi-modality U-Net (i.e. BCG and PPG signals). When re-scaled per day and posture

Table 4.3: Subject-wise BP Estimation Error (MAE)

Subject	SBP (mmHg)				DBP (mmHg)				MAP (mmHg)			
	fPTT	tPTT	UNet PPG	UNet BCG-PPG	fPTT	tPTT	UNet PPG	UNet BCG-PPG	fPTT	tPTT	UNet PPG	UNet BCG-PPG
1.0	5.92	5.53	6.00	4.97	3.79	3.63	3.44	3.05	4.22	3.98	3.80	3.30
2.0	3.42	3.35	3.03	3.16	2.68	2.59	2.05	2.04	2.85	2.79	2.20	2.25
3.0	4.32	3.86	4.25	3.80	3.27	2.97	3.07	2.34	3.49	3.16	3.37	2.63
5.0	6.24	5.41	4.12	3.88	3.75	2.97	2.94	2.83	4.39	3.55	3.12	2.93
7.0	6.15	5.79	6.11	4.38	3.47	3.18	4.07	3.79	4.20	3.90	4.38	3.72
10.0	9.83	8.70	7.18	6.29	4.73	4.40	4.00	2.92	6.26	5.66	3.85	3.00
12.0	4.94	4.92	4.18	4.42	2.35	2.37	2.41	3.16	3.12	3.13	2.41	3.12
14.0	9.19	9.27	9.54	8.18	5.62	5.31	4.40	4.22	6.61	6.39	5.89	5.15
15.0	6.12	4.80	5.07	5.10	3.77	2.98	2.50	2.55	4.33	3.30	2.92	2.68
16.0	9.21	9.00	6.24	5.21	4.63	4.78	3.97	3.33	5.88	5.95	4.16	3.25
17.0	5.57	5.69	4.84	4.96	2.63	2.62	3.44	2.39	3.35	3.42	3.49	2.99
18.0	5.98	5.66	7.26	7.35	4.09	3.77	4.93	6.27	4.52	4.14	5.41	6.37
19.0	5.62	3.84	4.84	4.43	4.17	3.32	3.62	3.40	4.46	3.25	3.64	3.23
20.0	6.10	5.77	4.50	4.64	3.37	3.10	3.61	3.08	3.68	3.34	2.88	2.36
Mean	6.33	5.83	5.51	5.05	3.74	3.43	3.46	3.24	4.38	4.00	3.68	3.36
STD	1.79	1.82	1.62	1.32	0.86	0.84	0.78	1.01	1.11	1.11	1.00	1.08

Subject-wise error for BP estimation. The reported values are mean absolute error (MAE, Unit: mmHg) between the predicted and actual BP for each subject. fPTT: finger PTT, tPTT: toe PTT, UNet PPG: single-modal U-Net method using the PPG signals as a source, UNet BCG-PPG: multi-modal U-Net method using the BCG and PPG signals as source.

for each subject, the overall correlations between the true and the estimated values were 0.80, 0.81, and 0.82 in single-modal U-Net and 0.83, 0.83, and 0.84 in multi-modal U-Net for SBP, DBP, and MAP, respectively. In the multi-modal U-Net, this corresponds to a MAE of 5.05 mmHg, 3.22 mmHg, and 3.35 mmHg for SBP, DBP, and MAP respectively as shown in Table 4.3. Therefore, the overall results for the multi-modality model were similar to the fPTT in this calibration scheme with slightly lower MAE compared to the tPTT.

When only the PPG signal was used as a source, the average MAE for SBP, DBP and MAP increased to 5.51 mmHg, 3.46 mmHg, and 3.68 mmHg compared to when both BCG and PPG were used as the source. Here the same U-Net architecture and the hyperparameter set were used for the two models but only the source signals were different. Note that with the U-Net-based method, only the finger PPG was used as the public BCG dataset used for the model training only has the finger PPG measurements.

Figure 4.5 illustrates Bland-Altman plot for the best performing model—the multi-modal U-Net in this study. On the plot, the subjects were represented with different colors and the postures were represented with different shapes. The upper rows show the overall correlation between the estimated and true values for each BP component. The bottom row shows the error distribution, where the dotted line shows the 95 % limit of agreement (LoA). The 95 % LoA were [-14.78, 9.43], [- 9.19, 7.68], and [-9.90, 7.11] in mmHg for SBP, DBP and MAP.

4.3.2 Calibration per day

4.3.2.1 PTT-based method

In this section, the posture specific calibration was removed, and the calibration was performed once per day during the first 2 minutes of supine posture for each subject. The calibration curve obtained here was applied to the remaining datapoints from other postures on the same day. Table 4.2 shows the overall results for this calibration scheme.

Without the posture-specific calibration, the correlation has decreased to 0.17, 0.20, and 0.16 in fPTT and 0.35, 0.37, and 0.34 in tPTT for SBP, DBP, and MAP. Similarly, the MAE has increased to 15.74 mmHg, 10.48 mmHg, and 11.58 mmHg in fPTT and 13.98 mmHg, 8.12 mmHg, and 9.55 mmHg in tPTT for SBP, DBP and MAP.

4.3.2.2 U-Net-based method

Similarly, for the U-Net-based methods, when re-scaled once per day only, the MAE has increased to 8.19 mmHg, 5.20 mmHg, and 5.58 mmHg in the single-modal model for SBP, DBP, and MAP. The increase in error was observed in the multi-modal model as well—the MAE was 6.72 mmHg, 4.22 mmHg, and 4.50 mmHg with overall correlation of 0.65, 0.72, and 0.71 for SBP, DBP, and MAP. Still, the multi-modal U-Net performed better than the single-modal U-Net or the PTT-based methods. All results here are presented in Table 4.2 and subject-wise MAE is also shown in Table 4.3 for all four models used in the analysis. Note that only the subjects available for both the PTT and U-Net approach were included in the results.

4.4 Discussion

4.4.1 Comparison between finger and toe PPG

When comparing the estimation results between the fPTT and tPTT in Table 4.3 and Table 4.3, the tPTT achieved higher accuracy given the same calibration scheme (per day and posture calibration). Better correlation with toe PPG was also observed in [155]. In [155], the toe PAT (the time delay between the ECG R-peak and the foot of the toe PPG waveform) correlated better than the finger PAT, particularly for the SBP than DBP. Though this study mainly focused on PAT, the PTT showed a similar trend where the PTT detected from the time delay between the ear PPG and toe PPG yielded better correlation compared to the corresponding PTT with finger PPG.

This could be due to smooth muscle contraction which is a well-known confounder of the PTT-based BP monitoring [20]. PPG sensors are most commonly placed at the finger as well as other upper extremity locations to obtain a distal timing reference for PTT extraction. However, these locations are often confounded by the smooth muscle contraction which leads to decrease in correlation to BP. Lower extremity locations such as the toe are less susceptible in that sense as it enables PTT to be measured through the aorta [135, 20]. However, the finger PPG or the other upper extremity locations such as the wrist are mostly preferred as they are more convenient to measure with non-invasive devices such as smartwatches and finger pulse oximeters.

4.4.2 Source signals in U-Net

With the advances in DL technologies, several studies have demonstrated using the PPG signal alone to generate BP waveform using the state-of-the-art deep architectures [78, 79, 81, 143, 144]. As the PPG waveform by nature has morphological similarity to the BP waveform [20], these studies have shown success on some levels. However, using the PPG signals alone to estimate BP poses some limitations. Due to the viscoelasticity of the wall of small peripheral arteries for which PPG is applied, the PPG waveform tends to be smoother in morphology and delayed in phase relative to the BP waveform despite its morphological similarity. Also, the PPG sensor contact pressure is an additional complication factor to the PPG waveform [20]. Therefore, relying only on PPG waveforms to monitor BP could lead to some errors.

Conventionally, in many physiology-based analyses [145, 26, 136, 137, 135, 20, 156, 155], PTT using BCG and PPG as a proximal and distal reference has shown a better correlation to BP than the PPG morphological features (i.e. peak amplitudes) or the PAT (the time delay between ECG R-peak and foot of the PPG). However, relatively less studies have been done in deploying DL models with multiple sensing modalities such as a combination of PPG and BCG as very few datasets with simultaneously measured PPG, BCG, and continuous BP are available to train and evaluate such DL models.

Therefore, in this study, we explored using both the PPG and BCG signals to generate BP waveforms using the DL models. The main idea behind using both BCG and PPG signals here was to leverage the morphological similarity of PPG waveforms to BP waveforms while allowing the model to learn the underlying relationship between PPG and BCG

signals which would help better construct the target BP waveform.

The results in Table 4.3 support this idea by showing the improved performance in the multi-modal U-Net model. This suggests the feasibility that the DL model could learn both the morphological and inter-modality relationship to generate a more realistic BP waveform.

Despite a larger correlation between the toe PPG and the BP as discussed in the previous section, for the U-Net model, the finger PPG was used over toe PPG as only the finger PPG was available for both the public BCG dataset and the in-house dataset. In future studies, the multi-modal U-Net model with the toe PPG could be investigated to further improve BP waveform generation.

4.4.3 Comparison between PTT and U-Net

From the results in Table 4.3, the tPTT model and multi-modal U-Net performed comparably with slightly lower MAE with the U-Net model when calibrated per day and posture for each subject. Without posture-specific calibration in per day calibration scheme, though the correlation has decreased for both models, the U-Net model yielded significantly better correlation compared to the tPTT model. This demonstrates that while PTT is heavily affected by the posture, the U-Net model is relatively robust to postural variability.

One reason behind the significant drop in estimation accuracy in the PTT-based model could be morphological distortion in the BCG caused by the posture. The postural effect on BCG morphology is a well-known challenge in BCG monitoring, particularly for the bed-based system [102, 66]. Such distortion leads to changes in detected PTT and thus varies the linear mapping between the PTT and the BP according to the postural changes.

This requires posture-specific calibration to track absolute BP values. Also, for the PTT, although some noisy beats were removed through the signal quality indexing, the fiducial point detection could be challenging in some postures like the laterals, leading to error in PTT extraction and ultimately inaccurate BP predictions. Rather than having a fixed threshold for removing the beats, dynamic thresholding on SQI could further improve PTT extraction.

The other reason could be channel selection. In this study, we used the channel chosen based on signal quality assessment during the calibration period (during the baseline period in supine in the per day calibration scheme) to predict the BP values during the test period as different channels often have different calibration curves. However, the best channel during the calibration may not necessarily be the best during testing. The optimization of channel selection or a combination could be done to improve in estimation accuracy in the PTT-based model.

4.4.4 Calibration

To estimate the absolute BP values for the PTT and U-Net models, the extracted PTT or the BP waveform had to be calibrated for each subject.

For PTT calibration, the K_1 and K_2 coefficients in Equation 4.1 are known to be person-specific [145, 26, 136, 137, 135, 20, 156]. The K_1 value is determined by the underlying baseline vascular stiffness, whereas K_2 represents the inherently correlated bias in baseline BP; which all varies from person-to-person.

Also, particularly for the bed-based BCG system like the one in this study, the morphological distortion in BCG is often observed [66, 102], leading to changes in fiducial point

timings in the heartbeat. In addition, physiologically, the BP itself is known to be affected by the posture as well [157, 158, 159, 160]. Having both the morphological distortion in BCG and the postural effects on BP, it is not surprising that the calibration curve is required per posture and posture for accurate BP estimates.

Therefore, when removing the posture-specific calibration, the estimation accuracy decreased for both PTT and U-Net methods. However, compared to the PTT-based model, the U-Net model's performance was less affected by the postural changes and the DBP error remained under grade A criteria for wearable BP monitoring devices based on the IEEE standard [161].

Though the U-Net model performed better than the PTT-based model overall, the generated BP waveform from the U-Net model could not be used directly without subject-specific re-scaling to estimate absolute BP values unlike some studies using the DL model [78, 79, 154, 81, 75, 80, 144]. In [78], for example, the globalized DL model generated BP waveforms from single-channel PPG signals with high estimation accuracy (MAE of 3.50 mmHg for SBP, 1.81 mmHg for DBP). However, in this study, the output from the U-Net model required re-scaling for a new subject to achieve high estimation accuracy. This could be because of the limited number of subjects ($n = 40$) used for the training. Also, using the BP waveform as a target signal in this study may not be accurate compared to the invasively measured arterial BP in MIMIC II Waveform dataset used in many studies [78, 79, 154, 81, 75, 80, 144]. The BP measured by a finger BP cuff serves as a robust surrogate for ground truth continuous BP measurements and has been validated in previous studies [136, 137, 26, 146, 155, 96, 145]. However, signals from this device could have some measurement errors, particularly while calibrating. Therefore, the measurements from this device may

not be suitable as a reference for the BP “waveform” although it could provide robust SBP and DBP values when averaged over a few seconds.

4.4.5 Limitations and Future Work

There are a few limitations in this work. First, the dataset used in this work only includes a limited number of subjects (20 subjects for the in-house, 40 subjects for the public BCG dataset). Also, all subjects in the analysis were relatively young and healthy without hypertension or any known history of cardiovascular diseases. To mitigate this, the protocol for the human subjects study included perturbations to modulate BP such that large variability in measured BP can be observed even with the limited number of subjects. However, high BP instances were still rare as shown in Figure 4.2, thus relatively large error was observed for the subjects with relatively high BP compared to other subjects in the dataset. Future work will include more subjects with diverse demographics and potentially hypertensive populations as well. Second, as observed in previous BP estimation studies as well, the calibration remained the key challenge in this work. Particularly with the postural changes, more frequent calibration had to be done for both PTT and U-Net models. With more data, future work could further investigate the postural effects on BCG and BP signals to reduce calibration requirements. Considering that this bed-based BCG system is mainly aimed at the hospital settings where measuring BP with conventional methods such as oscillometric cuff at least once a day is common, reducing the calibration requirement to just once per day could have significant meaning.

Third, the estimation error could be further improved. Though the results in this work were evaluated against the in-house dataset which is more challenging due to surrogate

ground truth measurements and extra complications from the postural variability, the estimation error was relatively larger than other studies using the well-studied MIMIC II dataset [162]. Future work will focus on improving the algorithm performance based on the observation from the work. For PTT-based models, the utilization of four load cell channels could be optimized to further improve the PTT estimation. For the U-Net models, the variants of the U-Net architecture—adding the attention gates [149] or residual blocks [78], for example—or other state-of-the-art DL architectures such as LSTM, CNN-LSTM or GAN could be explored as well.

4.5 Conclusion

In this study, we have demonstrated the algorithms for estimating BP using BCG signals recorded from the load cells on the hospital bed and PPG signals from the pulse oximeter sensors. Two different approaches were proposed for the extraction of the features—the conventional PTT-based method and the BP waveform estimation using the DL model. When calibrated per day and posture for each subject, the conventional PTT-based and U-Net-based models performed similarly. In the PTT-based method, the toe PTT correlated better to BP than finger PTT, and in the U-Net-based method, the multi-modal model outperformed a single-modal equivalent. Without the posture-specific calibration, the U-Net model showed a more robust performance compared to the PTT model. Although the estimation error has increased in general with less frequent calibration in both approaches, the estimation accuracy for DBP remained relatively small with U-Net models in this work, showing the feasibility of using the sensors already available in the hospitals—the load cells on the hospital bed and the pulse oximeters—to continuously monitor the BP. Yet, frequent

calibration, for each subject per day and posture, is required to achieve high estimation accuracy. The future work will focus on reducing calibration requirements while improving the error through analysis on the broader population to enable more robust and deployable BP monitoring.

CHAPTER 5

CONCLUSION AND FUTURE WORK

5.1 Conclusion

Monitoring vital signs is one of the most common and essential clinical needs to assess patients' physiologic states and apply adequate treatment promptly. Early recognition of abnormal vital signs and thus patient deterioration in hospitals is crucial to prevent serious adverse events leading to unplanned admission to the intensive care unit (ICU), prolonged hospitalization, long-term disability, or even unexpected deaths. To quantify the deterioration in the physiologic state, the early warning score (EWS) systems were proposed and have shown success in detecting medical emergencies; however, one of the limitations is the intermittency in vital measurement.

To mitigate this problem, continuous vitals monitoring solutions at the bedside have been proposed to detect deteriorating trends in vitals early. In this dissertation, we presented techniques to continuously estimate a set of vitals including the HR, RR, TV, and BP from the multi-channel BCG signals acquired using the load cells embedded on the hospital bed. We first explored signal processing techniques to estimate HR and RR, the most common and essential vitals used in hospitals. For the signal processing-based HR estimation, the IBI was estimated from a short segment of BCG signals by computing the probability of each candidate IBI being the actual IBI of the signal segment. An array processing algorithm that selectively combines the channel based on signal quality was proposed to

optimize the fusion of multiple load cell channels. A DL-based model was also presented with a large amount of data available in the later phase. In the DL-based approach, the BCG signals were transformed into a triangular waveform on which the heartbeat locations appear as valleys. While both methods achieved high estimation accuracy, the PDF-based method has an advantage in computational efficiency and the DL-based method provides an end-to-end solution.

This work demonstrated a robust RR estimation using the low-frequency component of the load cell signals for respiratory monitoring. Though not at the clinical-level accuracy, we also demonstrated the feasibility of monitoring the respiratory volume, opening the possibility for a continuous assessment of the pulmonary function.

Lastly, this work demonstrated BP monitoring in two different approaches. The conventional PTT-based and DL-based models showed similar performance when calibrated frequently, per day, and posture. However, the DL-based model outperformed when removing posture-specific calibration, demonstrating robustness against the postural variability. In sum, this work established robust and deployable methods in various settings, potentially improving continuous assessment of physiologic state in hospitals without adding extra cost or burden on the caregivers.

5.2 Future Work

Various future research directions could stem from this work. All human subjects studies in this work were done on healthy populations only. Although each protocol had specific perturbations to induce large variability in the target physiological parameters, the range of observed values was often limited due to a limited number of subjects from the relatively

young and healthy population. Also, the morphology of the cardiac signals such as BCG is known to be different for patients with cardiorespiratory diseases [163]. To deploy algorithms in this work for hospitalized patients, further studies should be done on the broader population including patients with cardiorespiratory conditions.

Future work could improve the model for the HR estimation algorithms so that the algorithms can be deployed on the devices. In the PDF-based algorithms, the thresholds and parameters related to PDF and Gaussian curve could be optimized through additional real-world data analysis. For example, instead of having the reference in the Gaussian weight curve updated every few seconds, it could be dynamically updated when the signal quality is high and keep the previous values or remove the weight curve when the motion heavily corrupts the signal. Though the DL model for HR estimation does not require hard-coded parameters except the threshold for the SNR, the computation complexity is high due to its deep structure. Further study can explore lighter architectures while maintaining the high accuracy for deploying the DL model on devices with computation or memory constraints.

For respiratory monitoring, TV monitoring, in particular, future work should improve the accuracy to meet the clinical criteria and elucidate the effects of different feature types (low-frequency vs. cardiac heartbeat features). With more data available, as done in the other section, DL models that leverage the morphological similarities between the low-frequency load cell signal and the ground truth respiration waveform could also be explored. Lastly, future studies should be done on the data collected under uncontrolled settings to engage natural breathing behaviors in addition to the simulated abnormal breathing patterns.

One of the major limitations of the PTT-based and the DL model in BP monitoring was the frequent calibration requirement. The results in this work indicated that both approaches were affected by the postures and the subject-specificity. Future work could further investigate the postural effects on BCG and BP signals to reduce calibration requirements on a larger dataset. Considering that this bed-based BCG system is mainly aimed at hospital settings where measuring BP with conventional methods such as oscillometric cuff at least once a day is common, reducing the calibration requirement to just once per day could have significant meaning. Also, future efforts can be made to improve estimation accuracy by engaging more elaborated architecture for the DL-based model or by optimizing the fusion of PTTs from multiple BCG channels for the PTT-based approach.

5.2.1 Final Remarks

With the recent advancement in technologies, an improvement in healthcare systems has been achieved. However, the number of adverse events in the hospitals remains high and many of those were deemed to be prevented with proper vital monitoring. In particular, such “preventable” adverse often come from the low-equipped settings where monitoring devices are often unavailable and the patient-to-nurse ratio is high. The scientific and technological advances stemmed from this work could significantly contribute to overcoming such problems by providing low-cost technologies to continuously monitor vitals from the existing sensors on the hospital beds without requiring extra attention from the caregivers. These algorithms could allow an in-depth quantification of physiologic state based on continuous measurement of basic vitals and serve as an extra safety net to detect patient deterioration. This dissertation constructs the basis of such a bed-based continuous vital

monitoring system that could be used in hospital settings to detect patient deterioration and in at-home settings to allow longitudinal health monitoring.

REFERENCES

- [1] E. J. Benjamin *et al.*, “Heart Disease and Stroke Statistics—2019 Update: A Report From the American Heart Association,” *Circulation*, vol. 139, no. 10, Mar. 2019.
- [2] C. Mathukia, W. Fan, K. Vadyak, C. Biege, and M. Krishnamurthy, “Modified Early Warning System improves patient safety and clinical outcomes in an academic community hospital,” *Journal of Community Hospital Internal Medicine Perspectives*, 2015.
- [3] Z. Zhang, Z. Pi, and B. Liu, “TROIKA: A General Framework for Heart Rate Monitoring Using Wrist-Type Photoplethysmographic Signals During Intensive Physical Exercise,” *IEEE Transactions on Biomedical Engineering*, vol. 62, no. 2, pp. 522–531, Feb. 2015.
- [4] C. H. Lund, L. B. Nonato, J. M. Kuller, L. S. Franck, C. Cullander, and D. K. Durand, “Disruption of barrier function in neonatal skin associated with adhesive removal,” *The Journal of Pediatrics*, vol. 131, no. 3, pp. 367–372, Sep. 1997.
- [5] M. E. Griffith, W. M. Portnoy, L. J. Stotts, and J. L. Day, “Improved capacitive electrocardiogram electrodes for burn applications,” *Medical & Biological Engineering & Computing*, vol. 17, no. 5, pp. 641–646, Sep. 1979.
- [6] O. T. Inan *et al.*, “Ballistocardiography and Seismocardiography: A Review of Recent Advances,” *IEEE Journal of Biomedical and Health Informatics*, 2015.
- [7] I. Sadek, T. T. S. Heng, E. Seet, and B. Abdulrazak, “A New Approach for Detecting Sleep Apnea Using a Contactless Bed Sensor: Comparison Study,” *Journal of Medical Internet Research*, vol. 22, no. 9, e18297, Sep. 2020.
- [8] C. Brüser, S. Winter, and S. Leonhardt, “Robust inter-beat interval estimation in cardiac vibration signals,” *Physiological Measurement*, vol. 34, no. 2, 2013.
- [9] C. S. Kim *et al.*, “Ballistocardiogram: Mechanism and Potential for Unobtrusive Cardiovascular Health Monitoring,” *Scientific Reports*, 2016.
- [10] I. Sadek, *Ballistocardiogram signal processing: A literature review*, 2018.
- [11] I. Starr, A. J. Rawson, H. A. Schroeder, and N. R. Joseph, “STUDIES ON THE ESTIMATION OF CARDIAC OUTPUT IN MAN, AND OF ABNORMALITIES IN CARDIAC FUNCTION, FROM THE HEART’S RECOIL AND THE BLOOD’S IMPACTS; THE BALLISTOCARDIOGRAM,” *American Journal of Physiology-Legacy Content*, 1939.

- [12] O. T. Inan, Dookun Park, L. Giovangrandi, and G. T. A. Kovacs, “Noninvasive Measurement of Physiological Signals on a Modified Home Bathroom Scale,” *IEEE Transactions on Biomedical Engineering*, vol. 59, no. 8, pp. 2137–2143, Aug. 2012.
- [13] Hyun Jae Baek, Gih Sung Chung, Ko Keun Kim, and Kwang Suk Park, “A Smart Health Monitoring Chair for Nonintrusive Measurement of Biological Signals,” *IEEE Transactions on Information Technology in Biomedicine*, vol. 16, no. 1, pp. 150–158, Jan. 2012.
- [14] D. Heise and M. Skubic, “Monitoring pulse and respiration with a non-invasive hydraulic bed sensor,” in *2010 Annual International Conference of the IEEE Engineering in Medicine and Biology Society, EMBC’10*, 2010.
- [15] C. Jiao, B.-Y. Su, P. Lyons, A. Zare, K. C. Ho, and M. Skubic, “Multiple Instance Dictionary Learning for Beat-to-Beat Heart Rate Monitoring From Ballistocardiograms,” *IEEE Transactions on Biomedical Engineering*, vol. 65, no. 11, pp. 2634–2648, Nov. 2018.
- [16] A. Alivar *et al.*, “Motion Artifact Detection and Reduction in Bed-Based Ballistocardiogram,” *IEEE Access*, vol. 7, pp. 13 693–13 703, 2019.
- [17] T. Reinvuo, M. Hannula, H. Sorvoja, E. Alasaarela, and R. Myllyla, “Measurement of respiratory rate with high-resolution accelerometer and emfit pressure sensor,” in *Proceedings of the 2006 IEEE Sensors Applications Symposium, 2006.*, IEEE, 2006, pp. 192–195, ISBN: 0-7803-9580-8.
- [18] E. Zimlichman *et al.*, “Early recognition of acutely deteriorating patients in non-intensive care units: Assessment of an innovative monitoring technology,” *Journal of Hospital Medicine*, vol. 7, no. 8, pp. 628–633, Oct. 2012.
- [19] J. Tuominen, K. Peltola, T. Saaresranta, and K. Valli, “Sleep parameter assessment accuracy of a consumer home sleep monitoring ballistocardiograph beddit sleep tracker: A validation study,” *Journal of Clinical Sleep Medicine*, vol. 15, no. 3, 2019.
- [20] R. Mukkamala, J.-O. Hahn, and A. Chandrasekhar, “Photoplethysmography in non-invasive blood pressure monitoring,” in *Photoplethysmography*, 2022.
- [21] T. Tamura, Y. Maeda, M. Sekine, and M. Yoshida, *Wearable photoplethysmographic sensors—past and present*, 2014.
- [22] R. Mukkamala *et al.*, “Toward Ubiquitous Blood Pressure Monitoring via Pulse Transit Time: Theory and Practice,” *IEEE Transactions on Biomedical Engineering*, 2015.

- [23] L. A. Geddes, M. H. Voelz, C. F. Babbs, J. D. Bourland, and W. A. Tacker, "Pulse Transit Time as an Indicator of Arterial Blood Pressure," *Psychophysiology*, 1981.
- [24] E. J. Wang *et al.*, "Seismo: Blood pressure monitoring using built-in smartphone accelerometer and camera," in *Conference on Human Factors in Computing Systems - Proceedings*, 2018, ISBN: 9781450356206.
- [25] A. M. Carek and O. T. Inan, "Robust Sensing of Distal Pulse Waveforms on a Modified Weighing Scale for Ubiquitous Pulse Transit Time Measurement," *IEEE Transactions on Biomedical Circuits and Systems*, vol. 11, no. 4, pp. 765–772, Aug. 2017.
- [26] A. M. Carek, H. Jung, and O. T. Inan, "A Reflective Photoplethysmogram Array and Channel Selection Algorithm for Weighing Scale Based Blood Pressure Measurement," *IEEE Sensors Journal*, 2020.
- [27] H. J. Baek, G. S. Chung, K. K. Kim, and K. S. Park, "A smart health monitoring chair for nonintrusive measurement of biological signals," *IEEE Transactions on Information Technology in Biomedicine*, 2012.
- [28] S. Gilaberte, J. Gómez-Clapers, R. Casanella, and R. Pallas-Areny, "Heart and respiratory rate detection on a bathroom scale based on the ballistocardiogram and the continuous wavelet transform," in *2010 Annual International Conference of the IEEE Engineering in Medicine and Biology Society, EMBC'10*, 2010, ISBN: 9781424441235.
- [29] M. Helfand, V. Christensen, and J. Anderson, *Technology Assessment: Early Sense for Monitoring Vital Signs in Hospitalized Patients*. 2011.
- [30] M. Tenhunen *et al.*, "Heart rate variability evaluation of Emfit sleep mattress breathing categories in NREM sleep," *Clinical Neurophysiology*, 2015.
- [31] J. K. Kimotho, T. Hemsell, and W. Sextro, "Estimation of Remaining Useful Lifetime of Piezoelectric Transducers Based on Self-Sensing," *IEEE Transactions on Reliability*, 2017.
- [32] C. Brüser, J. M. Kortelainen, S. Winter, M. Tenhunen, J. Pärkkä, and S. Leonhardt, "Improvement of force-sensor-based heart rate estimation using multichannel data fusion," *IEEE Journal of Biomedical and Health Informatics*, vol. 19, no. 1, 2015.
- [33] A. Q. Javaid, A. D. Wiens, N. F. Fesmire, M. A. Weitnauer, and O. T. Inan, "Quantifying and Reducing Posture-Dependent Distortion in Ballistocardiogram Measurements," *IEEE Journal of Biomedical and Health Informatics*, vol. 19, no. 5, pp. 1549–1556, Sep. 2015.

- [34] B. H. Choi, G. S. Chung, J.-S. Lee, D.-U. Jeong, and K. S. Park, "Slow-wave sleep estimation on a load-cell-installed bed: a non-constrained method," *Physiological Measurement*, vol. 30, no. 11, pp. 1163–1170, Nov. 2009.
- [35] L. Rosales, M. Skubic, D. Heise, M. J. Devaney, and M. Schaumburg, "Heartbeat detection from a hydraulic bed sensor using a clustering approach," in *2012 Annual International Conference of the IEEE Engineering in Medicine and Biology Society*, IEEE, Aug. 2012, pp. 2383–2387, ISBN: 978-1-4577-1787-1.
- [36] D. Hai *et al.*, "Heartbeat Detection and Rate Estimation from Ballistocardiograms using the Gated Recurrent Unit Network," in *2020 42nd Annual International Conference of the IEEE Engineering in Medicine & Biology Society (EMBC)*, IEEE, Jul. 2020, pp. 451–454, ISBN: 978-1-7281-1990-8.
- [37] National Asthma Education, "Expert Panel Report 3 (EPR-3): Guidelines for the Diagnosis and Management of Asthma-Summary Report 2007.," *The Journal of allergy and clinical immunology*, 2007.
- [38] G. Strategy, F. O. R. The, P. Of, C. Obstructive, and P. Disease, "From the Global Strategy for the Diagnosis, Management and Prevention of COPD, Global Initiative for Chronic Obstructive Lung Disease (GOLD) 2016.," Tech. Rep., 2016.
- [39] L. B. Gerald and W. C. Bailey, *Global initiative for chronic obstructive lung disease*, 2002.
- [40] D. L. Blackwell, J. W. Lucas, and T. C. Clarke, "Summary health statistics for U.S. adults: national health interview survey, 2012.," *Vital and health statistics. Series 10, Data from the National Health Survey*, 2014.
- [41] Natoinal Institutes of Health and National Institutes of Health, "Morbidity & Mortality: 2012 Chart Book on Cardiovascular, Lung, and Blood Diseases," *National Insitutes of Health*, 2012.
- [42] M. C. Townsend, "Spirometry in the occupational health setting-2011 update," *Journal of Occupational and Environmental Medicine*, 2011.
- [43] M. J. McGeachie *et al.*, "Patterns of Growth and Decline in Lung Function in Persistent Childhood Asthma," *New England Journal of Medicine*, 2016.
- [44] K. A. Johansson, E. Vittinghoff, J. Morisset, J. S. Lee, J. R. Balmes, and H. R. Collard, "Home monitoring improves endpoint efficiency in idiopathic pulmonary fibrosis," *European Respiratory Journal*, 2017.
- [45] H. A. Boushey *et al.*, "Daily versus As-Needed Corticosteroids for Mild Persistent Asthma," *New England Journal of Medicine*, 2005.

- [46] B. L. Graham *et al.*, *Standardization of spirometry 2019 update an official American Thoracic Society and European Respiratory Society technical statement*, 2019.
- [47] I. Gregg and A. J. Nunn, "Peak Expiratory Flow in Normal Subjects," *British Medical Journal*, 1973.
- [48] P. Lange *et al.*, "Lung-Function Trajectories Leading to Chronic Obstructive Pulmonary Disease," *New England Journal of Medicine*, 2015.
- [49] S. P. Bhatt *et al.*, "Discriminative Accuracy of FEV1:FVC Thresholds for COPD-Related Hospitalization and Mortality," *JAMA - Journal of the American Medical Association*, 2019.
- [50] J. Wanger *et al.*, "Standardisation of the measurement of lung volumes," *European Respiratory Journal*, vol. 26, no. 3, 2005.
- [51] B. A. Reyes, N. Reljin, Y. Kong, Y. Nam, and K. H. Chon, "Tidal Volume and Instantaneous Respiration Rate Estimation using a Volumetric Surrogate Signal Acquired via a Smartphone Camera," *IEEE Journal of Biomedical and Health Informatics*, vol. 21, no. 3, 2017.
- [52] G. Brüllmann, K. Fritsch, R. Thurnheer, and K. E. Bloch, "Respiratory monitoring by inductive plethysmography in unrestrained subjects using position sensor-adjusted calibration," *Respiration*, vol. 79, no. 2, 2009.
- [53] R. Farré, J. M. Montserrat, and D. Navajas, "Noninvasive monitoring of respiratory mechanics during sleep," *European Respiratory Journal*, 2004.
- [54] C. Li, V. M. Lubecke, O. Boric-Lubecke, and J. Lin, *A review on recent advances in doppler radar sensors for noncontact healthcare monitoring*, 2013.
- [55] K. Naishadham, J. E. Piou, L. Ren, and A. E. Fathy, "Estimation of Cardiopulmonary Parameters from Ultra Wideband Radar Measurements Using the State Space Method," *IEEE Transactions on Biomedical Circuits and Systems*, 2016.
- [56] A. D. Droitcour, O. Boric-Lubecke, and G. T. Kovacs, "Signal-to-noise ratio in doppler radar system for heart and respiratory rate measurements," *IEEE Transactions on Microwave Theory and Techniques*, 2009.
- [57] D. Zito *et al.*, "SoC CMOS UWB pulse radar sensor for contactless respiratory rate monitoring," *IEEE Transactions on Biomedical Circuits and Systems*, 2011.
- [58] P. Nguyen, X. Zhang, A. Halbower, and T. Vu, "Continuous and fine-grained breathing volume monitoring from afar using wireless signals," in *Proceedings - IEEE INFOCOM*, 2016, ISBN: 9781467399531.

- [59] P. Sharma, X. Hui, J. Zhou, T. B. Conroy, and E. C. Kan, “Wearable radio-frequency sensing of respiratory rate, respiratory volume, and heart rate,” *npj Digital Medicine*, vol. 3, no. 1, 2020.
- [60] X. Hui and E. C. Kan, “Monitoring vital signs over multiplexed radio by near-field coherent sensing,” *Nature Electronics*, 2018.
- [61] O. Polo, M. Tafti, M. Hamalainen, K. Vaahtoranta, and J. Alihanka, “Respiratory variation of the ballistocardiogram during increased respiratory load and voluntary central apnoea,” *European Respiratory Journal*, vol. 5, no. 2, 1992.
- [62] W. K. Lee, H. Yoon, C. Han, K. M. Joo, and K. S. Park, “Physiological signal monitoring bed for infants based on load-cell sensors,” *Sensors (Switzerland)*, vol. 16, no. 3, 2016.
- [63] A. Albukhari, F. Lima, and U. Mescheder, “Bed-embedded heart and respiration rates detection by longitudinal ballistocardiography and pattern recognition,” *Sensors (Switzerland)*, vol. 19, no. 6, 2019.
- [64] J. Alihanka, K. Vaahtoranta, and I. Saarikivi, “A new method for long-term monitoring of the ballistocardiogram, heart rate, and respiration,” *American Journal of Physiology - Regulatory Integrative and Comparative Physiology*, vol. 9, no. 3, 1981.
- [65] T. A., S. Z., S. D., C. S., and G. A., *Validation of contact-free sleep monitoring device with comparison to polysomnography*, 2017.
- [66] H. Jung, J. Kimball, T. Receveur, E. Agdeppa, and O. Inan, “Accurate Ballistocardiogram Based Heart Rate Estimation Using an Array of Load Cells in a Hospital Bed,” *IEEE Journal of Biomedical and Health Informatics*, 2021.
- [67] S. Isono *et al.*, “Contact-free unconstrained respiratory measurements with load cells under the bed in awake healthy volunteers: breath-by-breath comparison with pneumotachography,” *Journal of Applied Physiology*, vol. 126, no. 5, pp. 1432–1441, May 2019.
- [68] R. S. Weller, K. L. Foard, and T. N. Harwood, “Evaluation of a wireless, portable, wearable multi-parameter vital signs monitor in hospitalized neurological and neurosurgical patients,” *Journal of Clinical Monitoring and Computing*, 2018.
- [69] H. Brown, J. Terrence, P. Vasquez, D. W. Bates, and E. Zimlichman, “Continuous monitoring in an inpatient medical-surgical unit: A controlled clinical trial,” *American Journal of Medicine*, 2014.

- [70] G. Ogedegbe and T. Pickering, *Principles and Techniques of Blood Pressure Measurement*, 2010.
- [71] C. Yang and N. Tavassolian, “Pulse transit time measurement using seismocardiogram, photoplethysmogram, and acoustic recordings: Evaluation and comparison,” *IEEE Journal of Biomedical and Health Informatics*, 2018.
- [72] C. S. Kim, A. M. Carek, O. T. Inan, R. Mukkamala, and J. O. Hahn, “Ballistocardiogram-Based Approach to Cuffless Blood Pressure Monitoring: Proof of Concept and Potential Challenges,” *IEEE Transactions on Biomedical Engineering*, 2018.
- [73] B. Y. Su *et al.*, “Monitoring the Relative Blood Pressure Using a Hydraulic Bed Sensor System,” *IEEE Transactions on Biomedical Engineering*, 2019.
- [74] S. Chen, Z. Ji, H. Wu, and Y. Xu, “A non-invasive continuous blood pressure estimation approach based on machine learning,” *Sensors (Switzerland)*, vol. 19, no. 11, 2019.
- [75] M. Kachuee, M. M. Kiani, H. Mohammadzade, and M. Shabany, “Cuffless Blood Pressure Estimation Algorithms for Continuous Health-Care Monitoring,” *IEEE Transactions on Biomedical Engineering*, vol. 64, no. 4, 2017.
- [76] S. Haddad, A. Boukhayma, and A. Caizzone, “Continuous PPG-Based Blood Pressure Monitoring Using Multi-Linear Regression,” *IEEE Journal of Biomedical and Health Informatics*, 2021.
- [77] F. Miao, Z. D. Liu, J. K. Liu, B. Wen, Q. Y. He, and Y. Li, “Multi-Sensor Fusion Approach for Cuff-Less Blood Pressure Measurement,” *IEEE Journal of Biomedical and Health Informatics*, vol. 24, no. 1, 2020.
- [78] D.-K. Kim, Y.-T. Kim, H. Kim, and D.-J. Kim, “DeepCNAP: A Deep Learning Approach for Continuous Noninvasive Arterial Blood Pressure Monitoring Using Photoplethysmography,” *IEEE Journal of Biomedical and Health Informatics*, p. 1, 2022.
- [79] S. Mahmud *et al.*, “A Shallow U-Net Architecture for Reliably Predicting Blood Pressure (BP) from Photoplethysmogram (PPG) and Electrocardiogram (ECG) Signals,” *Sensors*, vol. 22, no. 3, 2022.
- [80] B. L. Hill *et al.*, “Imputation of the continuous arterial line blood pressure waveform from non-invasive measurements using deep learning,” *Scientific Reports*, vol. 11, no. 1, 2021.
- [81] K. Rishi Vardhan, S. Vedanth, G. Poojah, K. Abhishek, M. Nitish Kumar, and V. Vijayaraghavan, “BP-Net: Efficient Deep Learning for Continuous Arterial Blood

- Pressure Estimation using Photoplethysmogram,” in *Proceedings - 20th IEEE International Conference on Machine Learning and Applications, ICMLA 2021*, 2021.
- [82] W. Jia, Y. Li, Y. Bai, Z.-H. Mao, M. Sun, and Q. Zhao, “Estimation of heart rate from a chest-worn inertial measurement unit,” in *2015 International Symposium on Bioelectronics and Bioinformatics (ISBB)*, IEEE, Oct. 2015, pp. 148–151, ISBN: 978-1-4673-6609-0.
 - [83] G. Ligorio, E. Bergamini, I. Pasciuto, G. Vannozzi, A. Cappozzo, and A. Sabatini, “Assessing the Performance of Sensor Fusion Methods: Application to Magnetic-Inertial-Based Human Body Tracking,” *Sensors*, vol. 16, no. 2, p. 153, Jan. 2016.
 - [84] Z. Chen, J. T. Teo, S. H. Ng, and X. Yang, “Portable fiber optic ballistocardiogram sensor for home use,” in *Optical Fibers and Sensors for Medical Diagnostics and Treatment Applications XII*, Feb. 2012, p. 82180X.
 - [85] Yongwei Zhu, Haihong Zhang, M. Jayachandran, A. K. Ng, J. Biswas, and Zhihao Chen, “Ballistocardiography with fiber optic sensor in headrest position: A feasibility study and a new processing algorithm,” in *2013 35th Annual International Conference of the IEEE Engineering in Medicine and Biology Society (EMBC)*, IEEE, Jul. 2013, pp. 5203–5206, ISBN: 978-1-4577-0216-7.
 - [86] C. Bruser, A. Kerekes, S. Winter, and S. Leonhardt, “Multi-channel optical sensor-array for measuring ballistocardiograms and respiratory activity in bed,” in *2012 Annual International Conference of the IEEE Engineering in Medicine and Biology Society*, IEEE, Aug. 2012, pp. 5042–5045, ISBN: 978-1-4577-1787-1.
 - [87] O. T. Inan, M. Etemadi, R. M. Wiard, L. Giovangrandi, and G. T. Kovacs, “Robust ballistocardiogram acquisition for home monitoring,” *Physiological Measurement*, vol. 30, no. 2, 2009.
 - [88] L. Sörnmo and P. Laguna, *Bioelectrical Signal Processing in Cardiac and Neurological Applications*. Academic Press, 2005.
 - [89] C. H. Antink, H. Gao, C. Brüser, and S. Leonhardt, “Beat-to-beat heart rate estimation fusing multimodal video and sensor data,” *Biomedical Optics Express*, vol. 6, no. 8, p. 2895, Aug. 2015.
 - [90] C. H. Antink *et al.*, “On the Performance of Bed-Integrated Ballistocardiography in Long-Term Heart Rate Monitoring of Vascular Patients,” in *Computing in Cardiology*, 2019, ISBN: 9781728169361.
 - [91] C. Hoog Antink *et al.*, “Ballistocardiography Can Estimate Beat-to-Beat Heart Rate Accurately at Night in Patients After Vascular Intervention,” *IEEE Journal of Biomedical and Health Informatics*, vol. 24, no. 8, pp. 2230–2237, Aug. 2020.

- [92] G. G. BERNTSON *et al.*, “Heart rate variability: Origins, methods, and interpretive caveats,” *Psychophysiology*, vol. 34, no. 6, pp. 623–648, Nov. 1997.
- [93] K. Umetani, D. H. Singer, R. McCraty, and M. Atkinson, “Twenty-Four Hour Time Domain Heart Rate Variability and Heart Rate: Relations to Age and Gender Over Nine Decades,” *Journal of the American College of Cardiology*, vol. 31, no. 3, pp. 593–601, Mar. 1998.
- [94] Z. Zhang, “Photoplethysmography-Based Heart Rate Monitoring in Physical Activities via Joint Sparse Spectrum Reconstruction,” *IEEE Transactions on Biomedical Engineering*, vol. 62, no. 8, pp. 1902–1910, Aug. 2015.
- [95] J. Paalasmaa, H. Toivonen, and M. Partinen, “Adaptive Heartbeat Modeling for Beat-to-Beat Heart Rate Measurement in Ballistocardiograms,” *IEEE Journal of Biomedical and Health Informatics*, vol. 19, no. 6, pp. 1945–1952, Nov. 2015.
- [96] C. Carlson, V. R. Turpin, A. Suliman, C. Ade, S. Warren, and D. E. Thompson, “Bed-based ballistocardiography: Dataset and ability to track cardiovascular parameters,” *Sensors (Switzerland)*, vol. 21, no. 1, 2021.
- [97] O. Ronneberger, P. Fischer, and T. Brox, “U-net: Convolutional networks for biomedical image segmentation,” in *Lecture Notes in Computer Science (including sub-series Lecture Notes in Artificial Intelligence and Lecture Notes in Bioinformatics)*, vol. 9351, 2015.
- [98] P. F. Felzenszwalb and D. P. Huttenlocher, “Distance transforms of sampled functions,” *Cornell Computing and Information Science Technical Report TR20041963*, vol. 4, 2004.
- [99] D. Gavrilu, “Multi-feature hierarchical template matching using distance transforms,” 2002.
- [100] S. Hersek, B. Semiz, M. M. H. Shandhi, L. Orlandic, and O. T. Inan, “A Globalized Model for Mapping Wearable Seismocardiogram Signals to Whole-Body Ballistocardiogram Signals Based on Deep Learning,” *IEEE Journal of Biomedical and Health Informatics*, vol. 24, no. 5, 2020.
- [101] G. De Haan and V. Jeanne, “Robust pulse rate from chrominance-based rPPG,” *IEEE Transactions on Biomedical Engineering*, vol. 60, no. 10, 2013.
- [102] H. Jung, J. Kimball, T. Receveur, E. Agdeppa, and O. T. Inan, “Quantification of Posture-Induced Changes in Bed-Based Ballistocardiogram,” in *Computing in Cardiology*, vol. 2020-September, 2020.

- [103] A. L. Rosenberg, T. P. Hofer, R. A. Hayward, C. Strachan, and C. M. Watts, “Who bounces back? Physiologic and other predictors of intensive care unit readmission,” *Critical Care Medicine*, vol. 29, no. 3, 2001.
- [104] A. L. Rosenberg and C. Watts, “critical care reviews Patients Readmitted to ICUs * A Systematic Review of Risk Factors and,” *Chest*, vol. 118, 2000.
- [105] T. Jonsson, H. Jonsdottir, A. D. Möller, and L. Baldursdottir, “Nursing documentation prior to emergency admissions to the intensive care unit.,” *Nursing in critical care*, vol. 16, no. 4, 2011.
- [106] D. R. Goldhill, S. A. White, and A. Sumner, “Physiological values and procedures in the 24 h before ICU admission from the ward,” *Anaesthesia*, vol. 54, no. 6, 1999.
- [107] M. Folke, L. Cernerud, M. Ekström, and B. Hök, *Critical review of non-invasive respiratory monitoring in medical care*, 2003.
- [108] M. A. Cretikos, R. Bellomo, K. Hillman, J. Chen, S. Finfer, and A. Flabouris, “Respiratory rate: The neglected vital sign,” *Medical Journal of Australia*, vol. 188, no. 11, 2008.
- [109] K. Van Loon, B. Van Zaane, E. J. Bosch, C. J. Kalkman, and L. M. Peelen, *Non-invasive continuous respiratory monitoring on general hospital wards: A systematic review*, 2015.
- [110] P. G. Shekelle, “Nurse–Patient Ratios as a Patient Safety Strategy,” *Annals of Internal Medicine*, vol. 158, no. 5_Part_2, 2013.
- [111] J. B. West, *Pulmonary Physiology: The essentials*. Lippincott Williams & Wilkins, 2012.
- [112] S. McGee, “Respiratory Rate and Abnormal Breathing Patterns,” in *Evidence-Based Physical Diagnosis*, Elsevier, 2018, ch. Chapter 19.
- [113] M. Chu *et al.*, “Respiration rate and volume measurements using wearable strain sensors,” *npj Digital Medicine*, vol. 2, no. 1, 2019.
- [114] V. P. Seppä, J. Viik, and J. Hyttinen, “Assessment of pulmonary flow using impedance pneumography,” *IEEE Transactions on Biomedical Engineering*, vol. 57, no. 9, 2010.
- [115] H. Jung, S. Mabrouk, and O. T. Inan, “Impedance Pneumography: Assessment of Dual-Frequency Calibration Approaches,” in *2021 IEEE 17th International Conference on Wearable and Implantable Body Sensor Networks, BSN 2021*, 2021.

- [116] A. R. Fekr, K. Radecka, and Z. Zilic, "Design and Evaluation of an Intelligent Remote Tidal Volume Variability Monitoring System in E-Health Applications," *IEEE Journal of Biomedical and Health Informatics*, vol. 19, no. 5, 2015.
- [117] Y. S. Lee, P. N. Pathirana, C. L. Steinfort, and T. Caelli, "Monitoring and Analysis of Respiratory Patterns Using Microwave Doppler Radar," *IEEE Journal of Translational Engineering in Health and Medicine*, vol. 2, 2014.
- [118] S. Lyra *et al.*, "A deep learning-based camera approach for vital sign monitoring using thermography images for ICU patients," *Sensors*, vol. 21, no. 4, 2021.
- [119] W. M. St.-John and J. F. Paton, "Defining eupnea," *Respiratory Physiology and Neurobiology*, vol. 139, no. 1, 2003.
- [120] C. R. Fehnel *et al.*, "Incidence and Risk Model Development for Severe Tachypnea Following Terminal Extubation," *Chest*, vol. 158, no. 4, 2020.
- [121] A. Sadlon and L. chaitow, "Hyperventilation Syndrome/Breathing Pattern Disorders," in *Textbook of Natural Medicine*, 5th, Churchill Livingstone, 2020, ch. 135.
- [122] A. H. Gazi *et al.*, "Robust Estimation of Respiratory Variability Uncovers Correlates of Limbic Brain Activity and Transcutaneous Cervical Vagus Nerve Stimulation in the Context of Traumatic Stress," *IEEE Transactions on Biomedical Engineering*, 2021.
- [123] P. D. Welch, "The Use of Fast Fourier Transform for the Estimation of Power Spectra: A Method Based on Time Averaging Over Short, Modified Periodograms," *IEEE Transactions on Audio and Electroacoustics*, vol. 15, no. 2, 1967.
- [124] D. A. Birrenkott, M. A. Pimentel, P. J. Watkinson, and D. A. Clifton, "A robust fusion model for estimating respiratory rate from photoplethysmography and electrocardiography," *IEEE Transactions on Biomedical Engineering*, vol. 65, no. 9, 2018.
- [125] P. H. Charlton, T. Bonnici, L. Tarassenko, D. A. Clifton, R. Beale, and P. J. Watkinson, "An assessment of algorithms to estimate respiratory rate from the electrocardiogram and photoplethysmogram," *Physiological Measurement*, vol. 37, no. 4, 2016.
- [126] T. Chen and C. Guestrin, "XGBoost: A scalable tree boosting system," in *Proceedings of the ACM SIGKDD International Conference on Knowledge Discovery and Data Mining*, vol. 13-17-August-2016, 2016.
- [127] A. De Groote, M. Wantier, G. Cheron, M. Estenne, and M. Paiva, "Chest wall motion during tidal breathing," *Journal of Applied Physiology*, vol. 83, no. 5, 1997.

- [128] H. Kaneko and J. Horie, “Breathing movements of the chest and abdominal wall in healthy subjects,” *Respiratory Care*, vol. 57, no. 9, 2012.
- [129] K. Tavakolian, A. Vaseghi, and B. Kaminska, “Improvement of ballistocardiogram processing by inclusion of respiration information,” *Physiological Measurement*, vol. 29, no. 7, 2008.
- [130] D. Blanco-Almazan, W. Groenendaal, F. Catthoor, and R. Jane, “Analysis of Time Delay between Bioimpedance and Respiratory Volume Signals under Inspiratory Loaded Breathing,” in *Proceedings of the Annual International Conference of the IEEE Engineering in Medicine and Biology Society, EMBS*, 2019.
- [131] M. Młyńczak, W. Niewiadomski, M. Zyliński, and G. Cybulski, “Assessment of calibration methods on impedance pneumography accuracy,” *Biomedizinische Technik*, vol. 2015, 2015.
- [132] W. Massagram, N. Hafner, V. Lubecke, and O. Boric-Lubecke, “Tidal volume measurement through non-contact doppler radar with DC reconstruction,” *IEEE Sensors Journal*, vol. 13, no. 9, 2013.
- [133] D. E. Hurtado, J. A. Chavez, R. Mansilla, R. Lopez, and A. Abusleme, “Respiratory volume monitoring: A machine-learning approach to the non-invasive prediction of tidal volume and minute ventilation,” *IEEE Access*, 2020.
- [134] H. Jung, J. Kimball, T. Receveur, A. H. Gazi, E. Agdeppa, and O. Inan, “Estimation of Tidal Volume Using Load Cells on a Hospital Bed,” *IEEE Journal of Biomedical and Health Informatics*, 2022.
- [135] R. Mukkamala *et al.*, “Toward Ubiquitous Blood Pressure Monitoring via Pulse Transit Time: Theory and Practice,” *IEEE Transactions on Biomedical Engineering*, 2015.
- [136] V. Ganti *et al.*, “Enabling wearable pulse transit time-based blood pressure estimation for medically underserved areas and health equity: Comprehensive evaluation study,” *JMIR mHealth and uHealth*, vol. 9, no. 8, 2021.
- [137] V. G. Ganti, A. M. Carek, B. N. Nevius, J. A. Heller, M. Etemadi, and O. T. Inan, “Wearable Cuff-Less Blood Pressure Estimation at Home via Pulse Transit Time,” *IEEE Journal of Biomedical and Health Informatics*, vol. 25, no. 6, 2021.
- [138] D. Lee *et al.*, *Beat-to-beat continuous blood pressure estimation using bidirectional long short-term memory network*, 2021.

- [139] D. U. Jeong and K. M. Lim, “Combined deep CNN–LSTM network-based multi-tasking learning architecture for noninvasive continuous blood pressure estimation using difference in ECG-PPG features,” *Scientific Reports*, vol. 11, no. 1, 2021.
- [140] R. Song, H. Chen, J. Cheng, C. Li, Y. Liu, and X. Chen, “PulseGAN: Learning to Generate Realistic Pulse Waveforms in Remote Photoplethysmography,” *IEEE Journal of Biomedical and Health Informatics*, vol. 25, no. 5, 2021.
- [141] S. Pascual, A. Bonafonte, and J. Serra, “SEGAN: Speech enhancement generative adversarial network,” in *Proceedings of the Annual Conference of the International Speech Communication Association, INTERSPEECH*, vol. 2017-August, 2017.
- [142] J. Y. Zhu, T. Park, P. Isola, and A. A. Efros, “Unpaired Image-to-Image Translation Using Cycle-Consistent Adversarial Networks,” in *Proceedings of the IEEE International Conference on Computer Vision*, vol. 2017-October, 2017.
- [143] E. Brophy, M. De Vos, G. Boylan, and T. Ward, “Estimation of continuous blood pressure from ppg via a federated learning approach,” *Sensors*, vol. 21, no. 18, 2021.
- [144] M. Asgari Mehrabadi, S. A. H. Aqajari, A. H. Afandizadeh Zargari, N. Dutt, and A. M. Rahmani, *Novel Blood Pressure Waveform Reconstruction from Photoplethysmography using Cycle Generative Adversarial Networks*, Jun. 2022.
- [145] A. M. Carek, J. Conant, A. Joshi, H. Kang, and O. T. Inan, “SeismoWatch: Wearable Cuffless Blood Pressure Monitoring Using Pulse Transit Time,” *Proceedings of the ACM on Interactive, Mobile, Wearable and Ubiquitous Technologies*, 2017.
- [146] C. S. Kim, A. M. Carek, R. Mukkamala, O. T. Inan, and J. O. Hahn, “Ballistocardiogram as proximal timing reference for pulse transit time measurement: Potential for cuffless blood pressure monitoring,” *IEEE Transactions on Biomedical Engineering*, vol. 62, no. 11, 2015.
- [147] S. L. Martin *et al.*, “Weighing Scale-Based Pulse Transit Time is a Superior Marker of Blood Pressure than Conventional Pulse Arrival Time,” *Scientific Reports*, vol. 6, 2016.
- [148] P. Suresh, N. Narayanan, C. V. Pranav, and V. Vijayaraghavan, “End-to-End Deep Learning for Reliable Cardiac Activity Monitoring using Seismocardiograms,” in *Proceedings - 19th IEEE International Conference on Machine Learning and Applications, ICMLA 2020*, 2020.
- [149] P. Sarkar and A. Etemad, “CardioGAN: Attentive Generative Adversarial Network with Dual Discriminators for Synthesis of ECG from PPG,” Tech. Rep., 2021.

- [150] M. Chan, V. Ganti, and O. Inan, "Respiratory Rate Estimation using U-Net-Based Cascaded Framework from Electrocardiogram and Seismocardiogram Signals," *IEEE Journal of Biomedical and Health Informatics*, 2022.
- [151] J. Pan and W. J. Tompkins, "A Real-Time QRS Detection Algorithm," *IEEE Transactions on Biomedical Engineering*, vol. BME-32, no. 3, 1985.
- [152] Q. Li and G. D. Clifford, "Dynamic time warping and machine learning for signal quality assessment of pulsatile signals," *Physiological Measurement*, vol. 33, no. 9, 2012.
- [153] A. M. Carek and O. T. Inan, "Robust Sensing of Distal Pulse Waveforms on a Modified Weighing Scale for Ubiquitous Pulse Transit Time Measurement," *IEEE Transactions on Biomedical Circuits and Systems*, 2017.
- [154] O. Schlesinger, N. Vigderhouse, D. Eytan, and Y. Moshe, "Blood Pressure Estimation from PPG Signals Using Convolutional Neural Networks and Siamese Network," in *ICASSP, IEEE International Conference on Acoustics, Speech and Signal Processing - Proceedings*, vol. 2020-May, 2020.
- [155] R. C. Block *et al.*, "Conventional pulse transit times as markers of blood pressure changes in humans," *Scientific Reports*, vol. 10, no. 1, 2020.
- [156] M. Yavarimanesh *et al.*, "Assessment of Calibration Models for Cuff-Less Blood Pressure Measurement After One Year of Aging," *IEEE Transactions on Biomedical Engineering*, 2021.
- [157] I. Eşer, L. Khorshid, Ü. Yapucu Güneş, and Y. Demir, "The effect of different body positions on blood pressure," *Journal of Clinical Nursing*, vol. 16, no. 1, 2007.
- [158] M. S. Van Der Steen, A. M. Pleijers, J. W. Lenders, and T. Thien, "Influence of different supine body positions on blood pressure: Consequences for night blood pressure/dipper status," *Journal of Hypertension*, vol. 18, no. 12, 2000.
- [159] N. Watanabe, J. Reece, and B. I. Polus, "Effects of body position on autonomic regulation of cardiovascular function in young, healthy adults," *Chiropractic and Osteopathy*, vol. 15, 2007.
- [160] G. Cicolini *et al.*, "Differences in blood pressure by body position (supine, fowler's, and sitting) in hypertensive subjects," *American Journal of Hypertension*, vol. 24, no. 10, 2011.
- [161] IEEE, *IEEE Standard for Wearable , Cuffless Blood Pressure Measuring Devices IEEE Engineering in Medicine and Biology Society*. 2014, vol. 2019.

- [162] M. Saeed *et al.*, “Multiparameter intelligent monitoring in intensive care II: A public-access intensive care unit database,” in *Critical Care Medicine*, vol. 39, 2011.
- [163] V. B. Aydemir *et al.*, “Classification of Decompensated Heart Failure from Clinical and Home Ballistocardiography,” *IEEE Transactions on Biomedical Engineering*, vol. 67, no. 5, 2020.